CHARGE TRANSFER REACTIONS IN POROUS MATERIALS

BY

Katie R. Mitchell-Koch

Submitted to the graduate degree program in Chemistry
and the Graduate Faculty of the University of Kansas
in partial fulfillment of the requirements for the degree of
Doctor of Philosophy.

Committee:

Ward H. Thompson, Chairperson

Mikhail V. Barybin

Brian B. Laird

Aaron M. Scurto

Jon A. Tunge

The Dissertation Committee for Katie R. Mitchell-Koch certifies
that this is the approved version of the following dissertation:

CHARGE TRANSFER REACTIONS IN POROUS MATERIALS

Committee:

Ward H. Thompson, Chairperson

Mikhail V. Barybin

Brian B. Laird

Aaron M. Scurto

Jon A. Tunge

Date Approved: July 25, 2008

Dedicated with deep love and affection to Molly Rachel, my constant companion in writing this dissertation, and my family- Jeremy Mitchell-Koch, Melanie and Lawrence Mitchell, and Morey and MaryAnn James- whose abiding love and support have encouraged me every step of the way.

## ACKNOWLEDGMENTS

I am grateful for the generous support of the Fannie and John Hertz Foundation and the National Science Foundation Graduate Research Fellowship Program. This work has also been supported by grants from the Department of Energy and the National Science Foundation.

The Chemistry Department community at KU is fantastic- I have loved being a part of it, and it has certainly made my graduate school experience more enjoyable. Thanks to all of the faculty and staff for fostering such a supportive atmosphere.

I have had the privilege to work with a wonderful group of postdoctoral researchers in the Thompson group: Xiaobing Feng, Tolga Gulmen, Being Ka, Christine Morales, and Kumar Vanka. They have been good company and invaluable resources. Tolga had valuable input when interpreting the results presented in Chapter 3... and the group rocking chair seems a bit forlorn without him! I have had a lot of laughs and lively chats while sharing an office with Christine, and I am always amazed by all of the little Unix tricks she has stored. It was quite a transition coming home to write- I sure missed my officemate and friend Christine! I have also enjoyed working with Drew Vartia and Cassie Norton, and I couldn't "pass the torch" off to two better individuals!

Professor Ward Thompson is an amazing advisor. Not only has he taught me a great deal about chemistry through research, but he has also mentored me in career preparation and teaching. I know that I will be a better professor because of the experience and insight he has shared with me. Many, many thanks, Ward; I have had a wonderful graduate career, and it has been because of your advising style and engaging research program.

Two other professors have enriched my time in graduate school. Professor Misha Barybin has been a great collaborator. I have enjoyed working with Misha, and our discussions to understand how experimental and theoretical results fit together always spark my interest. Professor Brian Laird taught several classes that I took. His rigorous instruction, helpful math tricks, and interesting anecdotes made for a stimulating classroom experience. I learned a great deal that helped me in my research while deepening my knowledge for teaching physical chemistry. I also benefited from discussions with Brian regarding the research described in Chapter 2.

Finally, it has been quite an asset to have a spouse who has been through it before me- Jeremy has been a coach, cheerleader, sometimes even a bit of a nag- and it has been a great help in getting through grad school! Jeremy, your unfailing support has been just what I needed- all of those days and nights “home alone” while I have been in Lawrence working were certainly not an ideal for either of us. I am so grateful for your dedication to my education and willingness to make our two-city situation work.

# TABLE OF CONTENTS

Page

**ACCEPTANCE PAGE** . . . . . ii

**LIST OF TABLES** . . . . . x

**LIST OF FIGURES** . . . . . xi

**ABSTRACT** . . . . . xiii

**1 Introduction** . . . . . 1

1.1 Porous Materials . . . . . 1
1.2 Computational Studies of Nanoconfined Solutions . . . . . 4
1.3 Overview . . . . . 5

**2 Time-Dependent Fluorescence: Determining Entropic Contributions to the Free Energy of a Dye Molecule in Nanoconfined Solvents** . . . . . 7

2.1 Time-Dependent Fluorescence and Solvation Dynamics . . . . . 7
2.2 TDF Studies in Hydrophobic Cavities . . . . . 9
2.3 Methods . . . . . 12
2.3.1 Nanocavity System . . . . . 12
2.4 Monte Carlo Simulations . . . . . 14
2.4.1 Calculation of Entropy, Free and Internal Energies . . . . . 14
2.4.2 Simulation Details . . . . . 16
2.5 Solvent Packing . . . . . 18
2.6 Linear Solvents: Acetonitrile and Methyl Iodide . . . . . 20
2.6.1 Ground-state Solute in Linear Solvents: Free and Internal Energies . . . . . 22
2.6.2 Excited-state Solute in Linear Solvents: Free and Internal Energies . . . . . 23
2.6.3 Linear Solvents: Entropy . . . . . 30
2.7 Nonlinear Solvent: Methanol . . . . . 32
2.7.1 Ground-state Solute in Methanol: Free and Internal Energies . . 34
2.7.2 Excited-state Solute in Methanol: Free and Internal Energies . . 35
2.7.3 Methanol: Entropy . . . . . 37
2.8 Discussion . . . . . 40

Page

2.8.1 Electrostatic Effects . . . 42
2.8.2 Solute Orientation . . . 42
2.9 Conclusions . . . 48

**3 Infrared Spectra of a Proton-Transfer Complex in Nanoconfined Methyl Chloride Solution** . . . 51

3.1 Spectroscopic Studies of Proton Transfer . . . 52
3.2 Proton Transfer in Nanocavities . . . 53
3.3 Methods . . . 54
3.3.1 System . . . 54
3.3.2 Simulation Details . . . 58
3.3.3 Diabatic States and Calculation of Infrared Spectra . . . 59
3.4 Results . . . 64
3.4.1 $PT$ Case . . . 64
3.4.2 $PT_P$ and $PT_R$ Cases . . . 69
3.4.3 $P$ and $R$ Cases – No Proton Transfer . . . 73
3.4.4 Comparison of the Cases . . . 76
3.5 Discussion . . . 77
3.5.1 Solvent Coordinate and Frequency Distributions . . . 79
3.5.2 Condon and Other Approximations . . . 81
3.5.3 Linewidths and Motional Narrowing . . . 90
3.5.4 Proton Transfer Rate Constants . . . 91
3.6 Conclusion . . . 95

**4 *Ab Initio* Studies of a Carbon Acid for Potential Use as a Friedel-Crafts Acylation Solid Acid Catalyst** . . . 97

4.1 Introduction . . . 97
4.2 Solid Acids in Green Chemistry . . . 98
4.3 Acylation of 2-methoxynaphthalene . . . 104
4.4 Regioselective Friedel-Crafts Acylation with **Acid1**: Experimental Results . . . 108
4.5 *Ab Initio* and Density Functional Theory Calculations: Methods . . . 109
4.6 Thermodynamic Control . . . 109
4.7 Kinetic Factors . . . 112
4.8 Chemical Modifications of **Acid1**: Effects on Acidity . . . 116
4.9 Conclusions . . . 117

Page

**5 Conclusions** . . . . . 119

5.1 Overview and Future Directions . . . . . 119

**LIST OF REFERENCES** . . . . . 124

# LIST OF TABLES


| Table | | Page |
|---|---|---|
| 2.1 | Solvent, Solute, and Cavity Parameters. | 15 |
| 2.2 | Solvent Densities and Number of Molecules per Cavity | 19 |
| 3.1 | Parameters for Proton Transfer Complex. | 55 |
| 3.2 | The Five Proton Transfer Cases. | 56 |
| 3.3 | Parameters for Solvent and Proton Transfer Complex. | 57 |
| 3.4 | Motional Narrowing Parameters for the $P$ and $R$ Cases. | 90 |
| 4.1 | Relative Energies of Acylated 2-methoxynaphthalene. | 110 |
| 4.2 | Free Energies of AMN Regioisomers. | 112 |
| 4.3 | Calculated Charges for 2-methoxynaphthalene. | 114 |
| 4.4 | Relative Energies of *Sigma* Complex Intermediates. | 115 |
| 4.5 | Gas Phase Acidities. | 118 |

# LIST OF FIGURES


Figure Page

2.1 Solvent density of $CH_3I$ and $CH_3CN$ in $R$=10 Å cavities . . . . . 19

2.2 Solvent density of $CH_3OH$. . . . . 21

2.3 Ground-state energies in linear solvents, $R$=10 Å. . . . . 24

2.4 Ground-state energies in linear solvents, $R$=15 Å. . . . . 25

2.5 Excited-state energies in linear solvents, $R$=10 Å. . . . . 27

2.6 Excited-state energies in linear solvents, $R$=15 Å. . . . . 29

2.7 Entropy in linear solvents, $R$=10 Å. . . . . 31

2.8 Entropy in linear solvents, $R$=15 Å. . . . . 33

2.9 Ground-state energies in $CH_3OH$. . . . . 36

2.10 Excited-state energies in $CH_3OH$. . . . . 38

2.11 Entropy in $CH_3OH$. . . . . 39

2.12 Energies and entropy in $CH_3I$ with no solvent atomic charges. . . . . 43

2.13 Free energy surface in $CH_3OH$, $R$=10 Å. . . . . 44

2.14 Rotational entropies in $CH_3OH$. . . . . 46

2.15 Rotational entropies in $CH_3CN$, $R$=15 Å. . . . . 47

3.1 Proton potential energy curves for the five cases. . . . . 57

3.2 Instantaneous proton potentials at two values of $\Delta$E. . . . . 60

3.3 Frequency ($\omega$) versus solvent coordinate ($\Delta$E) . . . . . 61

Figure Page

3.4 Frequency distribution and IR spectrum for the $PT$ case. . . . . 65

3.5 Analytical fit to $PT$ spectrum. . . . . 68

3.6 Frequency distribution and IR spectrum for the $PT_P$ case. . . . . 70

3.7 Frequency distribution and IR spectrum for the $PT_R$ case. . . . . 71

3.8 Frequency distribution and IR spectrum for the $P$ case. . . . . 74

3.9 Frequency distribution and IR spectrum for the $R$ case. . . . . 75

3.10 Comparison of the five cases: spectra and frequency distributions. . . . . 78

3.11 Frequency versus solvent coordinate. . . . . 80

3.12 Solvent coordinate probability distributions and free energies. . . . . 82

3.13 Condon approximation compared to calculated infrared spectra. . . . . 84

3.14 Approximations to the $PT$ and $P$ spectra. . . . . 85

3.15 Approximations to the $PT_R$, $PT_P$, and $R$ spectra. . . . . 87

3.16 Transition dipole time correlation functions. . . . . 88

3.17 Frequency and reaction composition time correlation functions. . . . . 93

4.1 Chemical structure of **Acid1** . . . . . 98

4.2 Chemical modifications of **Acid1** . . . . . 99

4.3 Chemical structures of 2-MN and selected derivatives . . . . . 105

4.4 2-methoxynaphthalene: carbon numbers . . . . . 111

4.5 Proposed mechanism for Friedel-Crafts acylation . . . . . 113

## ABSTRACT

Porous materials, such as sol-gels and zeolites, contain nanometer-scale spaces in which molecules are confined, leading to significant changes in their chemical dynamics. In this dissertation, the effects of confinement on chemical behavior are studied. By understanding how the properties of a material affect functionality, the rational design of porous materials for applications such as catalysis may be achieved. The study of entropy and free energy of a nanoconfined model dye molecule with Monte Carlo methods is discussed in Chapter 2. In Chapter 3, infrared spectra of a model proton-transfer complex calculated using mixed quantum-classical molecular dynamics are calculated. These studies indicate that charge transfer dynamics and equilibria are spatially-dependent in nanoconfined systems. This is reflected in the time-dependent fluorescence and infrared spectra, discussed in Chapters 2 and 3, respectively. Chapter 4 describes quantum chemical studies of a carbon acid being developed for use in Friedel-Crafts acylation as a solid acid catalyst.

# Chapter 1

# Introduction

Recent advances in synthesis and characterization have led to the development of functional materials for a number of applications, including catalysis, separations, sensing, and optical materials.[1–12] In this work, computational studies have been undertaken to understand the chemistry and properties of some classes of these materials. In particular, a primary focus of this work is how nanoconfinement affects chemical behavior. A number of materials, including reverse micelles, sol-gels, and zeolites, contain nanoscale confining environments in which unique behavior takes place. By understanding how a confining framework influences the chemistry that takes place within, design principles for the development of novel functional materials may be elucidated. Properties that have been studied in this work include energetic and entropic driving forces for time-dependent fluorescence spectra, infrared spectra of a model proton-transfer complex, and properties and possible catalytic mechanisms of a novel carbon acid for applications in solid acid catalysis.

## 1.1 Porous Materials

Porous materials, including sol-gels, zeolites, clays, and metal organic frameworks, have been developed for a variety of applications.[11] Sol-gels are porous silica glasses formed by the hydrolysis of organosilicates.[1,13,14] These materials have a number of applications, including as catalysts,[15] sensors,[16] scaffolds for bone and tissue growth, and in optics. For optics, they are valued for thermal and mechanical stability, excellent

optical transmission ranging from UV to IR wavelengths, and the absence of significant defects (such as impurities or bubbles). Optics can also be made by inclusion (impregnation) of optically active molecules in the pores. In this case, the optical properties can be tailored by changing the pore size, surface properties and volume.[13] These doped sol-gels have been shown to be good materials for solid state dye lasers and as sensors.[17]

Zeolites are naturally-occurring or synthetic microporous, microcrystalline minerals used in catalysis. Zeolites are used most prolifically in the petroleum industry, where they catalyze a majority of all refining processes.[18] They are also used as catalysts in the synthesis of small organic molecules. More detail on zeolites and their use in Friedel-Crafts acylation reactions is given in Chapter 4, which describes studies of a carbon acid catalyst for the acylation of 2-methoxynaphthalene.

Porous materials have also been developed for gas storage, sensing, release, and separation. A class of microporous materials, low density three-dimensional solids of metal cluster joints and organic linkers, called metal-organic frameworks (MOFs), has been developed for numerous applications. A notable application of MOFs is for gas storage: different MOFs have shown high affinities for methane[19] and hydrogen[20,21] storage, which may be of use in developing the hydrogen economy and alternative energy sources. The low density of MOFs makes them attractive for portable energy storage. Another MOF application with environmental emphasis is the storage of carbon dioxide,[22] which could potentially be used for carbon dioxide sequestration. In addition to gas storage, selective gas adsorption by porous materials has proven useful for gas separations. One such material, ETS-4, a crystalline titanosilicate that is commerically available for separations, can discriminate between $N_2$ and $CH_4$ gases.[23]

Porous organic hosts can be functionalized by copolymerization with organic compounds or metal complexes. Both have been demonstrated to have applications in solid acid catalysis[8,24] (discussed further in Chapter 4), while the latter have demonstrated applications for gas storage. Metal complexes immobilized in an organic host were

shown to selectively bind NO and photolytically release the gas molecule, with potential applications for the storage and targeted release of NO for medical applications.[8]

Another system in which molecules experience nanoscale confinement is in reverse micelles. Reverse micelles are spontaneously formed when surfactant molecules with a polar head group and non-polar tail (alkylammonium carboxylates, for example)[25] are placed in a non-polar solvent, with a small amount of water (or other polar solvent). The head group solvates the polar solvent while forming a capsule. The shape of the capsule is dependent on the nature of the ampiphile, and can be spherical or oblong.[26] Reverse micelles are of interest for a number of reasons. First, they are often used to model biological systems, as the walls of a reverse micelle are similar to biological membranes. Reactions in reverse micelles also may exhibit enhanced rates, similar to those seen in enzymes, although reaction rates are often slower in these confined systems.[26] Secondly, because of their uniform size, they are considered "nanobeakers" in which reactions can take place in polar media within a non-polar solvent system. The size of the "nanobeakers," and thus the size of the solvent pool within and its corresponding confinement-influenced properties can be tuned by varying the ratio of polar solvent to surfactant.

Studies on reverse micelles have investigated the enhancement or inhibition of rates of chemical reactions within them.[25–30] Electron transfer reaction kinetics have also been studied; reverse micelles act as electron acceptors, forming solvated electrons in aqueous reverse micelles.[31–33] Other kinetics studies have been interested in excited-state proton transfer reactions[34–44] and the partitioning of substrates between the non-polar solvents and the interior of reverse micelles.[45,46] Because of the similarities between reverse micelles and biological systems, these reactions are of interest in understanding biologically-relevant chemical processes.

The above is just a sampling of the diverse types of porous materials, each comprising a wide variety of properties and functions, that have been synthesized or may be developed in the future. What remains to be understood is how to best design materials

for specific purposes. With this in mind, the studies reported in this dissertation have focused on charge transfer reactions in porous media. Charge transfer reactions are critical in many catalytic processes; one of the most basic and ubiquitous processes in catalysis is acid-base chemistry: a charge (proton) transfer reaction. The influence of confinement on charge transfer is a key focus of this work.

## 1.2 Computational Studies of Nanoconfined Solutions

In this work, several charge transfer reactions that take place in confining frameworks are considered. Charge transfer reactions, such as electron or proton transfer, are dependent on solvation dynamics, which are dramatically altered by confinement on the nanometer length scale (see Sections 2.1-2.2 and references therein). The reaction coordinate for these processes involves a collective solvent reorganization that facilitates the movement of charge.[47–53] Specifically, at the transition state the electric field generated by the solvent enables charge transfer. It is not one specific arrangement of solvent molecules at a single transition state, but rather a collection of transition states in which the solvent arrangement facilitates reaction (hence the term collective solvent coordinate). Because the confining framework influences solvation dynamics, reactions within nanoconfined spaces are influenced by solvent-framework interactions in addition to the reaction complex-framework interactions. By understanding how confinement and the properties of the confining framework (such as shape, flexibility, size, and surface chemistry) affect reactivity and solvent dynamics, the rational design of materials for diverse applications may be achieved.

In Chapters 2 and 3, a simple confining framework, which was originally developed as a model of reverse micelles, is used.[54–56] Details of this model are given in Chapter 2; briefly, a spherical nanocavity with smooth, hydrophobic walls is used. This nanocavity model has been used by the Thompson group in numerous investigations[57–66] to study dynamics and properties of nanoconfined solvents and solutions. Studies of a model

dye molecule that undergoes a significant change in dipole moment upon photoexcitation are presented in Chapter 2. This is done in the context of understanding how and why confinement affects the time-dependent fluorescence signal of the dye. Charge transfer in the same spherical cavity is again discussed in Chapter 3, but with a model proton transfer complex. The infrared spectra of the proton transfer complex are studied, with a focus on how chemical equilibria and proton transfer dynamics are reflected in vibrational spectroscopies. Chapter 4 considers a carbon acid catalyst that can be chemically modified and incorporated into a number of porous materials. In Chapters 2 and 3, the influence of the confining framework on chemical behavior is considered, while in Chapter 4, the properties of the carbon acid and possible catalytic mechanisms are explored.

## 1.3 Overview

In Chapter 2, Monte Carlo simulations are used to calculate the free energy, internal energy, and entropy of a model dye molecule dissolved in three different nanoconfined solvents. From the contributions to the free energies of the dye molecule in these various systems, the driving forces for the time-dependent fluorescence signal can be understood. Simulations allow for a "bird's eye" view at the molecular level, enabling the position-dependent free energy and entropy to be calculated as a function of the radial distance from the cavity wall. Different components of the entropy are considered, and rotational contributions to the entropy are calculated explicitly. It is found that solvent packing influences rotational freedom of the solute, giving rise to a strong correlation between the radial solvent density and the entropy and free energy. The spatial dependence of such quantities provides information about how confinement influences dynamics. In Chapter 3, mixed quantum-classical molecular dynamics simulations are used to calculate the infrared spectra of a model proton-transfer complex in nanoconfined solution. The infrared spectra are shown to contain information about proton

transfer dynamics and equilibria, providing further information about chemical reactivity in nanoconfined solutions. While pump-probe experiments have been used to study excited-state proton transfer rates, the work in Chapter 3 indicates that ground-state proton transfer rates may be able to be determined from infrared photon-echo experiments. Chapter 4 takes a different approach to studying charge transfer reactions in porous media, with a focus on the charge transfer agent itself through *ab initio* and DFT studies of a carbon acid that can be incorporated into a variety of porous materials for use as a solid acid. This acid is interesting in itself, since the acidic proton is bound to a carbon. The unusual acid was calculated to have a gas-phase acidity that is stronger than many common strong acids, such as $HNO_3$ and HCl. The carbon acid has shown unprecedented regioselectivity in the Friedel-Crafts acylation of 2-methoxynaphthalene, which is a step in the synthesis of the analgesic (*S*)-naproxen. The calculations indicate that the regioselectivity arises from the ability of the acid to catalyze the formation of the thermodynamic product. Chemical modifications can be carried out in order to incorporate the carbon acid into a porous material, forming a solid acid with green chemistry applications.

# Chapter 2

# Time-Dependent Fluorescence: Determining Entropic Contributions to the Free Energy of a Dye Molecule in Nanoconfined Solvents

Spectroscopy provides a way to investigate how nanoscale confinement affects chemical dynamics and reactivity. In this chapter, the molecular driving forces that give rise to a time-dependent fluorescence signal are explored. Time-dependent fluorescence (TDF) is a spectroscopic method used to probe solvation dynamics. In the following chapter, infrared spectroscopy in a nanoconfined system is considered. In both cases, investigations of charge transfer processes are undertaken. In this chapter, the system studied is a model dye molecule, which undergoes a significant change in dipole moment upon excitation, confined in organic solvents in 10 and 15 Å radius spherical, hydrophobic cavities.

## 2.1 Time-Dependent Fluorescence and Solvation Dynamics

Solvation dynamics describes the time evolution of solvent-solute interactions, and is often measured as a solvent response to changes in the solute dipole moment. Typically, studies of solvation dynamics involve dyes that undergo a large change in dipole moment upon photoexcitation. Other important probes of solvation dynamics involve excited-state electron and proton transfer reactions.[37–44,62,63,67–80] Such charge transfer processes have been shown to depend on a reaction coordinate involving solvent reorganization that facilitates the movement of charge.[47–53] In nanoconfined systems, the confining framework can influence chemical reactions and dynamics both through solute-framework interactions and through solvent-framework interactions that modify

the solvation dynamics. Thus, studies of solvation dynamics in nanoconfined systems probe how different confining frameworks influence chemical behavior and reactivity within. In addition to time-dependent fluorescence studies,[56,58,81–107] described below, and spectroscopic studies of excited-state electron[68] and proton transfer,[37–44,70–76] other studies of solvation dynamics in nanoconfined systems include rotational mobility measurements with fluorescence depolarization spectroscopy,[67] and proton conductivity measurements.[78–80]

In time-dependent fluorescence spectroscopy, the Stokes shift as a function of time is measured. For a chromophore in solution, before photoexcitation, the molecule is solvated according to the ground-state distribution of charges. Instantaneously upon excitation, according to the Franck-Condon principle, the electronic configuration of the chromophore has changed to an excited-state charge distribution, while the solvent nuclear degrees-of-freedom are still configured to the ground-state electronic distribution of the solute. As the solvent molecules reorient to better solvate the chromophore, the energy gap between the excited state and ground state decreases, causing the Stokes shift to redshift. The normalized time-dependent Stokes shift signal, called the solvent response function $C(t)$, is given according to Equation 2.1:

$$C(t) = \frac{\omega(t) - \omega(\infty)}{\omega(0) - \omega(\infty)}, \qquad [2.1]$$

where $\omega(t)$ is the time-dependent fluorescence frequency at time $t$, $\omega(0)$ is the instantaneous fluorescence frequency after excitation, and $\omega(\infty)$ is the equilibrium emission frequency. The rate of decay of the time-dependent Stokes shift provides information about how quickly solvent reorientation takes place, which in turn provides information about the dynamics of the solvent coordinate, upon which many charge transfer processes rely (see above). For bulk solvent, the TDF Stokes shift signal decays exponentially on a subpicosecond to picosecond timescale. As an example, TDF studies on Coumarin 480 in bulk water show a solvent response that is nearly complete at 1 ps.[108] In contrast, for nanoconfined systems, TDF measurements generally find that the fluorescence energy decays on multiple time scales, including ones that are significantly

longer than those observed in bulk solvents. For instance, TDF measurements on aqueous Coumarin 480 trapped in a sol-gel matrix with pore diameters of 10-20 Å found the Stokes shift decays with multiple time scales, the longest taking on the order of 15 ns.[92] Clearly such substantial modification of the solvation dynamics upon nanoscale confinement affects how a chemical reaction occurs. In order to understand how to design nanostructured materials for desired applications, such as supports for catalysts or molecular sensors, we need to uncover the origins of these changes in the solvation properties. The work described in this chapter addresses one potential driving force for the properties of nanoconfined solvents: entropy.

## 2.2 Time-Dependent Fluorescence Studies in Hydrophobic Cavities

Previous work in the Thompson group has involved the calculation of absorption and fluorescence spectra of a model diatomic dye molecule in nanoconfined methyl iodide and acetonitrile solvents in a number of sizes of hydrophobic spherical cavities, having radii of 10, 12, 15, and 20 Å.[57] The nanocavity and model dye, which are the same system as used in the work described in this chapter, are described in detail below, in Section 2.3. The absorption and fluorescence spectra were calculated from solvent coordinate values acquired from Monte Carlo simulations of the dye molecule in the ground state and excited state, respectively. The solvent coordinate, $\Delta E$, is defined as

$$\Delta E = E_{ex} - E_{gr}, \qquad [2.2]$$

where $E_{ex}$ is the energy of the system with the dye in the excited state, and $E_{gr}$ is the ground-state energy. The differences in the two energies arise only from the charge interactions between the solvent and the dye molecule in the two states, plus the 2 eV energy offset between the ground and excited states of the dye molecule.

It was found that the absorption spectra are nearly identical for all cavity sizes, while the fluorescence spectra are blue-shifted with decreasing cavity size in both solvents. Also, it was found that the probability distribution of the ground-state dye molecule

is peaked near the cavity wall, while the probability distribution for the excited-state dye molecule is bimodal, with one peak near the cavity wall and a second, larger peak for the solute molecule located in the interior of the cavity. These results suggest that diffusive motion of the solute toward the interior upon photoexcitation may give rise to the long timescale of TDF signals in nanoconfined systems. To confirm this, molecular dynamics simulations were carried out.[58]

Nonequilibrium molecular dynamics simulations in nanoconfined $CH_3I$ solution in 10, 12, 15 and 20 Å spherical, hydrophobic cavities were used to calculate the TDF data for the model dye molecule. As described in Ref. 58, it was found that the solvent response function, $C(t)$ (Eq. 2.1), decayed triexponentially, fit by the following expression:

$$C(t) = A_1 e^{-t/\tau_1} + A_2 e^{-t/\tau_2} + A_3 e^{-t/\tau_3}. \quad [2.3]$$

The three time scales are approximately $\tau_1$ ∼300 fs, $\tau_2$ ∼2 ps, and $\tau_3$ ∼30-40 ps for all of the TDF signals, regardless of cavity size, with a solvent density of ∼90% the bulk value in methyl iodide. Fluorescence spectra were calculated at different fixed distances of the solute center-of-mass within the cavity, and it was found that the spectra redshift and broaden as the solute position moves away from the cavity wall. Corroborating this data is the solute diffusion toward the interior of the cavity upon photoexcitation. The solute diffusion takes place on two timescales, fitting the expression

$$\langle \Delta d(t) \rangle = D(1 - B_1 e^{-t/\tau_{d1}} - B_2 e^{-t/\tau_{d2}}). \quad [2.4]$$

There is an initial, rapid motion with $\tau_{d1}$ ∼1.4 ps, while $\tau_{d2}$ varies with cavity size, ranging from ∼350 ps for the 10 Å cavity, ∼120 ps for the 12 Å cavity, to ∼70 ps for the 15 Å cavity.

By combining the solute diffusion data, probability distributions for the ground and excited state of the dye molecule, and the TDF spectra, one can conclude that one of the contributions to the longest timescale observed in the TDF signal is diffusion of the excited dye molecule toward the interior of the cavity. Clearly, spatially-dependent free

energies/probability distributions do not arise in bulk (unconfined) solutions, suggesting that this phenomenon contributes to the unique TDF spectra acquired in nanoconfined systems. In addition to spherical cavities, absorption and fluorescence spectra for ellipsoidal cavities were investigated.[59] It was found that, as with the spherical cavities, the dye molecule in the ground state had high probability of being located near the cavity wall. Moreover, the distribution was peaked at the "ends" of the ellipsoids. For the excited-state solute, there was likewise a higher probability density for the solute near the interior of the cavity.

In general, the differences in the probability distributions of the ground- and excited-state dye molecule for the spherical and ellipsoidal cavities can be explained in terms of effective solvent polarity: near the cavity center, the solvent is effectively more polar, favoring solvation of the more polar excited-state solute; near the cavity wall, the solvent is effectively less polar, favoring the relatively non-polar ground-state dye molecule. While electrostatics clearly play an important role in the probability distributions of the dye molecule in its two electronic states, the contributions of internal energy and entropy to the free energies are considered explicitly in this work. Moreover, the influence of solvent packing effects on these contributions to the free energies is considered.

In this Chapter, a number of systems are considered in which a model dye molecule is confined. Three different solvents with various properties are investigated: $CH_3I$, $CH_3CN$, and $CH_3OH$. The size of the confining framework is also varied: both 10 and 15 Å radius spherical cavities are studied. The entropy, free energies, and internal energies of the model dye molecule are calculated using Monte Carlo simulations. The methods are described in Sections 2.3 and 2.4.2. The solvent packing of methyl iodide, acetonitrile, and methanol solvents, which was found to be related to the energies and entropy, is described in Section 2.5. The free and internal energies and entropy for the linear solvents and methanol in the two cavity sizes are given in Sections 2.6 and 2.7.

In Section 2.8, the origins of the maxima and minima in the entropy are considered, with conclusions summarized in Section 2.9.

## 2.3 Methods

### 2.3.1 Nanocavity System

The systems studied in this work, like the earlier work of the Thompson group, described above,[57–59] involve a model diatomic dye molecule (denoted as *AB*) solvated in an organic solvent enclosed in a smooth-walled hydrophobic, spherical cavity. The dye molecule model was adapted from one developed by Carter and Hynes.[109,110] The dye molecule interacts with other molecules through Lennard-Jones (see Eq. 3.3) and Coulombic interactions, which are detailed in Table 2.3.1. The solute molecule is described by a two valence-bond state model, with electronic coupling between the states equal to 0.01 eV, such that the ground and excited states are effectively of fixed charge character. The excited state lies 2 eV above the ground state *in vacuo*. In the ground state, the solute molecule is relatively nonpolar, with *A* having a charge +0.1 $|e|$ and *B* a charge of $-0.1$ $|e|$, giving $\mu$=1.44 D. In the excited state, the dipole moment is substantial: $\mu$=7.1 D, with *A/B* charges of +0.5/-0.5 $|e|$. The solute interacts through both Lennard-Jones and Coulombic interactions; the Lennard-Jones parameters are identical for both *A* and *B* and are independent of the electronic state.

The hydrophobic cavity model used in this work, based on reverse micelles, was designed by Linse and Halle,[54,55] with modified parameters by Faeder and Ladanyi.[56] Here, the smooth, hydrophobic walls interact exclusively via Lennard-Jones interactions; thus, the potential is only a function of the radial distance of an interaction site from the center of the cavity. The model potential between an interaction site and the cavity walls is calculated by assuming that the cavity is comprised of a continuum of sites at constant density. The resulting cavity model potential is of the 3-9 form with

curvature corrections that depend on the cavity radius. Thus, the potential is given as

$$U = 8\pi\rho_{hc}\,\epsilon\,\sigma^3\left[\left(\frac{\sigma}{R}\right)^9 F(z,6) - \left(\frac{\sigma}{R}\right)^3 F(z,3)\right], \qquad [2.5]$$

where $\rho_{hc}$ is the density of the hydrocarbon interaction sites on the cavity walls, $\epsilon$ and $\sigma$ are Lennard-Jones parameters, and $R$ is the radius of the cavity. The quantity $z$ is defined as a function of the cavity size and the distance $r$ of the interaction site from the center of the cavity:

$$z = \frac{r}{R}. \qquad [2.6]$$

The functions $F(z,n)$ are calculated by integrating over all points of the hydrocarbon exterior of the cavity:

$$F(z,n) = \int_0^\infty dy \int_{-1}^1 dx \left[\frac{y^2}{(z^2+y^2-2xyz)^n}\right] \qquad [2.7]$$

Thus,

$$F(z,3) = \frac{2}{3(1-z^2)^3} \qquad [2.8]$$

and

$$F(z,6) = \frac{2(5+45z^2+63z^4+15z^6)}{45(1-z^2)^9}. \qquad [2.9]$$

In the limit of $R \to \infty$, the 3-9 potential between a flat hydrocarbon surface and the interaction site is recovered. In this work, spherical cavities of two different sizes, radius $R$=10 and 15 Å , were studied. With the parameters used by Faeder and Ladanyi,[56,106,107] the expression in Eq. 2.5 simplifies to

$$U(z) = 18\sqrt{3}\,\epsilon_{wall}\left[\left(\frac{15}{2}\right)\left(\frac{\sigma_{wall}}{R}\right)^9 F(z,6) - \left(\frac{\sigma_{wall}}{R}\right)^3 F(z,3)\right]. \qquad [2.10]$$

The Lennard-Jones parameters used here are the same as in Refs. 56, 106 and 107: $\sigma_{wall}$= 2.5 Å and $\epsilon_{wall}$= 0.46 kcal/mol.

Three solvents were investigated in this work: methyl iodide, acetonitrile, and methanol. For all three cases, rigid molecule models of $CH_3I$,[111] $CH_3CN$,[112] and $CH_3OH$[113,114] were employed; all models feature a "unified atom" (single interaction

site) to describe the methyl groups. The two effectively linear solvents, $CH_3I$ ($\epsilon$=6.97) and $CH_3CN$ ($\epsilon$=36.64),[115] were chosen because of their similarity in size but differing polarities. Methanol, a nonlinear solvent with a dielectric constant ($\epsilon$=33.0) similar to acetonitrile,[115] is a slightly smaller molecule that exhibits hydrogen bonding interactions, and provides a contrast to the solvent packing motif displayed by $CH_3I$ and $CH_3CN$ (see below). The proton in methanol is treated as a point charge in the model used here. The parameters for interactions of the solute, solvents, and cavity wall are summarized in Table 2.3.1.

## 2.4 Monte Carlo Simulations

The aim of this work was to determine the entropy, $\Delta S$, as a function of the solute radial position in spherical nanocavities. To do so, the Helmholtz free energy, $\Delta A$, and internal energy, $\Delta U$, were calculated using Monte Carlo methods.

### 2.4.1 Calculation of Entropy, Free and Internal Energies

Helmholtz free energies were calculated by thermodynamic integration.[116,117] In this approach, the solute center-of-mass position (at distance $r$ from the cavity center) is held fixed and the average radial force, $\langle F(r) \rangle$, on the solute center-of-mass,

$$\langle F(r) \rangle = \left\langle -\frac{\partial U}{\partial r} \right\rangle = \frac{\int d\mathbf{q} \int d\mathbf{p} \left( \frac{-\partial U}{\partial r} \right) e^{-\beta H(\mathbf{p},\mathbf{q})}}{\int d\mathbf{q} \int d\mathbf{p}\, e^{-\beta H(\mathbf{p},\mathbf{q})}} . \qquad [2.11]$$

is calculated. Free energies are a measure of work, and thermodynamic integration here calculates the free energy as force times distance. In this work, the free energy, $A(r)$, is obtained by integrating the average radial force over the solute radial distance, *r*:

$$\Delta A(r) \equiv A(r) - A(r_0) = -\int_{r_0}^{r} dr\ \langle F(r) \rangle. \qquad [2.12]$$

The integration was carried out with a simple integration scheme: using the trapezoidal rule. Other integration methods were tested for comparison, and they yielded similar results.

Table 2.1 Interaction Parameters for Solute, Solvents, and Nanocavity.

| Site | $\epsilon$(kcal/mol) | $\sigma$(Å) | $q(\|e\|)$ | $r_{ij}$(Å) |
|---|---|---|---|---|
| **Solute** | | | | |
| *Ground State* | | | | |
| $A$ | 0.3976 | 3.5 | +0.1 | |
| $B$ | 0.3976 | 3.5 | -0.1 | 3.0 |
| *Excited State* | | | | |
| $A$ | 0.3976 | 3.5 | +0.5 | |
| $B$ | 0.3976 | 3.5 | -0.5 | 3.0 |
| **Solvents** | | | | |
| ***$CH_3I$***[111] | | | | |
| $CH_3$ | 0.2378 | 3.77 | +0.25 | |
| I | 0.5985 | 3.83 | -0.25 | 2.16 |
| ***$CH_3CN$***[112] | | | | |
| $CH_3$ | 0.207 | 3.775 | +0.15 | |
| C | 0.150 | 3.65 | +0.28 | 1.458 |
| N | 0.170 | 3.2 | -0.43 | 1.157 |
| ***$CH_3OH$***[113,114] | | | | |
| $CH_3$ | 0.2071 | 3.775 | +0.265 | |
| O | 0.1701 | 3.071 | -0.7 | 1.4246 |
| H | 0.0 | 0.0 | +0.435 | 0.9451 |
| $\angle$COH=108.5° | | | | |

In addition to the free energy obtained by thermodynamic integration, the internal energy was calculated as a function of radial distance. In each simulation for a fixed $r$, the average internal energy, $U(r)$, is obtained by straightforward averaging of the potential energy, $U(r) = \langle V_r \rangle$, and then

$$\Delta U(r) \equiv U(r) - U(r_0) = \langle V_r \rangle - \langle V_{r_0} \rangle. \quad [2.13]$$

The value of $r_0$ is arbitrary since we are only concerned about relative energies; in all cases, it was taken to be $r_0$= 0.25 Å, the smallest radial position considered. The solute center-of-mass position was fixed in increments of 0.25 Å; for each position, a full Monte Carlo simulation was carried out, in which radial forces and internal energy data were collected.

From the difference in internal and free energies, the entropy was calculated as

$$\Delta S(r) = \frac{\Delta U(r) - \Delta A(r)}{T}. \quad [2.14]$$

The temperature, $T$, for all simulations in this work is 298 K.

Errors were calculated by block averaging the forces and internal energies over 40 blocks; data is reported with a 95% confidence interval using the Student *t* distribution.[118] Errors in the free energies were relatively low (generally $\leq$0.2 kcal/mol), while errors in the internal energy were higher (ranging from $\leq$0.2 kcal/mol in $CH_3I$ to $\sim$0.7 kcal/mol in $CH_3OH$, despite an increased number of Monte Carlo cycles for the latter solvent). Thus, the largest contribution to the error in the entropy comes from the internal energy, resulting in uncertainties in the entropies of $\sim$0.5-1 cal/(mol·K) in $CH_3I$ up to $\sim$2-3 cal/(mol·K) in $CH_3OH$.

### 2.4.2 Simulation Details

All Monte Carlo simulations were carried out in the canonical (NVT) ensemble at a temperature of 298 K. Configurations within the cavity were initiated with a warmup

cycle in which the initial positions of the solute and solvent were placed on a face-centered cubic lattice. For each solute radial position required for thermodynamic integration, the cavity coordinates were chosen such that the solute center-of-mass was placed at the desired radial distance from the center of the cavity. The number of molecules, $N_{mol}$, in the simulation was determined from the specified density (here, 90% of the bulk liquid density at 298 K) and the cavity size. Note that the volume used in the density calculations accounts for the excluded volume of the cavity walls: the cavity radius was reduced by 0.5 $\sigma_{wall}$. Initially, a spherical cavity large enough to include all of the desired molecules was created. The molecules were then allowed to equilibrate, with the cavity radius shrinking by 0.1 Å every 100 cycles (1 cycle=$N_{mol}$ steps) until the specified cavity size was reached. Afterwards, the equilibration was continued to reach a total of $4 \times 10^5$ Monte Carlo cycles as a warmup, followed by a longer data collection period (see below). For solvent molecules, the center-of-mass position was translated and the molecule was rotated in each step. For a step involving the solute, only rotation was allowed, as the center-of-mass position was fixed in order to carry out thermodynamic integration (see above). Each move was accepted or rejected according to the Metropolis method.[119] With the Metropolis method, each random move is always accepted if it results in a lower energy. If the move results in a higher energy, the move is accepted if the Boltzmann factor of the change in energy, $\Delta E$, is greater than a randomly generated number , $N_{ran}$, between 0 and 1:

$$e^{-\frac{\Delta E}{k_B T}} > N_{ran}. \qquad [2.15]$$

Data was collected over a run of $4 \times 10^6$ Monte Carlo cycles for methyl iodide and acetonitrile solvents, and $6 \times 10^6$ Monte Carlo cycles for methanol. Table 2.2 lists the number of molecules for the systems studied.

## 2.5 Solvent Packing

The free energies and entropies were found to be related to solvent packing, so a brief discussion of this is useful for interpreting the results. Compared to bulk liquids, solvent organization if considerably more ordered upon confinement. Clearly, the solvent ordering may impact chemistry in nanoconfined systems and contribute to differences between chemistry in nanocavities versus bulk systems.

Two linear solvents, methyl iodide and acetonitrile, were studied. Although the two solvents have quite different polarities ($\epsilon_{CH_3I}$=6.97, $\epsilon_{CH_3CN}$=36.64),[115] they are similar in size and were found to pack in a similar fashion. The rod-shaped molecules lay parallel to the wall, forming layers. For the 10 Å cavity, there are two layers or spherical shells of solvent. For the 15 Å cavity, there are three layers, with one or two solvent molecules located in the center within the layered structure. The solvent density of $CH_3I$ and $CH_3CN$ in the $R$=10 Å cavities is shown in Figure 2.1; the density is plotted both as a function of atomic density and total solvent density, illustrating the orientation of the solvent parallel to the cavity wall. The packing of the layers is governed by the van der Waals radii of the atoms. As can be seen in Figure 2.1, in acetonitrile, the distance between the peak atomic solvent density in the first and second layers is $\sim$3.85 Å for the methyl groups ($\sigma_{CH_3}$= 3.775 Å), $\sim$3.65 Å for the carbon atoms ($\sigma_C$= 3.65 Å), and $\sim$3.4 Å for nitrogen ($\sigma_N$= 3.2 Å). Likewise, in methyl iodide the spacing is $\sim$3.9 Å for both the methyl groups ($\sigma_{CH_3}$= 3.775 Å) and the iodine atoms ($\sigma_I$= 3.83 Å). The atomic solvent densities combine to form the total solvent density, resulting in two peaks located at distances $d$ $\sim$3.4 Å and $d$ $\sim$7.25 Å from the cavity wall. The solvent density in the $R$=15 Å cavities is similar to the $R$=10 Å cavities in that the solvent layering of $CH_3I$ and $CH_3CN$ in the $R$=15 Å cavities is dominated by packing effects.

Methanol, a non-linear solvent that displays hydrogen bonding, has a somewhat different solvent packing motif than the linear solvents. While the linear solvents pack

2.2

Table 2.2 Densities of Bulk Solvents and Number of Solvent Molecules per Simulation.

| Solvent | Density (g/cm$^3$)[115] at 298 K | Molar density (mol/cm$^3$) | $R$=10 Å | $R$=15 Å |
|---|---|---|---|---|
| $CH_3I$ | 2.2789 | 0.01606 | 23 | 93 |
| $CH_3CN$ | 0.7825 | 0.01915 | 27 | 111 |
| $CH_3OH$ | 0.7925 | 0.02447 | 36 | 144 |

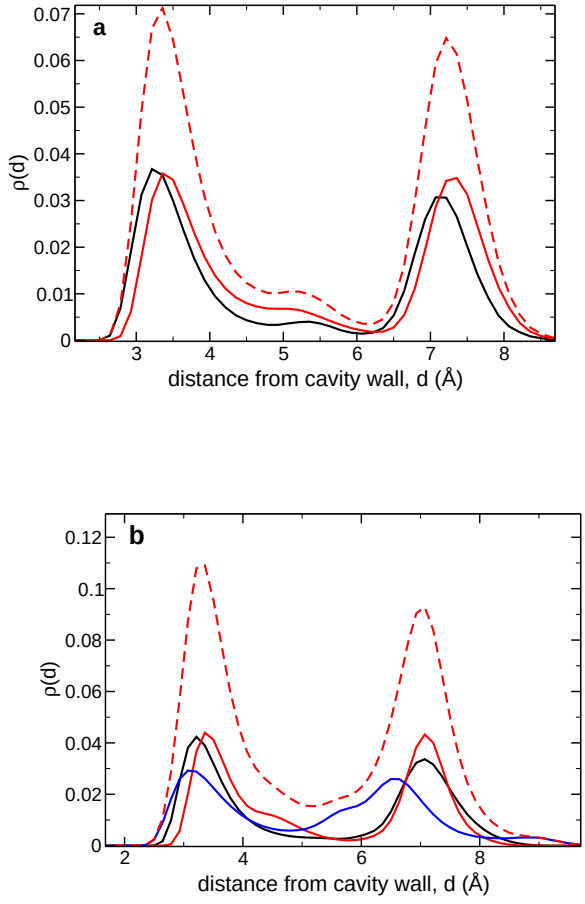


Figure 2.1 The atomic solvent densities in $R$=10 Å cavities for a) $CH_3I$: $CH_3$ (black line), I (red line) and b) $CH_3CN$: $CH_3$ (black line), C (red line), N (blue line). The total solvent densities are also given (dashed red line).

in layers parallel to the cavity wall, methanol packs in a more perpendicular fashion. This is illustrated in Figure 2.2, which shows the individual atomic solvent densities for "$CH_3$", O, and H in methanol along with the total solvent densities in the $R$=10 and $R$=15 Å cavities. In bulk $CH_3OH$, there is a greater number of molecules per unit volume (0.02447 mol/ml) than in $CH_3CN$ (0.01915 mol/ml) and $CH_3I$ (0.01606 mol/ml);[115] thus, there are more $CH_3OH$ solvent molecules contained in the cavities than there are for the linear solvents, as indicated in Table 2.2. Methanol packs with two solvent layers in the 10 Å cavity; the first layer has the methyl groups oriented toward the hydrophobic wall, with the oxygen of the hydroxyl group pointing inward toward the center of the cavity. The second layer packs with the hydroxyl groups pointing in toward the first layer to capitalize on hydrogen bonding interactions. In the $R$=15 Å cavity, the first two solvent layers pack in the same manner as those in the 10 Å cavity; a third layer is less oriented, with one or two solvent molecules at the center within the three solvent layers. Note, however, that the peaks in the methyl density are separated by 3.85 Å, which is close to the $CH_3$ Lennard-Jones diameter of 3.775 Å (see Table 2.3.1). Thus, while hydrogen bonding influences the arrangement of the hydroxyl groups in the solvent layer, packing effects dominate the arrangement of the $CH_3$ groups in methanol.

## 2.6 Linear Solvents: Acetonitrile and Methyl Iodide

The entropy and free and internal energies were shown to be related to solvent packing. As the linear solvents, acetonitrile and methyl iodide, were found to pack in a similar fashion, the results for the two solvents are presented and discussed together in this section. In order to understand the driving forces for the time-dependent fluorescence signal, $\Delta A(d)$, $\Delta U(d)$, and $\Delta S(d)$ were calculated for the model dye molecule in both the ground and excited states.

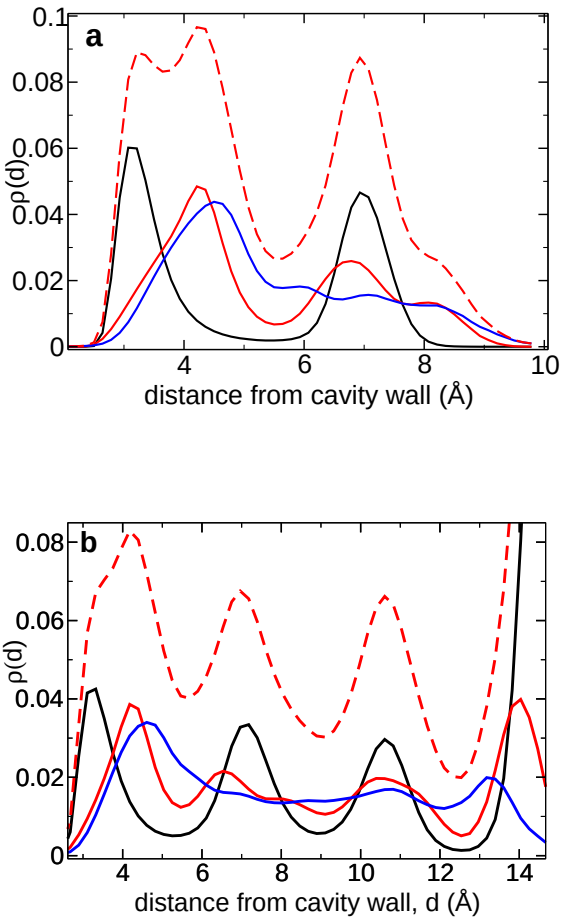


Figure 2.2 The atomic solvent densities: $CH_3$ (black line), O (red line), and H (blue line) for $CH_3OH$ in the a) $R$=10 and b) $R$=15 Å cavities. The summed atomic densities give the total solvent density (dashed red line).

### 2.6.1 Ground-state Solute in Linear Solvents: Free and Internal Energies

The relative free energies and internal energies for the nanoconfined $CH_3I$ and $CH_3CN$ systems have been calculated as a function of the solute center-of-mass position in the cavity, as described in Section 2.4. The results for the ground-state solute are plotted as a function of the solute center-of-mass distance from the cavity wall, $d$, for $R$=10 Å and 15 Å in Figures 2.3 and 2.4, respectively. Note that the free and internal energies are set to zero by convention (equations 2.12 and 2.13) for the position nearest to the cavity center, at $d$=9.75 and 14.75 for the $R$=10 and 15 Å cavities, respectively. For both cavity sizes and solvents, the free energy global minimum is near the cavity wall, at $d$=3.5 Å. In the smaller $R$=10 Å cavity, there is a difference of $\sim$0.4 kcal/mol between the free energy minimum near the cavity wall and the free energy of the solute located near the cavity center, around $d$=7.5 Å. A comparison with the solvent radial density shows that both of these free energy minima correspond to distances where the solute center-of-mass is located within a solvent layer. In addition, there is a local free energy minimum for both solvents in the $R$=10 Å cavity between the two solvent layers, near $d\sim$4.5 Å. There is a free energy maximum in both linear solvents around $d$=6 Å that gives rise to a barrier of $\sim$2.4 kcal/mol for the ground-state solute to move from the free energy minimum near the cavity wall to the local minimum in the second solvent shell.

In comparison to the $R$=10 Å cavities, the free energy curves for the ground-state solute in the $R$=15 Å cavities are much shallower, as seen in Figure 2.4, with differences between maxima and minima of $\sim$1 kcal/mol. For the $R$=15 Å cavities, all of the minima in the free energies correspond to a solute center-of-mass position located within a solvent layer. The global minimum in $\Delta A(d)$ is located at $d$=3.5 Å in both solvents, with local free energy minima located in the second layer of solvent, at $d$= 7.5 (7.75) Å in $CH_3I$ ($CH_3CN$) and within the third solvent layer, at $d$=11.75 (11.0) Å.

Thus, in all cases, the free energies are at a minimum in locations where solvent density is at or near a maximum.

The internal energies, on the other hand, are distinct from the free energies in the location of minima and their relationship to the solvent density. For the 10 Å cavities, the global minimum is located at $d$=4.75 Å (4.5 Å) in methyl iodide (acetonitrile). This corresponds to a position between the two solvent layers, *i.e.*, the solute molecule has one atom in each solvent layer such that the solute center-of-mass lies in between. Other local minima in $\Delta U(d)$ for $R$=10 Å are located at $d$=3.5 (3.75) Å, around the free energy global minimum within the first solvent layer, and at $d$=7.75 (7.25) Å, toward the interior of the cavity, with the solute center-of-mass slightly inside of the second solvent layer in $CH_3I$ ($CH_3CN$). For the $R$=15 Å cavities, the internal energy curves shown in Figure 2.4 are more difficult to interpret because the magnitude of the fluctuations in internal energy is not much larger than the statistical error. However, there are two discernible minima near the cavity wall, within the first solvent layer (around $d\sim$3.5 Å), and between the first two solvent layers ($d \sim$5 Å), with a small barrier between the two at $d$=4.5 (4.25) Å for $CH_3I$ ($CH_3CN$).

The differences between the free and internal energies are naturally due to entropic effects as indicated by Eq. 2.14. The large size of these differences indicate that entropy has a strong influence in determining the most likely position for the solute within the cavity.

### 2.6.2 Excited-state Solute in Linear Solvents: Free and Internal Energies

By understanding the differences between the energetic and entropic driving forces for the ground-state and excited-state solute, we can better understand the processes exhibited in the time-dependent fluorescence spectra. The salient difference between the free energies in the excited state and the ground state is that the global minimum is located near the center of the cavity for the solute in the excited state, whereas the

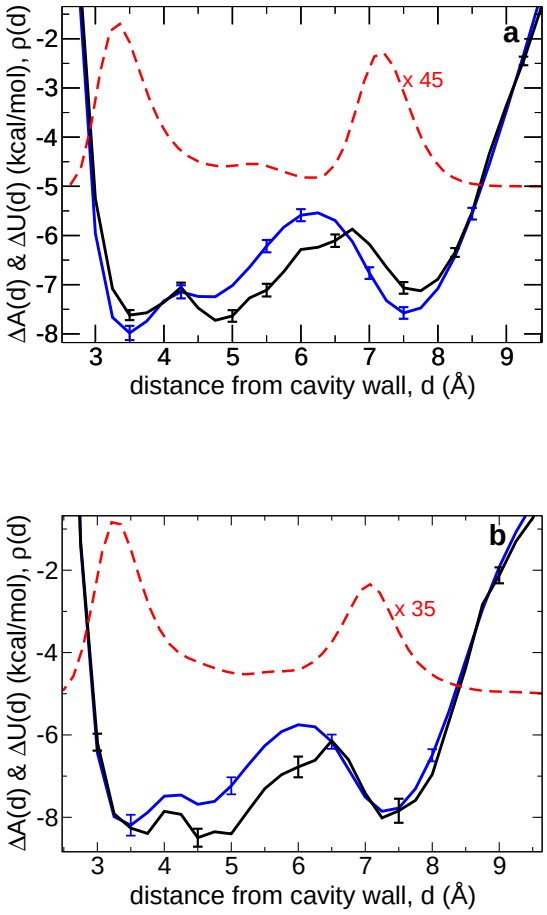


Figure 2.3 The free (blue line) and internal (black line) energies for the ground-state solute in a) $CH_3I$ and b) $CH_3CN$ in the 10 Å cavity. The scaled and shifted total solvent density is overlaid (dashed red line).

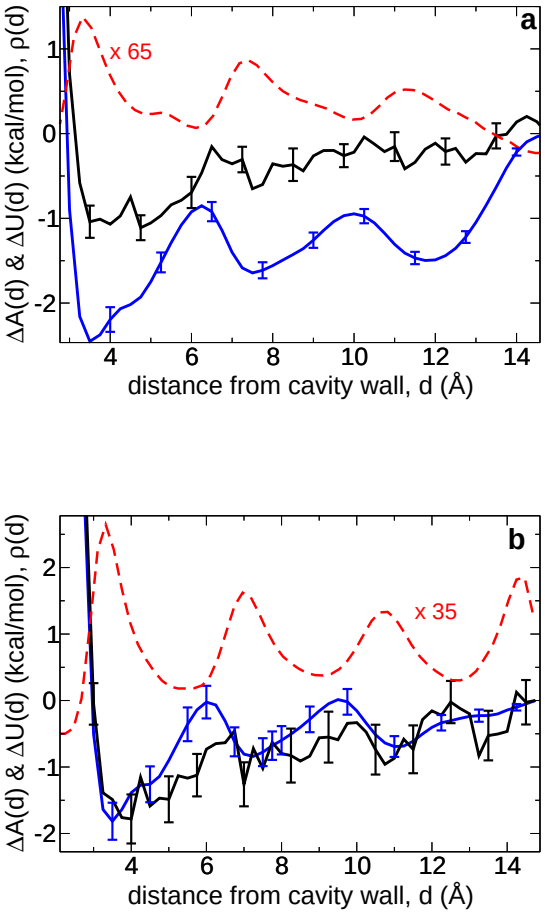


Figure 2.4 The free (blue line) and internal (black line) energies for the ground-state solute in a) $CH_3I$ and b) $CH_3CN$ in the 15 Å cavity. The scaled and shifted total solvent density is overlaid (dashed red line).

solute in the ground state has a global minimum near the cavity wall. The position of the free energy minimum for the two electronic states is a reflection of the position-dependent solvent polarity within the cavity. The solvent layer adjacent to the cavity wall is effectively less polar, and this is the favored position for the relatively non-polar solute in its ground electronic state. Upon excitation, the solute has a significant dipole moment, and is better solvated toward the interior of the cavity where the solvent is effectively more polar. In spite of the differences in the location of the free energy global minima for the two electronic states of the solute, the radial positions of the *local* minima are at approximately the same distances from the cavity wall for the ground and excited states, as can be seen by comparing Figs. 2.3 and 2.5 for $R$=10 Å, and Figs. 2.4 and 2.6 for $R$=15 Å.

Figure 2.5 shows the free and internal energies for the solute in the excited electronic state in $CH_3I$ and $CH_3CN$ solvents in the 10 Å cavity; the solvent density is also plotted in these figures. As seen in Figure 2.5a, in $CH_3I$ the two lowest free energy minima lie at the peaks of the solvent density: at $d$=3.5 and 7.5 Å. The global minimum in $\Delta A(d)$ for the excited-state solute, located at $d$=7.5 Å, lies 1.1 kcal/mol lower than the minimum next to the cavity wall, where the ground-state solute is at its global minimum in free energy. A local maximum at $d$=6.0 Å results in a free energy barrier of 1.8 kcal/mol for the solute to move from the inside of the cavity toward the wall. The barrier height is $\sim$0.7 kcal/mol for the excited-state solute to move away from the cavity wall toward the global free energy minimum at $d$=7.5 Å.

As seen in Figure 2.5a, there are notable differences in the free and internal energies, indicating a significant contribution from entropy to the free energy. Overall, energy differences in $\Delta U(d)$ are smaller than $\Delta A(d)$. In methyl iodide, two local minima in the internal energy lie at $d$=5.5 and 7.75 Å; the internal energies at these two points are equal within the statistical error. The minimum at 5.5 Å lies between the solvent layers, and corresponds to a region of relatively high free energy, indicating that solute positioned in this region is entropically disfavored (see Section 2.6.3 below).

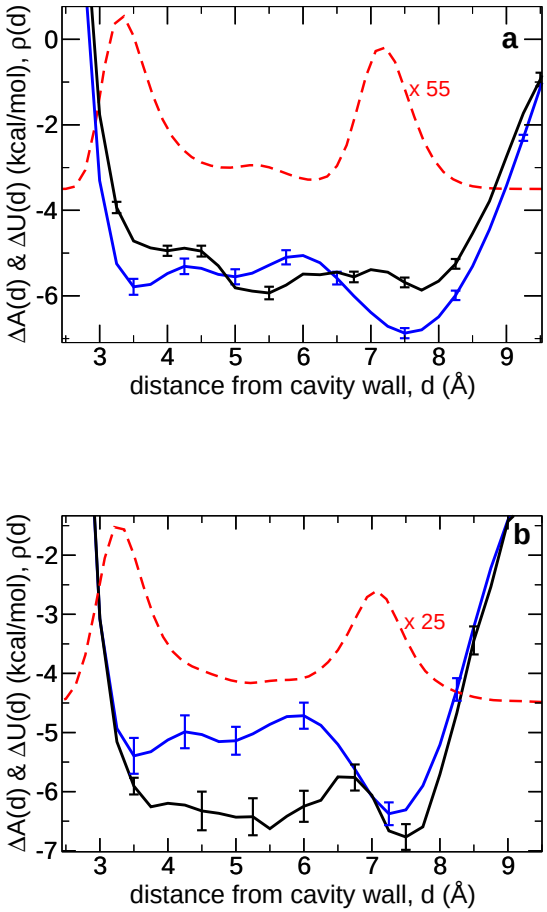


Figure 2.5 The free (blue line) and internal (black line) energies for the excited-state solute in a) $CH_3I$ and b) $CH_3CN$ in the 10 Å cavity. The scaled and shifted total solvent density is overlaid (dashed red line).

For acetonitrile in the 10 Å radius cavity, the global minimum in free energy is at $d$=7.75 Å; it is 1.0 kcal/mol lower in energy than another local minimum near the wall at 3.5 Å, as seen in Figure 2.5b. As in the case of $CH_3I$, there is a local maximum in $\Delta A(d)$ at $d$=6.0 Å in $CH_3CN$, with a barrier of 1.7 kcal/mol to move from the interior toward the cavity wall (the barrier is $\sim$0.7 kcal/mol when approached from the cavity wall toward the interior). It is interesting to note that the barrier heights are nearly identical for the two linear solvents. Also like the methyl iodide system, the internal energy in acetonitrile is relatively shallow from $d$=3.25-7.75 Å, with the exception of a local maximum at $d$=6.5-6.75 Å. It is notable that the barrier in the free energy is at a region where the internal energy is near its minimum, indicating a large entropic barrier for solute motion between positions in the first and second solvent layers.

The free and internal energies for the linear solvents $CH_3I$ and $CH_3CN$ in the $R$=15 Å cavity are plotted in Figure 2.6; the scaled and shifted solvent density is overlaid for comparison. Figure 2.6a shows that the solute in $CH_3I$ has two minima in the free energy at $d\sim$7.5 Å and 12 Å. These two minima correspond to positions within the second and third solvent layers. As with the methyl iodide system in the ground state, the internal energy is relatively featureless. There is a broad minimum from $d\sim$5 Å to the inside of the cavity ($d$=14.75 Å); the region near the cavity wall ($d\sim$3.5=5 Å) is energetically less favorable. In this way, the excited-state internal energy differs from that of the ground state, which has a minimum in $\Delta U(d)$ near the cavity wall. While the internal energy differences are rather small in methyl iodide, this is not the case for acetonitrile, however, as can be seen in Figure 2.6b. The internal energy of the excited state solute in $CH_3CN$ ($R$=15 Å) has a sharp global minimum at $d$=13.5 Å. This position also corresponds to a minimum in free energy. Other free energy minima lie around $d$=7.0 and 11.0 Å, at positions within the second and third solvent layers, respectively. As was seen for the ground-state solute, the magnitudes of the variations in $\Delta U(d)$ and $\Delta A(d)$ are much smaller for $R$=15 Å than for $R$=10 Å. In general, the energy differences are $\sim$1 kcal/mol, with the notable exception of the internal energy

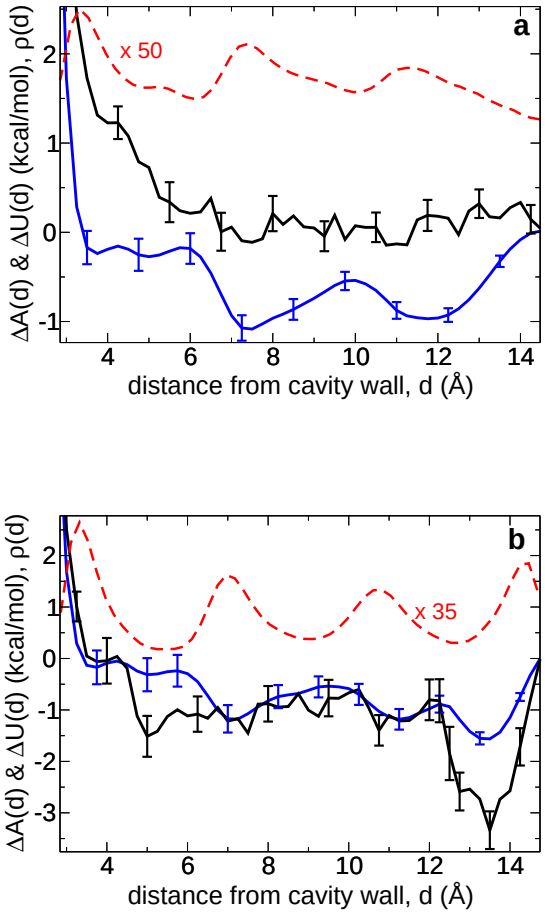


Figure 2.6 The free (blue line) and internal (black line) energies for the excited-state solute in a) $CH_3I$ and b) $CH_3CN$ in the 15 Å cavity. The scaled and shifted total solvent density is overlaid (dashed red line).

in acetonitrile, where the global minimum at $d$=13.5 Å is ∼2 kcal/mol below the next lowest local minima and ∼3 kcal/mol lower than the area next to the cavity wall.

### 2.6.3 Linear Solvents: Entropy

Clearly, the differences between $\Delta A(d)$ and $\Delta U(d)$, seen in Figs. 2.3-2.6 and discussed above, indicate an important role for entropic effects. Plots of $\Delta S(d)$ for the solute in both the ground and excited electronic states are given in Figure 2.7 for $CH_3I$ and $CH_3CN$ in the $R$=10 Å cavities. The entropy of the methyl iodide solution in the $R$=10 Å cavity is qualitatively identical for the solute in the ground state and excited state, as seen in Figure 2.7a. There are two maxima in $\Delta S(d)$ near the two positions of lowest free energy: next to the cavity wall, at $d$=3.25 Å, and within the second layer of solvent, at $d$∼7.5 Å. Entropy is lowest between the two solvent layers, $d$=5-6 Å. The total differences between the maxima and minima of $\Delta S(d)$ are slightly larger for the solute in the excited state.

In acetonitrile for $R$=10 Å, the entropy appears to be relatively independent of solute electronic state, as most values of $\Delta S(d)$ for the excited-state solute are the same within statistical error as those for the ground-state solute. As in $CH_3I$, the overall entropy differences in $CH_3CN$ between the global minimum, located between the two solvent layers ($d$∼5-6 Å), and the two maxima, where the solute is located within a solvent layer ($d$∼3 and 7 Å), appear to be slightly greater when the solute is in the excited state, though here they are within the statistical error. By comparing Figs. 2.7a and 2.7b, it can be seen that the entropy in $CH_3CN$ differs from the entropy in $CH_3I$ in that there is a region of high entropy from $d$=6.5-9.75 Å in $CH_3CN$, corresponding to the region from the second solvent layer inward to the center of the cavity, whereas for $CH_3I$, the entropy decreases for values greater than $d$=7.5 Å. The magnitude of the entropy changes in the 10 Å cavities are ∼6-7 cal/(mol·K), with $\Delta S(d)$ differences slightly larger in $CH_3CN$ than in $CH_3I$. These differences correspond to entropic contributions to the relative free energy of $T\Delta S \approx$1.8-2.1 kcal/mol.

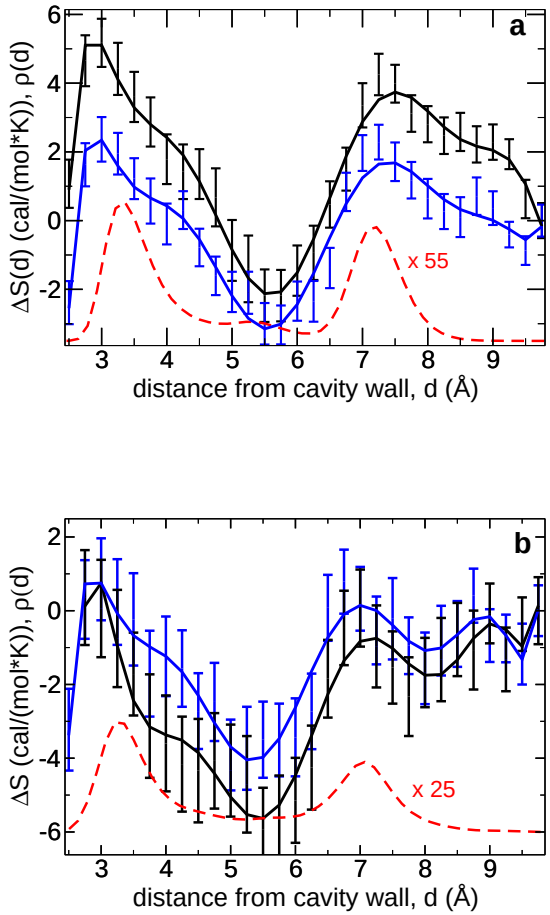


Figure 2.7 The entropy for a) $CH_3I$ and b) $CH_3CN$ solution in the 10 Å cavity, when the solute is in the ground state (blue line) and the excited state (black line). The solvent density is overlaid (dashed red line).

The entropy in $CH_3I$ in the $R$=15 Å cavity is plotted in Figure 2.8a; it can be seen that $\Delta S(d)$ for the solute molecule in both electronic states has a maximum near the cavity wall ($d$=3.0-3.75), with minima near the cavity center and around $d$=6.0 Å. The peaks in entropy coincide with regions of high solvent density, while areas between solvent layers correspond to minima in $\Delta S(d)$. The region between $d$=7 and 13 Å is higher than the minima by $\sim$3 cal/(mol·K) except around $d$=10 Å, where there is a local minimum. As with the $R$=10 Å cavities, the differences in $\Delta S(d)$ from the maximum near the cavity wall to the minimum between the two solvent layers is slightly greater for the solute in the excited state. In the 15 Å cavities, these entropy differences are somewhat greater: on the order of 8-9 cal/(mol·K) ($T\Delta S \approx$2.4-2.7 kcal/mol) for the excited state and 5-6 cal/(mol·K) ($T\Delta S \approx$1.5-1.8 kcal/mol) for the ground state, with larger entropy differences between the electronic states seen in the more polar acetonitrile solvent.

While the entropies are similar for the solute in both the ground and excited states in $CH_3I$ for $R$=10 and 15 Å, there is a dependence on electronic state in the entropy of the acetonitrile solution in the 15 Å cavity, as shown in Figure 2.8b. For both electronic states, there is a maximum near the cavity wall, with a minimum between the first two solvent layers. However, for the ground-state solute, there is a region of relatively higher entropy from $d$=6.75 Å to the center of the cavity, with slight dips around $d$=9.0 and 13.25. In contrast, when the solute is in the excited state, there is a marked drop in entropy in the region from $d$=12.25-14.25 Å. Thus, the free energy local minimum observed around $d$=13.5 Å for the excited-state solute in acetonitrile arises from the favorability of the internal energy, which has a global minimum at this position, as discussed above in Section 2.6.2 and seen in Figure 2.6.

## 2.7 Nonlinear Solvent: Methanol

For the linear solvents, it was found that entropy is at a maximum at radial positions where the solvent density is also at a maximum. Likewise, the free energy is generally at

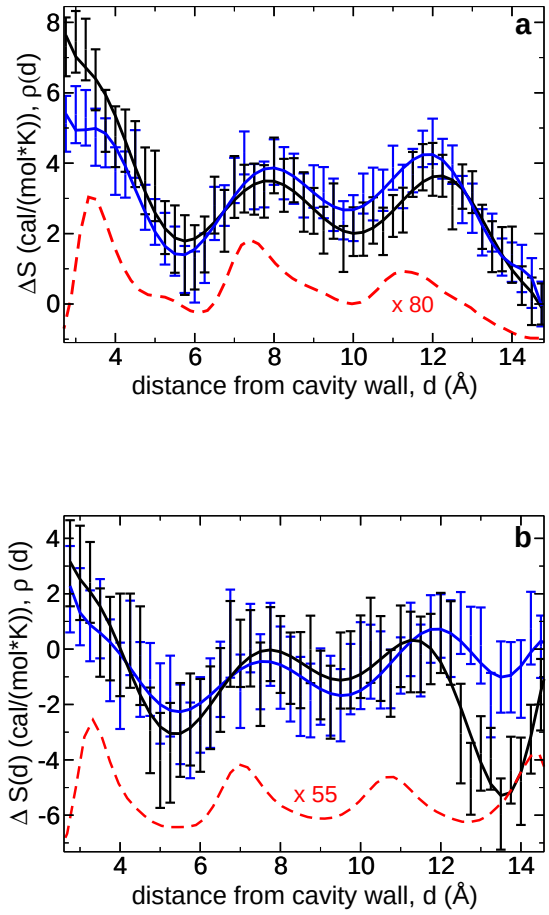


Figure 2.8 The entropy for a) $CH_3I$ and b) $CH_3CN$ solution in the 15 Å cavity, when the solute is in the ground state (blue line) and the excited state (black line). The solvent density is overlaid (dashed red line).

a minimum in the regions of maximum entropy and solvent density. The linear solvents, which have very similar solvent packing, also show similar trends for the entropy and free energy as a function of radial distance from the cavity wall. As discussed above in Section 2.5, methanol packs in a different manner than the linear solvents: the hydroxyl groups of the two outer solvent layers are oriented toward one another via hydrogen bonding interactions, while the methyl group layering is determined by packing effects. Given the differences in solvent packing, one might expect the entropy and free and internal energies of the ground- and excited-state solute in methanol to differ from those of the linear solvents.

### 2.7.1 Ground-state Solute in Methanol: Free and Internal Energies

The free and internal energies were calculated for the ground-state solute molecule in $CH_3OH$ solvent in the $R$=10 and 15 Å cavities. These are plotted in Figure 2.9 along with the total solvent density. In methanol, the solute in the ground state has a global free energy minimum near the cavity wall within the first solvent layer, at $d$=3.5 Å, for both the $R$=10 and 15 Å cavities. In the 10 Å cavity the global minimum near the wall lies 1.7 kcal/mol lower in energy than a local minimum at $d$=7.25 Å; there is a free energy barrier located at $d$=6.25 Å that is 3 kcal/mol higher than the minimum near the cavity wall.

Figure 2.9b shows that the free energy differences are smaller in the $R$=15 Å cavity than those seen in the $R$=10 Å cavity (Figure 2.9a). It can be seen that the free energy local minima for $R$=15 Å are $\sim$1 kcal/mol higher in energy than the global minimum near the cavity wall and are located at the center of the cavity and around $d$=7.5 and 10.75 Å. The latter two minima correspond to positions within the second and third solvent layers, respectively. As in the $R$=10 cavity, the free energy barrier in the $R$=15 Å cavity is located between solvent layers, at $d$=6.25 Å. This local maximum is 1.8 kcal/mol higher than the global minimum in $\Delta A(d)$, located near the cavity wall.

The internal energy in the 15 Å cavity is fairly shallow, but there is a discernible minimum at $d\sim$5.0 Å and a maximum around 12 Å. The minimum in $\Delta U(d)$ corresponds to a position between the first two solvent layers. In the $R$=10 Å cavity, the internal energy differences are more pronounced, as seen in Figure 2.9a, and there is a global minimum in $\Delta U(d)$ centered around $d$=5 Å, at a location between the two layers of methyl groups of $CH_3OH$ and at a position where the hydroxyl groups are at maximum density (*cf.* Figure 2.2). The global minimum in $\Delta U(d)$ in the $R$=10 Å cavity corresponds to an area where $\Delta A(d)$ is higher than its global minimum by over 1 kcal/mol. This indicates that the region between the two solvent layers is entropically disfavored.

### 2.7.2 Excited-state Solute in Methanol: Free and Internal Energies

Plots of $\Delta A(d)$ and $\Delta U(d)$ for the excited-state solute are presented in Figure 2.10 for the $R$=10 and 15 Å cavities. As in the linear solvents, the more polar excited-state solute is better solvated toward the interior of the cavity. In the 10 Å cavity, the free energy has a global minimum at $d$=7.25 Å, with a local minimum at 5.0 Å, as seen in Figure 2.10a. Figure 2.10b shows that the solute in the $R$=15 Å cavity also has free energy minima located around those same two positions, with additional ones at $d\sim$11.0 Å and at the cavity center (14.75 Å). Like the ground- and excited-state solute free energies in the linear solvents and the ground-state solute in methanol (Sections 2.6.1, 2.6.2, and 2.7.1), the free energy minima of the excited-state solute in $CH_3OH$ correspond to regions of maximum solvent density.

As with the other $R$=15 Å cavities, the energy differences are smaller ($\sim$2 kcal/mol) than those in the $R$=10 Å cavities and the internal energy is relatively shallow. There is, however, a minimum in $\Delta U(d)$ around $d$=5 Å and a maximum at 12 Å (see Figure 2.10b) for $R$=15 Å, in the same positions as the extrema in $\Delta U(d)$ for the ground-state solute in $CH_3OH$, $R$=15 Å (*cf.* Figure 2.9b). In the $R$=10 Å cavity, $\Delta U(d)$ has a minimum at $d$=4.75-5.0 Å, where the solute center-of-mass is nested within the

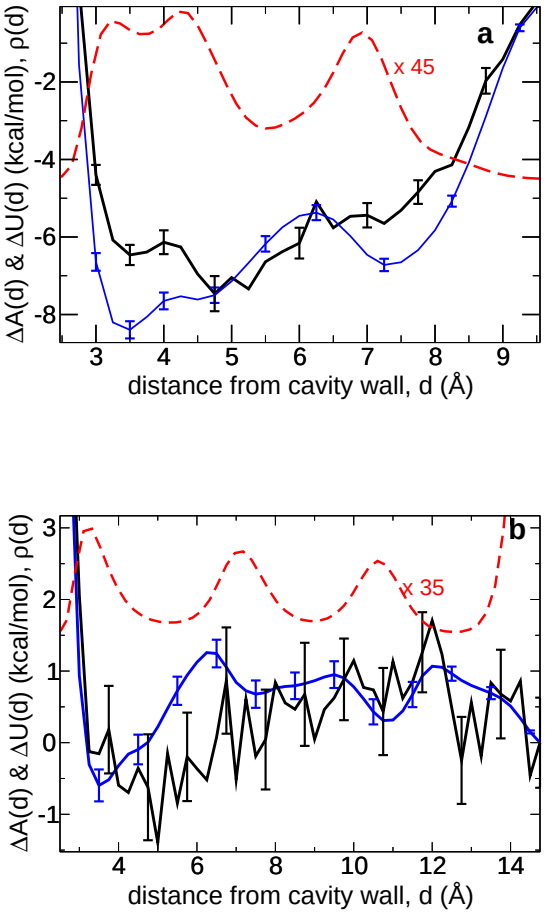


Figure 2.9 The free (blue line) and internal (black line) energies for the solute in the ground state in $CH_3OH$ in the a) 10 Å and b) 15 Å cavity. The scaled and shifted total solvent density is overlaid (dashed red line).

hydroxyl groups of both layers of solvent. This significant minimum in internal energy results in a local minimum in free energy at $d$=5.0 Å, but does not give rise to a global minimum in $\Delta A(d)$. Hence, it can be seen from comparing $\Delta U(d)$ and $\Delta A(d)$ in Figure 2.10a that the global minimum in free energy in the $R$=10 Å cavity at $d$=7.25 is entropically favored.

### 2.7.3 Methanol: Entropy

For the linear solvents, the entropies of the $R$=10 Å cavities were nearly identical, regardless of solute electronic state. In methanol, however, the entropy is different for solute ground and excited states, as shown in Figure 2.11a. The global maxima in entropy are located at the same radial distance as the respective free energy global minima of the two electronic states. Thus, for the ground-state solute, entropy is at a maximum near the cavity wall ($d$=2.75-3.5 Å) in the first layer of solvent, near the peak solvent density of the methyl groups. There is a local maximum in $\Delta S(d)$ when the solute center-of-mass is located in the second solvent layer, at $d\sim$7.5 Å. The global minimum is located at $d$=5.25-6.0 Å and is $\sim$10 cal/(mol·K) (T$\Delta$S$\sim$3 kcal/mol) lower in entropy than the global maximum. The excited state likewise has a global minimum in entropy in the region between the two solvent layers where solvent density is low ($d$=4.5-5.5 Å). This corresponds to the region where $\Delta U(d)$ is at its global minimum (see Figs. 2.9a and 2.10a), which indicates that entropy makes significant contributions in determining the most probable radial positions of the dye molecule in both the ground and excited states. For the excited-state solute, the entropy is at a global maximum from $d\sim$7-8 Å that is $\sim$12 cal/(mol·K) higher in entropy than the global minimum. Another local maximum is in the region near the cavity wall ($d$=3.0-3.75). As with the entropies of the linear solvents, the magnitude of differences in $\Delta S(d)$ are somewhat greater when the solute is in the excited state than in the ground state.

In the 15 Å cavities, differences in the radial entropy due to solute electronic state are less marked. The entropy in $CH_3OH$ for $R$=15 Å is plotted in Figure 2.11b, where

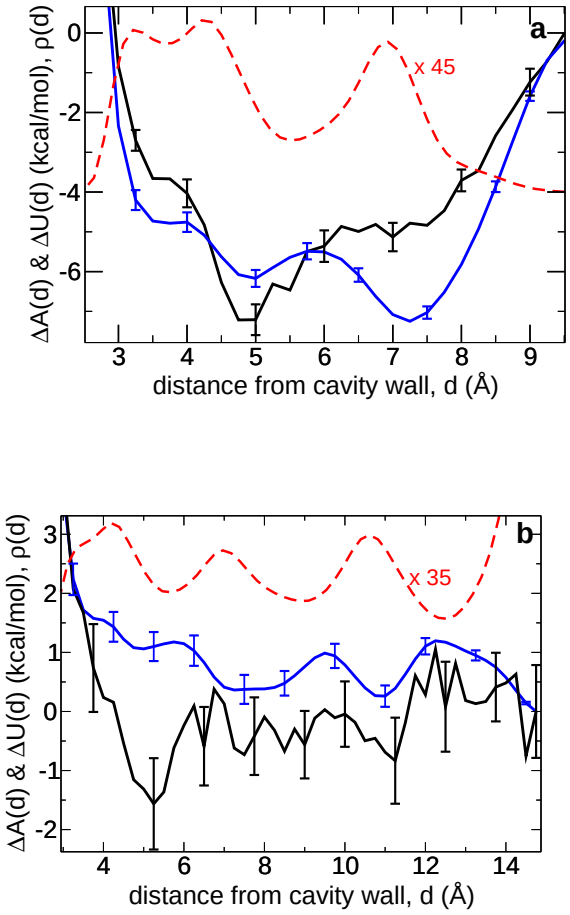


Figure 2.10 The free (blue line) and internal (black line) energies for the solute in the excited state in $CH_3OH$ in the a) 10 Å and b) 15 Å cavity. The scaled and shifted total solvent density is overlaid (dashed red line).

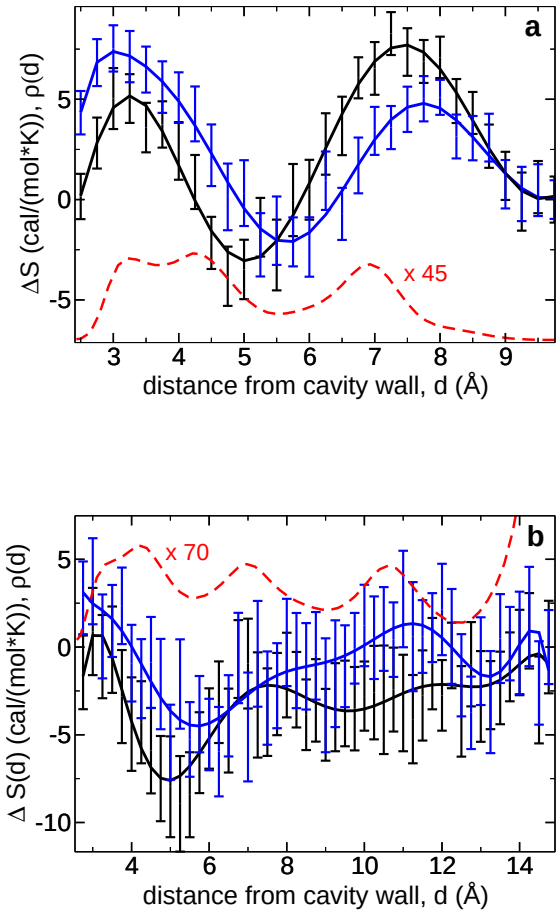


Figure 2.11 The entropy for $CH_3OH$ and solution in the a) 10 Å and b) 15 Å cavity, when the solute is in the ground state (blue line) and the excited state (black line). The solvent density is overlaid (dashed red line).

it can be seen that for the ground-state solute, $\Delta S(d)$ has a global minimum at $d\sim$5-6.5 Å, when the solute center-of-mass is located between the first two solvent layers. This region corresponds to a barrier in $\Delta A(d)$, but a minimum in $\Delta U(d)$, as can be seen in Figure 2.9b. Thus, the free energy barrier for ground-state solute movement away from the cavity wall in the $R$=15 Å cavity is an entropic one. There is another region of lower entropy for the ground-state solute at $d$=12.5-13.25 Å, near the center of the cavity. Entropy is at a maximum near the cavity wall and around $d$=11-14 Å; statistical errors lead to a broad maximum in $\Delta S(d)$ in the interior of the cavity. For the excited-state solute, the global minimum in entropy is located around $d$=5.25 and is 5-8 cal/(mol·K) (T$\Delta S\sim$1.5-2.4 kcal/mol) lower than other radial positions. This global minimum in $\Delta S(d)$ corresponds to a global minimum in $\Delta U(d)$, with the solute center-of-mass located between the two solvent layers. At other regions in the cavity, fluctuations in the entropy are within 2-3 cal/(mol·K) (T$\Delta$S$<$1 kcal/mol). Although the entropy appears relatively featureless between $d$=6-14.75 Å the unfavorable entropy at the position of minimum $\Delta U(d)$ ($d\approx$4.5-5.5 Å) indicates that entropy is the dominant factor in determining the locations of the free energy minima (see Figure 2.10b), which are located within the second and third solvent layers and in the center of the cavity.

## 2.8 Discussion

The results presented in Sections 2.6 and 2.7 demonstrate that entropy has a large influence on the free energy of the diatomic solute in solution: minima in free energy are located where entropy is at a maximum, and are distinct from the global minima in internal energy. A general trend in the radially-dependent energies, shown in Figs. 2.3-2.6, 2.9, and 2.10, is that $\Delta U(d)$ is typically at a minimum between solvent layers, while $\Delta A(d)$ is almost always at a minimum when the solute molecule is located within a solvent layer. The exceptions to free energies being located within solvent layers arise for the excited-state solute in $CH_3OH$ and $CH_3CN$ in 15 Å cavities, in which there is a free energy minimum near the center of the cavity, where the solute molecule

is surrounded by the third solvent shell. Because the entropy is at a maximum when the solute center-of-mass is located within a solvent layer, entropy makes the largest contributions to the free energy at these locations, leading to a strong correlation between solvent density and the free energy and entropy of all the systems studied.

In $CH_3I$ and $CH_3CN$ solvents for both the $R$=10 and $R$=15 Å cavities, the entropy has a local maximum within 0.5 Å of where the total solvent density is at its peak. On the other hand, while there is a correlation between entropy and solvent packing in $CH_3OH$, a non-linear solvent, the maxima in entropy to do not correspond as directly to solvent density peaks. As can be seen from Figure 2.11, the first $\Delta S(d)$ maximum next to the cavity wall correlates with the methyl density in the first solvent layer, but the other maximum lies closer to the interior of the cavity than the peak solvent density of the innermost layer. Nonetheless, entropy is at a global minimum in both the 10 and 15 Å cavities between the first two solvent layers where the solvent density is at a minimum. While the present work shows a strong relationship between the position-dependent entropy and local density, simulations by Mittal, Errington, and Truskett of hard sphere fluids in one- and two-dimensional confinement showed that total excess entropy of a confined hard sphere fluid generally has no dependence on local density profiles (fluid packing), but a strong dependence on the average (total) density of the fluid.[120]

Because of the relationship between solvent packing and $\Delta S(d)$, the origin of the solvent packing was explored. In addition, to investigate what governs $\Delta S(d)$ at the molecular level, several factors were considered. First, the translational entropy with a free volume model was considered,[121] but it did not match the qualitative trends in the calculated values of $\Delta S(d)$. Other possible sources to describe the molecular origins of the entropy that were explored include electrostatic interactions and contributions due to solute orientation. These are discussed below.

### 2.8.1 Electrostatic Effects

The similarities in entropy between the ground state and excited state solute molecule in every system studied, as seen in Figs. 2.7, 2.8, and 2.11, indicate that electrostatic effects - at least in the solute-solvent interactions - do not make significant contributions to the entropy. However, electrostatics may play a role in the way that solvent molecules pack in the cavity, which in turn is related to the entropy. Therefore, the effect of electrostatics was calculated directly, and the origin of the solvent packing motif in the linear solvents was explored.

To determine how charge and geometry influence solvent packing and entropy in $CH_3I$, simulations in the $R$=10 Å cavity were run with the solvent charges set to zero. The free and internal energies for this are plotted in Figure 2.12a along with the corresponding charged ground-state solute energies in $CH_3I$. With no charges on the solvent molecules, the solvent density profile of $CH_3I$ did not change distinguishably, indicating the solvent density is determined by packing effects rather than electrostatics. Moreover, the free energy is very similar to that of the ground-state solute in $CH_3I$; see Figure 2.12a. Thus, the resulting entropy shown in Figure 2.12b has the same shape, with maxima and minima in the same locations, as the ground- and excited-state entropies. The magnitude of $\Delta S(d)$, as with the ground state, is slightly smaller than that of the excited state, though the differences are close to the statistical error. The entropy of the system, then, in the linear solvents, like the solvent density, appears to be primarily influenced by the molecular geometry and packing of the solvent rather than interactions due to the charges.

### 2.8.2 Solute Orientation

In order to investigate the relationship between solvent packing, entropy, and solute orientation, two-dimensional plots of solute free energy and solute orientation were made, assuming separability of the two coordinates. Specifically, during the Monte Carlo simulations, solute atomic positions were recorded 80,000 times at even intervals

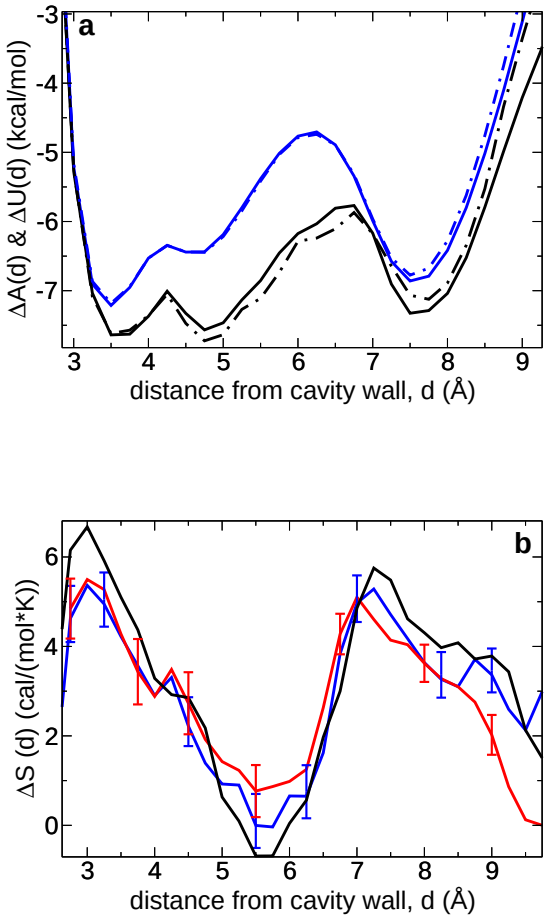


Figure 2.12 a) The shifted free (blue line) and internal (black line) energies for the solute in $CH_3I$ with solvent charges turned off, compared to the free (blue, dot-dash) and internal (black, dot-dash) energies of the ground-state solute in $CH_3I$. b) The entropy in $CH_3I$ when there are no charges in the solvent (red), compared to the ground-state solute (blue line) and excited-state solute (black line).

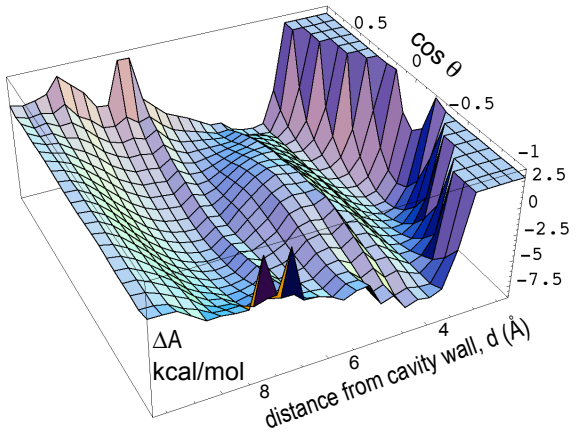


Figure 2.13 Free energy surface for the ground-state solute in $CH_3OH$ for $R$=10 Å. The rotational free energy is calculated as a function of $\cos\,\theta$, and the free energy is plotted versus distance from the cavity wall, $d$.

over the course of each run. The angle, $\theta$, between the solute molecular axis and the radial vector between the solute center-of-mass and the cavity center was calculated. Orientational probabilities from histograms of $\cos\,\theta$ with bin widths of 0.1 were used to calculate rotational free energies ($\Delta A(d, cos\,\theta)$=-RT ln $\frac{P(d,cos\theta)}{P_0}$). Figure 2.13 shows the free energy surface for the excited-state solute in $CH_3OH$ in the 10 Å cavity.[122]

The free energy surfaces indicate that the solute molecule is primarily oriented parallel to the cavity wall when it is located within solvent layers. In the parallel orientation, the area in which the molecule can rotate around the azimuthal angle, $\phi$, is maximized. On the other hand, when the solute molecule is located between solvent layers, it has a higher probability of being oriented perpendicular to the wall. In such an orientation, the volume through which the solute molecule rotates about the azimuthal angle $\phi$ is minimized. This gives a qualitative explanation why entropy may be at a maximum within solvent layers and next to the cavity wall. A more quantitative calculation of rotational entropy was carried out, using[123]

$$\Delta S_{rot}(d) = -k_B \int P(\theta, d)\ \ln P(\theta, d)\ \sin\theta\, d\theta \qquad [2.16]$$

as a measure of the rotational entropy.

Rotational entropies, using Eq. 2.16, were calculated for the various solvents and cavity sizes. Two examples of the rotational entropies, in $CH_3OH$, $R$=10 Å and $CH_3CN$, $R$=15 Å, are plotted along with the total entropies in Figs. 2.14 and 2.15. The rotational entropies for the ground- and excited-state solute in $CH_3OH$ are identical to each other. As seen in Figure 2.14, the rotational entropies have a global minimum, located between the methyl group solvent density peaks at $d\sim$4.5-5.5 Å (*cf.* Figure 2.2a and 2.11a), that coincides with the global minimum in the total entropy. The maxima in $\Delta S_{rot}(d)$, located around $d$=4 Å and from $d\sim$6.5-9 Å, also correspond to regions of high total entropy. However, while the location of the global maximum in $\Delta S(d)$ is dependent on solute electronic state, the maxima in rotational entropy are independent of electronic state. Also, the differences in maxima and minima in the rotational entropy are not as pronounced as the apparent differences in the total $\Delta S(d)$, which have rather larger uncertainties due to statistical errors.

Like the entropy in $CH_3OH$ solvent in the $R$=10 Å cavity, the total $\Delta S(d)$ in $CH_3CN$ solvent in the $R$=15 Å cavity is dependent on the solute electronic state. In $CH_3CN$, $R$=15 Å, there is a global minimum in $\Delta S(d)$ located at $d\sim$13 Å for the excited-state solute (coinciding with a sharp minimum in $\Delta U(d)$, as seen in Figure 2.6b), whereas for the ground-state solute, entropy in this location is just at a local minimum. As can be seen in Figure 2.15, the rotational entropies in $CH_3CN$, $R$=15 Å are very similar to the total entropies. The magnitude of the differences in $\Delta S_{rot}(d)$ and total $\Delta S(d)$ are comparable, and the maxima and minima coincide. Remarkably, the rotational entropy qualitatively reproduces the electronic-state dependence in $\Delta S(d)$ around $d$=13 Å, although the magnitude of the entropy differences are somewhat smaller. The only region where there are noticeable differences between the rotational and total entropies is in the region near the cavity wall, around $d$=3 Å.

Rotational entropy, like the total entropy, is at a minimum between the solvent layers, where there is higher probability that the solvent lies perpendicular to the cavity

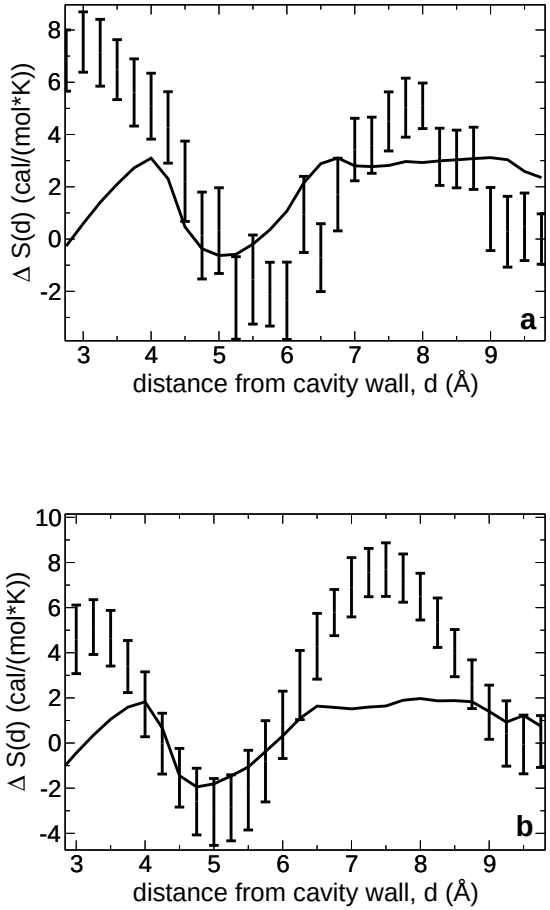


Figure 2.14 The total (black error bars) and shifted rotational (solid black line) entropies for the a) ground- and b) excited-state solute in $CH_3OH$, $R$=10 Å.

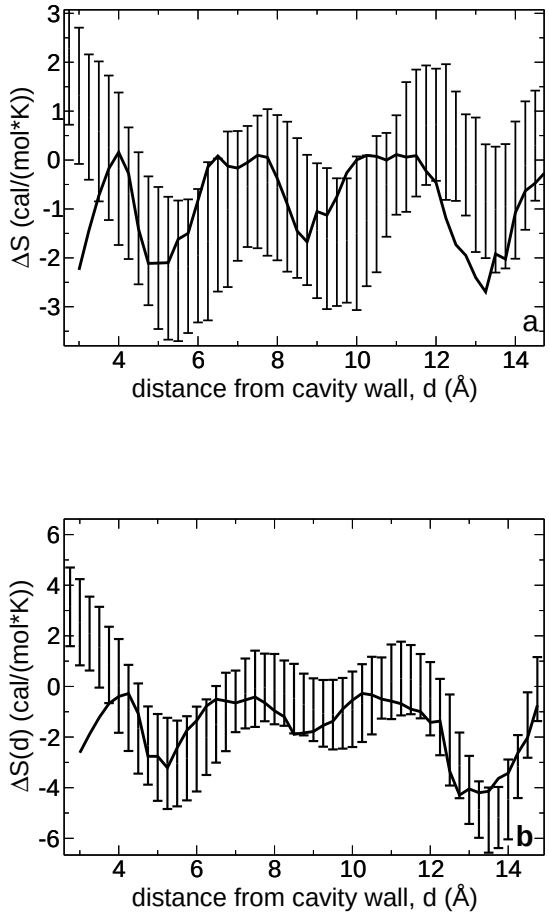


Figure 2.15 The total (black error bars) and shifted rotational (solid black line) entropies for the a) ground- and b) excited-state solute in $CH_3CN$, $R$=15 Å.

wall. With Eq. 2.16, entropy is maximized when the probability is high for the solute to be oriented parallel to the wall. Although the calculated total entropy is highest near the wall, very few values of $\theta$ are probable, and so the rotational entropy is lower relative to other regions in the cavity where a greater range of $\theta$ values are accessible to the solute. The discrepancies between the total and rotational entropy at distances very near the cavity wall may be due to insufficient sampling in the repulsive region, $d \leq$3.0 Å, and/or other entropic contributions that give rise to higher values of total entropy. In fact, the rotational entropy is at a maximum within 0.5 Å of the free energy minimum near the cavity wall, which can be seen by comparing Figs. 2.14 and 2.15 with Figs. 2.10 and 2.4, respectively. Meanwhile, the total entropy has a maximum around $d$=3 Å, where the free and internal energies are high due to repulsive interactions with the wall. Except for very small values of $d$, the rotational entropies describe the trend of the overall entropy well. The magnitude of differences in $\Delta S_{rot}(d)$ are generally somewhat smaller than the magnitude of those in the total $\Delta S(d)$, though the magnitude in $\Delta S(d)$ is somewhat indefinite due to statistical errors. Moreover, the rotational entropy calculated by Eq. 2.16 is a crude measure of rotational entropy, and assumes separability between $\theta$ and the azimuthal angle $\phi$. Given these considerations, there is remarkable agreement between the total and rotational entropies, indicating that rotational contributions are the dominant factor in the total $\Delta S(d)$.

## 2.9 Conclusions

Monte Carlo simulations were used to calculate free energies, internal energies, and entropies of a model dye molecule in its ground and excited states in $CH_3I$, $CH_3CN$, and $CH_3OH$ solvents confined in 10 and 15 Å radius spherical, hydrophobic cavities. The primary conclusions of this work are: 1.) Global minima in $\Delta A(d)$ are distinct from global minima of $\Delta U(d)$, indicating that the most likely position for the solute molecule is governed by entropy. 2.) Free energy global minima correspond to regions of maximum entropy. 3.) Entropy is at a maximum when the solute center-of-mass

is located in a region of high solvent density. 4.) When the solute center-of-mass is located in a solvent layer, the solute has a higher probability of being oriented parallel to the wall; thus, rotational entropy makes substantial contributions to the total calculated $\Delta S(d)$. 5.) Electrostatic interactions and translational entropy were found to have little effect on the total entropy.

Entropic contributions to free energy are significant in determining the most probable position of the solute. In these systems, the more polar excited-state model dye molecule is better solvated toward the center of the cavity, where the solvent is more polar. In fact, the magnitudes of differences in $\Delta S(d)$ within the cavities were greater in solvents with higher "bulk" polarity. We have shown that the position-dependent solvent polarity in the nanoconfined solvents, as manifested in the different locations for ground- and excited-state solutes, exhibits an interplay between charge interactions and entropic effects. Electrostatic interactions, which can be straightforwardly seen in $\Delta U(d)$, are most favorable when the solute center-of-mass is between two solvent layers, with one atom of the diatomic dye model in each solvent layer. It is entropic considerations that minimize the free energy at positions where the solute center-of-mass is in the solvent layers, but the internal energy ultimately determines in which solvent layer the global free energy minimum is located. At the positions of high entropy located within a solvent layer, the solute molecule has a high probability of being oriented parallel to the cavity wall. In such an orientation, rotation of the solute is maximized; the increased solute rotational freedom is the primary source of the higher entropies observed when the solute center-of-mass is positioned within a solvent layer.

The free energies of the ground-state and excited-state solute were previously shown to rationalize the longer time scales in time-dependent fluorescence spectra of this model dye in nanocavities.[57,58] Namely, shorter time scales in the normalized Stokes shift are due to inertial motion and solvent reorientation, while the longest time scale can be attributed to diffusion of the more polar excited-state molecule away from the cavity wall toward the interior. This study explored the driving force for the diffusive

time scale, indicating that entropy strongly influences solvation dynamics in charge-transfer processes in nanoconfined solvents.

# Chapter 3

## Infrared Spectra of a Proton-Transfer Complex in Nanoconfined Methyl Chloride Solution

The previous chapter explored the driving forces behind one spectroscopic method used to probe confining frameworks, time-dependent fluorescence. In this chapter, the same confining framework, a spherical, hydrophobic cavity, is considered, but a different spectroscopic method is explored: infrared absorption spectroscopy. In this case, a model proton transfer complex in methyl chloride solution confined in a 12 Å radius cavity is studied. The instantaneous frequencies and infrared spectra are calculated using mixed quantum-classical dynamics for 5 different cases of the model, in which the energy offset was varied such that a number of different proton transfer equilibrium reaction free energy values were afforded.

A model proton transfer complex is used in this work. Proton transfer reactions are of considerable interest as they are ubiquitous in chemistry, physics, and biology. Their importance also extends to catalysis, including efforts to develop microporous and mesoporous materials, for example, as solid acid catalysts (see Chapter 4). Our understanding of proton transfer reactions in such porous materials is currently limited, with only a small number of experimental[37–41,41,43,44,68,70,71,76] and theoretical[62,63,77,124] studies having addressed the issue. By studying the effect that confining environments have on proton- and charge transfer reactions, the development of new catalysts can be guided.

## 3.1 Spectroscopic Studies of Proton Transfer

A variety of spectroscopic methods are used to probe proton transfer processes in confining environments. Experimental studies have focused almost completely on excited-state proton transfer since the reaction can be straightforwardly initiated. Pump-probe experiments[67,70] of optical chromophores in reverse micelles[37–39,41,41,43,44,68,76] and sol-gels[70,71] found that deprotonation rates decreased with decreasing pore size, and overall were slower than in neat solvent. These excited-state proton-transfer dynamics experiments provide information about the confining framework and its effects on solvation.

Although experimental studies of proton transfer in nanoconfined solvents have considered excited-state proton transfer almost exclusively, most proton transfer reactions important in catalysis occur in the ground electronic state. The dynamics of such ground-state proton transfer reactions are more difficult to probe spectroscopically; however, linear and/or nonlinear vibrational spectroscopies have some promise for addressing this issue. In particular, vibrational spectroscopies are sensitive to local environments, and have already been shown to provide extensive information about liquid structure and hydrogen bonding dynamics. Spectral diffusion data reflect the microscopic dynamics and can be probed by infrared photon echo experiments. Recent studies of numerous properties of condensed phases, including hydrogen-bond strength,[125–128] structure,[129–132] and dynamics,[133–135] as well as reorientational,[125,136] solvation,[135,137,138] and proton transfer[139–142] dynamics, have been carried out with linear and non-linear[143] vibrational spectroscopies. Several examples of such work have been carried out on nanoconfined liquid systems.[136,144–146]

In addition to the studies of proton transfer discussed above, infrared spectra in general are frequently used to characterize confined solvent systems, including those with a solute vibrational chromophore.[147–156] Thus, it is useful to consider what the vibrational spectra of a ground-state proton transfer reaction complex can tell us about the reaction

equilibrium and dynamic properties. Experimental measurements of the infrared spectra of proton transfer complexes in bulk solvents have revealed a number of interesting features. For example, Zundel and co-workers have found that for a large number of systems a broad background appears generally in the range of 3000-800 $cm^{-1}$ when proton transfer is possible.[157] The width and location of these "infrared continuum" (also called "Zundel polarization") bands vary by system, and are attributed to the proton polarizability of the hydrogen bond in the reaction complex. These features have also been found in simulations of an excess proton in water.[139,142,158–164] and a Mannich base system.[165] This work involves the calculation of ground-state vibrational spectra of a model proton transfer complex based on a hydrogen-bonded phenol-amine complex that undergoes intermolecular proton transfer.

## 3.2 Proton Transfer in Nanocavities

Previous work by the Thompson group on the model proton transfer complex in nanoconfined solvent have involved Monte Carlo studies on the reaction free energies as a function of solute position[62] and molecular dynamics simulations to probe the proton transfer mechanism and dynamics in the vibrationally adiabatic limit.[63] Like the work in this chapter, these two studies involved the proton transfer complex in nanoconfined $CH_3Cl$ solution in spherical, hydrophobic cavities. In the Monte Carlo study, the probability distribution of products and reactants was determined by constraining the proton to a bond length characteristic of either products or reactants, then sampling the position of the complex within both the $R$=10 Å and $R$=15 Å nanocavities. It was found that in the $R$=10 Å cavity, the less polar reactants had a distribution centered around $d$=3.5 Å, where $d$ is the distance from the cavity wall. Meanwhile, the more polar products were distributed closer to the interior of the cavity, around $d$=7 Å. In the larger $R$=15 Å cavities, the reactants likewise had a distribution peaked around $d$=4 Å. However, the products had a bimodal distribution in the cavity interior, with a larger peak around $d$=7.5 and a smaller one at $d$=11 Å. The probability distributions

for the proton transfer complex are qualitatively similar to those seen for the model dye molecule, discussed in Chapter 2, in which the ground-state dye molecule is preferentially solvated in the first solvent layer near the cavity wall, while the excited-state solute has lower free energy toward the middle of the cavity, in the inner solvent layers.

Using Monte Carlo methods (Ref. 62), the reaction free energies of the complex located at different distances, $d$, within the cavity were calculated. It was found that, at reaction complex positions near the cavity wall, the free energy of proton transfer is endothermic. Meanwhile, for positions near the interior of the cavity, the free energy of reaction is exothermic. This corroborates the probability distributions found for products and reactants. Whether solvent reorganization (for the proton transfer reaction) takes place before solute diffusion toward the interior/exterior or vice-versa, or as a concerted mechanism, was explored with non-equilibrium molecular dynamics in Ref. 63. It was found that all three mechanisms take place, with a concerted mechanism being the least probable. This work also explored the effect of cavity size on the proton transfer reaction (using $R$=10, 12, and 15 Å cavities), and concluded that the free energy of reaction becomes more exothermic as cavity size increases; furthermore, the proton transfer rates increase with larger cavity sizes. In this work, only one cavity size, $R$=12 Å was considered. Equilibrium molecular dynamics trajectories were used to calculate the infrared spectra of the proton transfer complex in $CH_3Cl$ solution. The methods are detailed below in Section 3.3. Results for the five proton transfer cases considered are presented in Section 3.4. A discussion of spectral features, approximations and contributions to the spectra, and proton transfer equilibria and rates follows.

## 3.3 Methods

### 3.3.1 System

The proton transfer reaction complex studied in this work is a simplified model of a phenol-amine system, based on a model developed by Borgis.[166,167] In this work, the electronic structure of the reaction complex is represented by a two valence bond

Table 3.1 Parameters for the *in Vacuo* Potentials of the Neutral and Ionic Valence Bond States for the Proton Transfer Complex.

| Parameter | | Neutral (N) | Ionic (I) |
|---|---|---|---|
| $D_{N/I}$ | (eV) | 5.1 | 4.2 |
| $b_{N/I}$ | $Å^{-1}$ | 1.568 | 1.5 |
| $r^{eq}_{N/I}$ | Å | 0.9572 | 0.90 |
| $B_{N/I}$ | (eV) | 0.04 | 0.05 |

(VB) state model composed of reactant- and product-like fixed-charge VB states.[62] The potential energy of the proton in the neutral valence bond state (reactants), $V^0_N$ is given by

$$V^0_N(r_{OH}; R_{ON}) = D_N \left[1 - e^{-b_N(r_{OH} - r^{eq}_N)}\right]^2 + \frac{B_N}{r^6_{HN}}. \qquad [3.1]$$

The O-H-N angle is held linear, and the heavy atom (O–N) bond distance is fixed at $R_{O-N}$ = 2.7 Å, effectively modeling a rigid intramolecular proton transfer system. Thus, the H-N distance is a function of the O-N and O-H distances: $r_{HN} = R_{ON} - r_{OH}$. The potential energy of the proton in the ionic valence bond state (reactants), $V^0_I$ is given by

$$V^0_I(r_{OH}; R_{ON}) = \Delta V_0 + D_I \left[1 - e^{-b_I(r_{HN} - r^{eq}_I)}\right]^2 + \frac{B_I}{r^6_{OH}}. \qquad [3.2]$$

Both valence bond potentials (Eqs. 3.1 and 3.2) involve a Morse potential term that describes the proton-oxygen (proton-nitrogen) bond for reactants (products) and a $\frac{B}{r^6}$ repulsive term as the proton approaches the opposite atom - nitrogen (oxygen) in the case of reactants (products); $\Delta V_0$ describes the gas-phase offset (see below). The parameters for the potentials $V^0_N$ and $V^0_I$ are given in Table 3.1.

Within this model, the equilibrium constant for the reaction in solution can be "tuned" by changing the gas-phase offset, $\Delta V_0$, the energy difference between the two VB states. The central case ($PT$) considered is based on a value of $\Delta V_0 = 0.7$ eV that permits significant proton transfer over the simulation time scale and for which reactants and products are nearly equal in free energy. However, data obtained using a

Table 3.2 Energy Offsets, Reaction Free Energies, and Equilibrium Constants for the Five Proton Transfer Reaction Complex Cases.

| Case | Description | $\Delta V_0$ (eV) | $\Delta G_0$ (kcal/mol) | $K_{eq}$ |
|---|---|---|---|---|
| $P$ | Products only | 0.45 | – | – |
| $PT_P$ | Products Favored | 0.65 | -1.0 $\pm$ 0.3 | $\sim$7 |
| $PT$ | | 0.7 | 0.1 $\pm$ 0.2 | 0.8 |
| $PT_R$ | Reactants Favored | 0.75 | 0.8 $\pm$ 0.3 | 0.2 |
| $R$ | Reactants only | 0.95 | – | – |

number of other gas phase offsets, $\Delta V_0 = 0.45$, 0.65, 0.75, and 0.95 eV, were also studied in this work, in order to determine how the spectrum depends on the equilibrium constant and chemical exchange, as discussed in Section 3.4. The energy offsets used in this work are summarized in Table 3.2; Figure 3.1 shows the gas phase potentials as a function of O-H distance for the various cases considered.

The solvent and solute molecules interact through Lennard-Jones and Coulombic interactions; the parameters for both the proton transfer complex and $CH_3Cl$ solvent are detailed in Table 3.3. The Lennard-Jones potential, $V_{ij}$, between two interaction sites $i$ and $j$ is given by:

$$V_{ij} = 4\epsilon_{ij}\left[\left(\frac{\sigma_{ij}}{r_{ij}}\right)^{12} - \left(\frac{\sigma_{ij}}{r_{ij}}\right)^{6}\right] + \frac{q_i\, q_j}{r_{ij}}. \qquad [3.3]$$

The reaction complex and solvent molecules interact with the spherical cavity only through Lennard-Jones interactions integrated over the infinite region surrounding the cavity,[54,55] as detailed in Chapter 2 and given in Eq. 2.5. For these calculations, one reaction complex was dissolved in the $CH_3Cl$ solvent confined in a spherical hydrophobic cavity of radius $R = 12$ Å. The density of the confined solution was taken to be $\rho \simeq$ 0.8 g/cm$^3$ ($\rho_{CH_3Cl,bulk}$=0.911[115] g/cm$^3$), resulting in a total of 49 molecules (including the reaction complex).

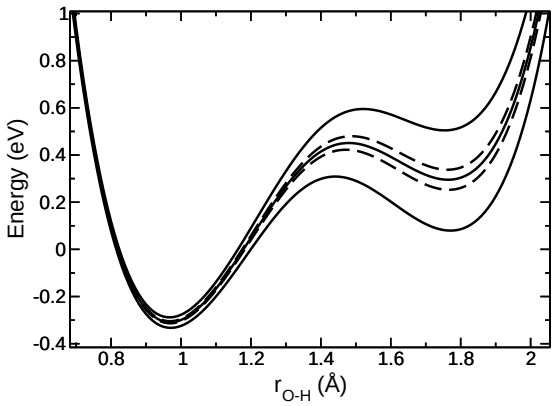


Figure 3.1 The gas phase electronic ground-state proton potential energy curves for the different cases considered are plotted as a function of O-H distance. Results are shown for, from bottom to top, $P$ ($\Delta V_0 = 0.45$ eV), $PT_P$ ($\Delta V_0 = 0.65$ eV), $PT$ ($\Delta V_0 = 0.7$ eV), $PT_R$ ($\Delta V_0 = 0.75$ eV), and $R$ ($\Delta V_0 = 0.95$ eV).

Table 3.3 Charges and Lennard-Jones Parameters for Proton Transfer Complex and $CH_3Cl$ Solvent.

| site | $\epsilon$ (kcal/mol) | $\sigma$ (Å) | q ($\|e\|$) | $r_{ij}$ (Å) |
|---|---|---|---|---|
| *$CH_3Cl$* | | | | |
| $CH_3$ | 0.2364 | 3.775 | +0.25 | |
| Cl | 0.4145 | 3.48 | -0.25 | 1.781 |
| *Proton Transfer Complex:* | *neutral state* | | | |
| Ph-O | 0.09495 | 3.5 | -0.5 | |
| H | 0.0 | | +0.5 | variable |
| $NR_3$ | 0.09495 | 3.5 | 0.0 | 2.7 |
| *Proton Transfer Complex:* | *ionic state* | | | |
| Ph-O | 0.09495 | 3.5 | -1.0 | |
| H | 0.0 | | +0.5 | variable |
| $NR_3$ | 0.09495 | 3.5 | +0.5 | 2.7 |

### 3.3.2 Simulation Details

Vibrationally adiabatic mixed quantum-classical molecular dynamics simulations were used to calculate the infrared spectrum of the proton transfer complex. In this approach, the motions of the solvent molecules and solute heavy atoms are governed by the classical Hamiltonian

$$H_n(\mathbf{P}, \mathbf{Q}, \mathbf{p_e}, \mathbf{e}) = \sum_i \frac{\mathbf{P}_i^2}{2m_i} + \sum_i \frac{\mathbf{p}_{e,i}^2}{2I_i} + E_n(\mathbf{Q}, \mathbf{e}), \quad [3.4]$$

where $\mathbf{Q}_i$ and $\mathbf{e}_i$ are the center-of-mass coordinates and orientational unit vector of molecule $i$ with conjugate momenta $\mathbf{P}_i$ and $\mathbf{p}_{e,i}$, respectively. The molecule $i$ mass and moment of inertia are denoted by $m_i$ and $I_i$, respectively. The potential term, $E_n(\mathbf{Q}, \mathbf{e})$, is the vibrationally adiabatic energy obtained by solving the one-dimensional proton vibrational Schrödinger equation

$$\hat{h}_r \phi_n(r; \mathbf{Q}, \mathbf{e}) = E_n(\mathbf{Q}, \mathbf{e}) \phi_n(r; \mathbf{Q}, \mathbf{e}) \quad [3.5]$$

for fixed $\mathbf{Q}$ and $\mathbf{e}$ at every time step. Here, the proton Hamiltonian is given by

$$\hat{h}_r(\mathbf{Q}, \mathbf{e}) = \frac{\hat{p}_r^2}{2m_H} + V_g(\hat{r}, \mathbf{Q}, \mathbf{e}), \quad [3.6]$$

where $r$ is the O-H distance and $V_g(\hat{r}, \mathbf{Q}, \mathbf{e})$ is the electronic ground-state potential energy of the system.

The Schrödinger equation is solved using the Lanczos algorithm,[168,169] where the three lowest vibrational states were converged. A sinc-function discrete variable representation basis[170] was used with a grid spacing of $\delta r = 0.0284$ Å and a potential cutoff of 3.5 eV, giving 49-50 grid points. For each value of the gas phase offset, four or eight 15 ns trajectories (see Section 3.4) were run for data collection with a time step[116] of 1 fs. The temperature was maintained by a Nosé-Poincare thermostat;[171] the average temperature was $\sim 260$ K. The data collection run was preceded by a two-stage warmup consisting of a period of classical dynamics alone followed by a mixed quantum-classical equilibration; the temperature was maintained using velocity rescaling for the first half of each warmup stage. Different initial conditions were achieved

by varying the length of the warmup periods: between 0.5-1 ns for the classical equilibration and 0.2-0.8 ns for the mixed quantum-classical warmup.

### 3.3.3 Diabatic States and Calculation of Infrared Spectra

It was found that both the $n = 0 \rightarrow n = 1$ and $n = 0 \rightarrow n = 2$ vibrational transitions contribute to the O-H and N-H stretches in the characteristic ranges (3300-3450 cm$^{-1}$). This is discussed in further detail in Section 3.4. Briefly, for different ranges of the solvent coordinate, either the $n = 1$ or $n = 2$ eigenstate is localized in the same product/reactant well as the ground state, while the other is localized in the opposite well. This is illustrated in Figure 3.2, which shows the instantaneous proton potentials along with eigenvalues and eigenfunctions of the $n = 0, n = 1$, and $n = 2$ states for the reaction complex in the reactants well at two different values of the solvent coordinate, $\Delta$E, defined below in Eq. 3.12. At higher absolute values of the solvent coordinate (-9.5 kcal/mol $< \Delta$E $<$ 10.4 kcal/mol, as seen below in Figure 3.3), the $n = 1$ vibrational state is localized in the same well as the ground state, while for solvent coordinate values of lower magnitude, the $n = 1$ and $n = 2$ states change character and the $n = 2$ vibrational state is localized above the ground state. Thus, the $n = 0 \rightarrow n = 1$ and $n = 0 \rightarrow n = 2$ vibrational transitions combine to form diabatic surfaces; the surfaces are plotted in Figure 3.3 from data of the instantaneous transition frequencies as a function of solvent coordinate.

Infrared absorption is dependent on the magnitude of the dipole moment: the oscillator strength, which is a measure of absorption intensity, is directly proportional to the square of the transition dipole moments. In the case of these diabatic states, the transition dipole moments are greatest for transitions from the ground state ($n = 0$) to the diabatic state located in the same well, which we shall call $D_1$ (represented by the solid lines in Figure 3.3). On the other hand, the transition dipole moments from the ground state to the diabatic state located in the opposite well, which we shall call $D_2$, $\langle D_2|\mu|0\rangle$, are quite small: typically $\sim 10^{-3}$ times smaller than $\langle D_1|\mu|0\rangle$.

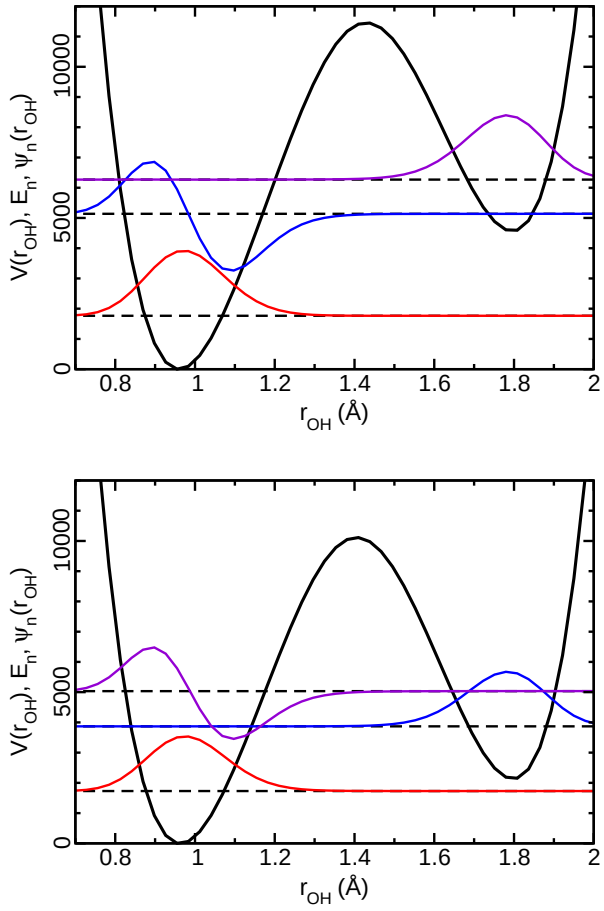


Figure 3.2 The instantaneous proton potentials (solid black line), eigenvalues (dashed black lines), and eigenfunctions are plotted as a function of the $O-H$ distance for two solvent coordinate values for the $PT$ case (energies are in cm$^{-1}$). Top panel: $\Delta E = -13.0$ kcal/mol. Bottom panel: $\Delta E = -6.0$ kcal/mol.

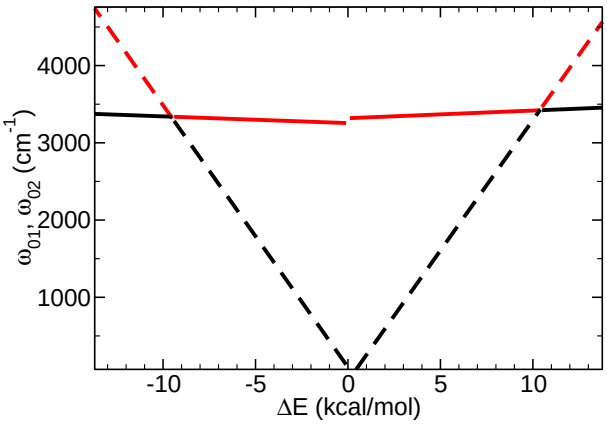


Figure 3.3 A schematic of the $n = 0 \rightarrow n = 1$ (black lines) and $n = 0 \rightarrow n = 2$ (red lines) transition frequencies as a function of solvent coordinate, $\Delta$E. The diabatic surface $D_1$ is represented by solid lines, while the dashed lines illustrate the diabatic surface $D_2$.

In cases where non-adiabatic excited-state dynamics are possible, one has to pay particular attention in calculating the spectra.[172–174] The problem is simplified if the excited-state dynamics are in either the adiabatic or diabatic limit. In this work, the adiabatic limit is one in which, upon absorption to the $n$=1 ($n$=2) state, the excited state remains in the $n$=1 ($n$=2) vibrationally excited state, even as it changes character as the solvent coordinate evolves. In contrast, the diabatic limit is the one in which the excited-state wavefunction maintains its character (localization in product/reactant well), even as the vibrational state changes from $n = 1$ to $n = 2$ as the solvent coordinate evolves at the "crossing points" or dividing surface, located for this system at $\Delta E$= -9.5 and 10.4 kcal/mol.

To determine the extent of diabaticity/adiabaticity for the present system, the rates of transition from one diabatic state to another were estimated using a Landau-Zener surface hopping probability,[175–178]

$$P_{LZ} = 1 - e^{-\frac{2\pi W_{12}^2}{\hbar v_\perp |\Delta F_\perp|}}, \qquad [3.7]$$

where $W_{12}$ is the coupling between diabatic surfaces $D_1$ and $D_2$, $|\Delta F_\perp|$ is the difference in slopes between the two surfaces, and $v_\perp$ is the velocity in the solvent coordinate at the dividing surface. For this system, the intersections of the diabatic surfaces are assumed to be of the form $\Delta E$=constant. This is reasonable based on Figure 3.3: for reactants, $\Delta E$= -9.5 kcal/mol; for products, $\Delta E$=10.4 kcal/mol. The Landau-Zener probabilities were calculated from non-equilibrium molecular dynamics trajectories, where the system was first equilibrated in the ground state, then promoted to the $n = 1$ or $n = 2$ excited state. Values of $P_{LZ}$ for the $n = 1$ state were calculated from one hundred 10 ps trajectories. The $n = 1$ trajectories had few re-crossings, as the system rapidly moved to low values of the solvent coordinate (toward chemical exchange) once the dividing surface was crossed. For the $n = 2$ state, $P_{LZ}$ values were calculated from four 500 ps trajectories in which the dividing surfaces were crossed $\sim$750 times. For trajectories originating in the $n = 1$ or $n = 2$ states, the calculated probabilities to hop between the $D_1$ and $D_2$ surfaces in both products and reactants were never greater than

0.3%. Therefore, this system appears to be strongly in the diabatic limit and all excited-state trajectories are assumed to remain on the same diabatic surface. Thus, the infrared spectra were calculated using only the vibrational transitions from the ground state to the diabatic surface $D_1$ ($n = 0 \rightarrow D_1$). The diabatic surface $D_1$, as seen in Figure 3.3, is the one that has vibrational frequencies in the characteristic ranges of O-H and N-H stretches, $\sim$3250-3400 cm$^{-1}$ and $\sim$3350-3500 cm$^{-1}$, respectively.

In order to calculate the infrared spectrum, the instantaneous transition frequencies for the $n = 1$ and $n = 2$ states, $\omega_{n0}(t)$, and the transition dipole moment, $\underline{\mu}_{n0}(t)$ were calculated and collected at intervals of 5 fs. From this data, the vibrational state ($n = 1$ or $n = 2$) that corresponds to the diabatic state $D_1$ is selected for calculation of the infrared spectrum based on which $n$ vibrationally-excited state has values that fall within the characteristic ranges of the transition dipole moments ($\sim$ 0.2) and instantaneous transition frequencies($\sim$3250-3500 cm$^{-1}$). The infrared spectrum is then obtained as the Fourier transform of a function comprised of the dipole-dipole time correlation function and the fluctuating frequency, according to the following semiclassical approximation from linear response theory:[179–181]

$$I(\Omega) \sim \frac{1}{2\pi} \int_{-\infty}^{\infty} dt \; e^{-i\Omega t} \; \phi(t). \qquad [3.8]$$

The function $\phi(t)$ is given by

$$\phi(t) = \left\langle \underline{\mu}_{d_{10}}(0) \cdot \underline{\mu}_{d_{10}}(t) \; e^{i \int_0^t d\tau \, \delta\omega_{d_{10}}(\tau)} \right\rangle, \qquad [3.9]$$

where $\underline{\mu}_{d_{10}}(t) = \langle D_1(t)|\underline{\hat{\mu}}|0(t)\rangle$ is the transition dipole moment matrix element at time $t$ between the ground vibrational state and state $D_1$ and $\delta\omega_{d_{10}}(t) = \omega_{d_{10}}(t) - \overline{\omega}_{d_{10}}$ is the instantaneous frequency fluctuation.

In the calculation of vibrational spectra, various approximations, such as the Condon approximation, are sometimes used. While the Condon approximation has been shown in some work to reproduce experimental spectral features of HOD in $D_2O$[182] and hydrated HCl and KOH[183] (both exhibit strong hydrogen-bonding), other work has

indicated that non-Condon effects can be significant in strongly hydrogen-bonded systems.[184,185] Thus, for proton transfer reactions, it may be expected that the Condon approximation is insufficient to describe the vibrational lineshapes of such systems. It is therefore interesting to explore the effectiveness of the Condon approximation in the calculation of vibrational spectra of a model proton transfer complex. Approximations to Eq. 3.9 that can be useful in understanding the origin of the spectral features are discussed in Section 3.5.2.

## 3.4 Results

In this Section, simulated infrared spectra, vibrational frequency distributions, and solvent coordinate free energy surfaces are presented for the model phenol-amine system in nanoconfined $CH_3Cl$. To investigate the role of the reactant and product species and the effects of chemical exchange, five values of the gas phase offset have been examined as discussed in Section 3.3.1 and Table 3.2. The cases consist of instances in which there are products exclusively (*P*), products are favored ($PT_P$), the reaction free energy is nearly zero ($PT$), reactants are favored ($PT_R$), and reactants are found exclusively ($R$), respectively. The infrared spectra of the proton transfer complex were calculated according to Eq. 3.8 from data acquired in eight 15 ns trajectories for the $PT_P$, $PT$, and $PT_R$ cases and from data acquired in four 15 ns trajectories for the $P$ and $R$ cases.

### 3.4.1 $PT$ Case

The distribution of instantaneous frequency shifts and the infrared spectrum for the $PT$ case ($\Delta V_0 = 0.7$ eV) are shown in Figure 3.4. In the distribution of instantaneous frequencies, the contributions from the $n = 0 \rightarrow n = 1$ and $n = 0 \rightarrow n = 2$ transitions are also plotted separately. Note that the frequency distribution has two large peaks, one corresponding to the reactants ($O - H \cdots N$) centered at 3339 $cm^{-1}$ and another corresponding to products ($O^- \cdots H - N^+$) at 3427 $cm^{-1}$, as well as long tails on

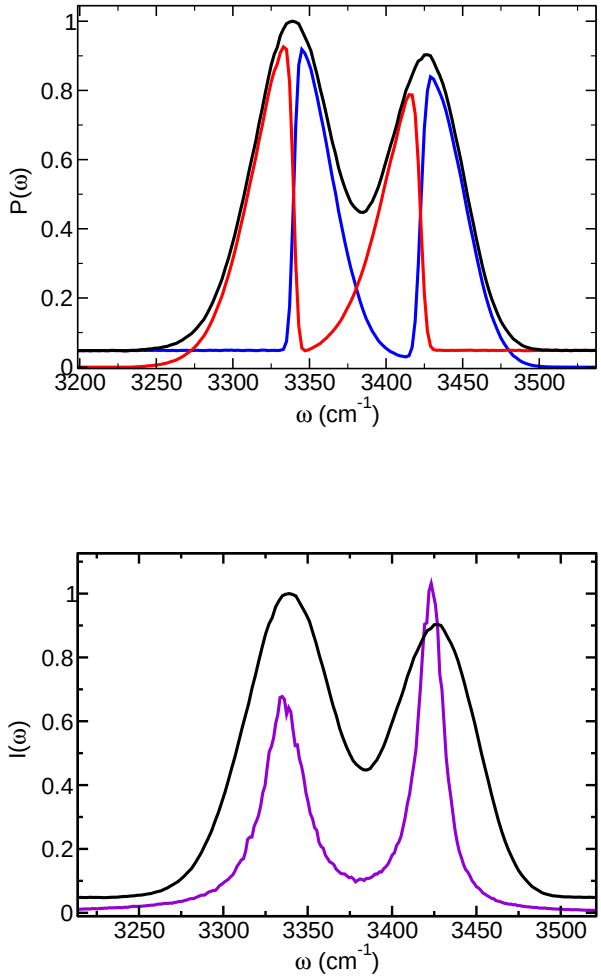


Figure 3.4 Results for the $PT$ ($\Delta V_0 = 0.7$ eV) case. Top: The distribution of instantaneous vibrational transition frequencies for $n = 0 \rightarrow n = 1$ (blue line), $n = 0 \rightarrow n = 2$ (red line), and the total (black line). Bottom: The infrared spectrum (violet line) along with the total instantaneous frequency distribution (black line).

both the low and high frequency sides. The low and high frequency tails correspond to frequencies from the $D_2$ surface. Note that the $D_2$ transition frequency and transition dipole moment values are not included in the calculation of the IR spectrum in this work, as given by Eq. 3.8, nor would they have significant contributions if they were included, due to the negligible values of $\underline{\mu}_{d_{10}}(t)$ . Both the reactant and product peaks of the frequency distribution are Gaussian in shape, and are composed of a sum of contributions from the $n = 0 \rightarrow n = 1$ and $n = 0 \rightarrow n = 2$ frequencies, arising from transitions between the ground state and the diabatic surface $D_1$.

It is interesting to note that the lower frequencies within each Gaussian peak of the product and reactant frequency distributions are from the $n = 0 \rightarrow n = 2$ transition. Specifically, those low frequencies correspond to cases, for example, where the $n = 0$ vibrational state is localized in the reactant well but the $n = 1$ state is primarily in the product well, as illustrated in Figure 3.2. When this occurs, the $n = 2$ state assumes the physical character of a first-excited state localized in the reactants (that of diabatic state $D_1$). Hence, solvent configurations that allow the $n = 1$ state to access the product well lead to quite low $0 \rightarrow 1$ transition frequencies, robbing the lower part of the reactant peak in the distribution of frequencies; however, this is replaced by the contributions from the $n = 2$ state which takes on the same physical character, as discussed previously in Section 3.3.3 and seen in Figure 3.2. Significant contributions to the frequency distribution and the IR spectra are made from $n = 0 \rightarrow n = 2$ transitions when the collective solvent coordinate has low absolute magnitude (as seen in Figure 3.3).

The infrared spectrum, like the instantaneous frequency distribution, has two peaks centered around the O-H and N-H absorption frequencies, at 3336 and 3424 cm$^{-1}$, respectively, while the average frequency including both reactant and product peaks, *i. e.*, of the $0 \rightarrow D_1$ transitions, $\overline{\omega}_{d_{10}}$, is 3377 cm$^{-1}$. The O-H peak has a full-width half maximum (fwhm) of 28 cm$^{-1}$, while the N-H peak has a fwhm of 18 cm$^{-1}$. Clearly,

the spectral peaks are motionally narrowed, as the absorption spectrum exhibits significantly narrower peaks than the instantaneous frequency distribution. This is discussed in further detail in Section 3.5.3.

To understand the origin of the spectral features, it is useful to consider how the equilibrium properties of the system are manifest in the vibrational absorption spectra. To do so, the infrared spectra were fit to an analytical expression. The spectral peaks appear to have a Lorentzian shape; thus, the function $\phi(t)$ from Eq. 3.9 was fit to the general equation

$$\phi(t) = \chi_R e^{-k_R t} e^{i\Delta\omega_R t} + \chi_P e^{-k_P t} e^{i\Delta\omega_P t}. \quad [3.10]$$

The Fourier transform of this function is sum of two Lorentzian distributions. The expression for a Lorentzian distribution is as follows:

$$I(\omega) \propto \frac{1}{\pi} \frac{k}{(\omega - \bar{\omega})^2 + k^2}. \quad [3.11]$$

The frequencies $\Delta\omega_R$ and $\Delta\omega_P$ were found by taking the difference between the average transition frequency , $\overline{\omega}_{d_{10}}$, and the frequency of maximum intensity for the respective reactant and product peaks in the infrared spectrum. The mole fractions, $\chi_R$ and $\chi_P$ were calculated by integrating the reactant and product peaks in the instantaneous frequency distribution. The values fit to $\phi(t)$ using Eq. 3.10 are in excellent agreement with the IR spectrum for the $PT$ case, and indeed give rise to two Lorentzian peaks arising from the contributions of the products and reactants; the Fourier transform of the analytical expression of $\phi(t)$ along with the full spectrum are shown in Figure 3.5.

For the $PT$ case, the fit values for Eq. 3.10 were $\chi_R$=0.54, $\chi_P$=0.46; $k_R$=0.45 ps$^{-1}$=15.0 cm$^{-1}$, $k_P$=0.26 ps$^{-1}$=8.7 cm$^{-1}$; $\Delta\omega_R$=-1.258 ps$^{-1}$=-42 cm$^{-1}$, $\Delta\omega_P$=1.37 ps$^{-1}$=45.7 cm$^{-1}$. The mole fractions $\chi_R$ and $\chi_P$ give rise to an equilibrium constant of 0.85, which agrees within statistical error with the value of $K_{eq}$=0.8, calculated from values of $\Delta$A, given in Table 3.2. It is notable that the difference in transition dipole moment between products and reactants does not factor into the fitting for $\phi(t)$. Although the reactants and products have disparate dipole moments ($\sim$2 and $\sim$9 Debye,

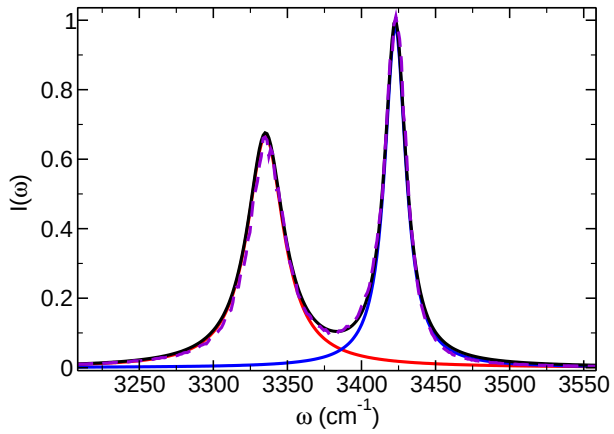


Figure 3.5 The analytical fit parameters for reactants (red line), products (blue line), and the combined analytically fit spectrum (black line). The full $PT$ case infrared spectrum (violet line) is given for comparison.

respectively), the *transition* dipole moments are virtually identical: between 0.2 and 0.21 for both reactants and products. The product peak in the infrared spectrum shown in Figure 3.4 exhibits a higher intensity than the reactant peak, even though the equilibrium constant slightly favors reactants for the $PT$ case. This is due to the smaller value of $k_P$, which gives rise to the narrower peak width in products (as shown in Eq. 3.11). The values of $k_R$ and $k_P$ are related to the dipole-dipole time correlation functions, which will be discussed in Section 3.5.2. The fact that the equilibrium composition of reactants and products is reflected in the infrared spectrum arises from the mapping of the transition frequencies onto the solvent coordinate, as discussed in Section 3.5.1, and the similarities in transition dipole moments of the products and reactants. This suggests that the infrared spectra for this system can be predicted from data acquired from equilibrium simulations and conversely, that the spectra provide direct information about the chemical equilibrium. This may not be the case for systems with fast chemical exchange or different product and reactant transition dipole moments.

### 3.4.2 $PT_P$ and $PT_R$ Cases

To investigate how the reaction equilibrium affects the spectrum, the gas phase offset was decreased and increased slightly from the $PT$ case. For the $PT_P$ case ($\Delta V_0 = 0.65$ eV), the products are favored over reactants by approximately 7:1. On the other hand, in the $PT_R$ case, the reactants are favored over the products by roughly 5:1 ($\Delta V_0 = 0.75$ eV). The distribution of transition frequencies and the IR spectrum for the $PT_P$ case are shown in Figure 3.6; the frequency distribution and spectrum for the $PT_R$ case are shown in Figure 3.7.

For the $PT_P$ case in which products are favored, the distribution of transition frequencies is qualitatively similar to that for the $PT$ case, except that the lower-frequency peak corresponding to reactants is diminished in intensity. This can be seen by comparing Figure 3.6 to Figure 3.4. The peak corresponding to reactants for the $PT_P$ case is located at $\sim 3333$ cm$^{-1}$ and that for products is centered near 3432 cm$^{-1}$, giving an

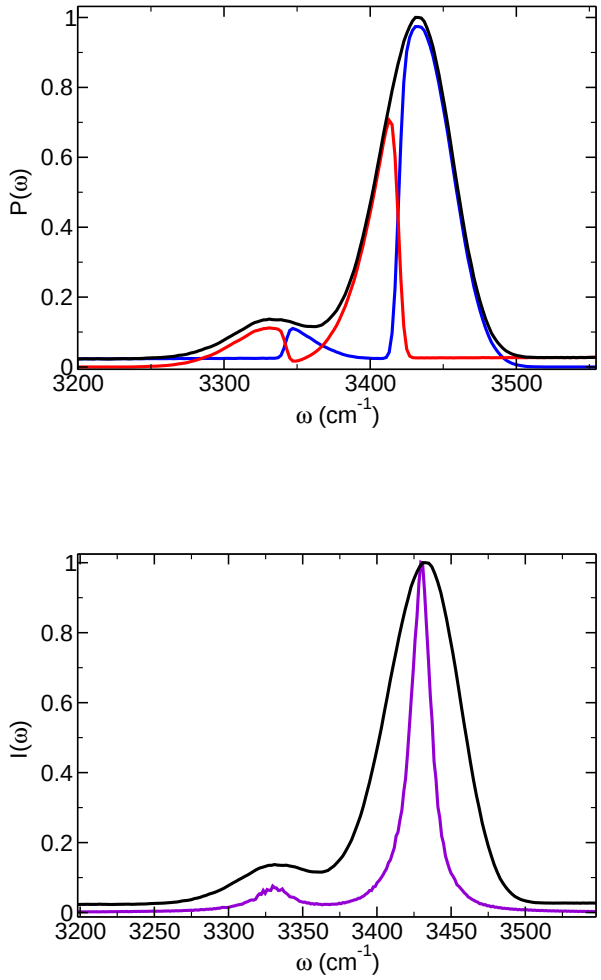


Figure 3.6 Same as Figure 3.4 but for the $PT_P$ ($\Delta V_0 = 0.65$ eV) case.

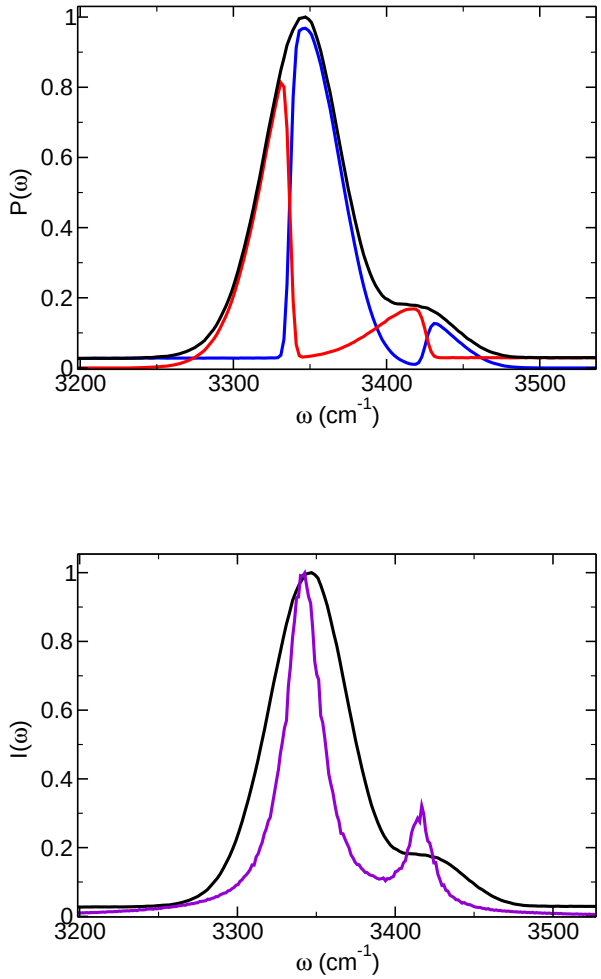


Figure 3.7 Same as Figure 3.4 but for the $PT_R$ ($\Delta V_0 = 0.75$ eV) case.

average transition frequency, $\overline{\omega}_{d_{10}}$, of 3418 cm$^{-1}$. Each peak has a contribution from both the $n = 0 \rightarrow n = 1$ and $n = 0 \rightarrow n = 2$ transitions (on the $D_1$ diabatic surface), with the former comprising a larger part of the product peak and the latter a greater part of the reactant peak. Note that the average frequencies for the product and reactant peaks in the $PT_P$ case differ from those for the $PT$ case. These differences arise from different probability distributions in the solvent coordinate, which are a result of the different gas phase offsets for the five cases. The relationship between transition frequencies and solvent coordinate values, as well as the solvent coordinate probability distributions for the five cases, are discussed further in Section 3.5.1.

As with the $PT$ case, the $PT_P$ spectrum exhibits two Lorentzian-shaped peaks for the reactants and products; both absorption peaks are narrower than the frequency distribution. The fwhm of the reactant peak, centered at 3330 cm$^{-1}$, is 27 cm$^{-1}$. For the product peak, centered at 3430 cm$^{-1}$, the fwhm is 16 cm$^{-1}$. Like the $PT$ case, the spectrum is well fit by two Lorentzian peaks according to Eq. 3.10. The fit results in the following values: $\chi_R$= 0.12, $\chi_P$=0.88; $k_R$=0.51 ps$^{-1}$=17.0 cm$^{-1}$, $k_P$=0.23 ps$^{-1}$=7.7 cm$^{-1}$; $\Delta\omega_R$=-2.64 ps$^{-1}$=-88 cm$^{-1}$, $\Delta\omega_P$=0.36 ps$^{-1}$=12.0 cm$^{-1}$. Note that the coefficients $\chi_R$ and $\chi_P$ give an estimate of the equilibrium constant, based on the spectrum, of $K_{eq} \sim 7.3$. This is in excellent agreement with the value of $K_{eq} \sim 7$ given in Table 3.2, which was calculated using the solvent coordinate values.

The $PT_R$ case has a distribution of transition frequencies, shown in Figure 3.7, that is in many ways the reverse of the $PT_P$ case: both reactant and product peaks are observed, with the reactant peak significantly larger than that for products. The reactant peak is centered near 3347 cm$^{-1}$, while the product peak is around 3420 cm$^{-1}$; the average value for the $n = 0 \rightarrow D_1$ transition, $\Delta\omega_{d_{10}}$, is 3352.5 cm$^{-1}$. The $n = 0 \rightarrow n = 1$ transition accounts for a greater part of the reactant peak while the $n = 0 \rightarrow n = 2$ transition is the larger contributor to the product peak. It was seen that for both the $PT_P$ and $PT_R$ cases, the predominant species (products and reactants, respectively for these cases) has more contributions from the $n = 1$ state, while the minor species

(reactants and products, respectively) has greater contributions from the $n = 2$ state. This is the case because higher absolute values of the solvent coordinate are sampled when the reaction complex is in the predominant species, while lower absolute values of the solvent coordinate arise for the minor species.

As with the $PT$ and $PT_P$ cases, the infrared spectrum for the $PT_R$ case has two motionally-narrowed peaks for reactants and products. The reactant peak is centered at 3341.5 cm$^{-1}$ with a fwhm of 28 cm$^{-1}$, while the product peak has a fwhm of 18 cm$^{-1}$, centered at 3417 cm$^{-1}$. The fitting of the $PT_R$ spectrum using Eq. 3.10 resulted in the following values: $\chi_R$= 0.86, $\chi_P$=0.14 (giving $K_{eq}$ ~0.16); $k_R$=0.425 ps$^{-1}$=14.2 cm$^{-1}$, $k_P$=0.27 ps$^{-1}$=9.0 cm$^{-1}$; $\Delta\omega_R$=-0.337 ps$^{-1}$=-11.2 cm$^{-1}$, $\Delta\omega_P$=1.93 ps$^{-1}$=64.4 cm$^{-1}$. Thus, like the cases discussed previously, the $PT_R$ spectrum is described well as the sum of two Lorentzian peaks.

### 3.4.3 $P$ and $R$ Cases – No Proton Transfer

The $P$ and $R$ cases exhibited no proton transfer over the course of four 15 ns trajectories. Thus, they provide an interesting comparison with the $PT$, $PT_P$, and $PT_R$ cases for which chemical exchange, or an equilibrium between the reactants and products, is observed in the simulations.

The distribution of transition frequencies for the $P$ ($\Delta V_0 = 0.45$ eV) case is shown along with the IR spectrum in Figure 3.8, while the analogous data for the $R$ ($\Delta V_0 = 0.95$ eV) case is presented in Figure 3.9.

The distribution of transition frequencies for the $P$ case consists of a single peak centered around 3455 cm$^{-1}$. The distribution results almost completely from the $n = 0 \rightarrow n = 1$ transition, with a small contribution on the low frequency side from the $n = 0 \rightarrow n = 2$ transition. This is accompanied by a significantly diminished tail on the low frequency side compared to the frequency distributions for the $PT$, $PT_P$, and $PT_R$ cases. The significant contributions from $n = 0 \rightarrow n = 1$ transitions and the negligible amount of low frequencies in the frequency distribution can all be attributed

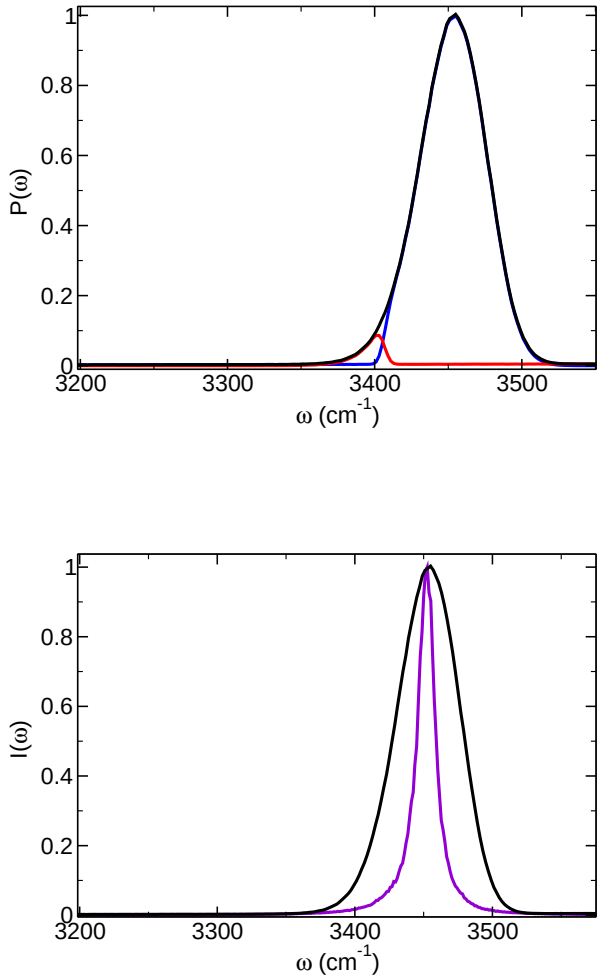


Figure 3.8 Same as Figure 3.4 but for the $P$ ($\Delta V_0 = 0.45$ eV) case.

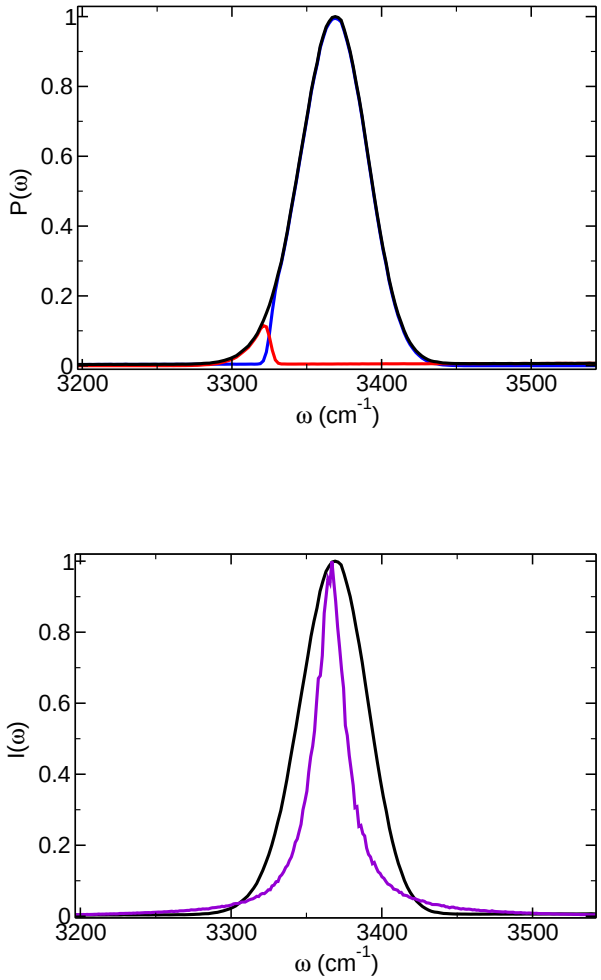


Figure 3.9 Same as Figure 3.4 but for the $R$ ($\Delta V_0 = 0.95$ eV) case.

to the fact that high values of the solvent coordinate are sampled almost exclusively in the $P$ case; lower values of $\Delta E$ give rise to $n = 0 \rightarrow n = 2$ contributions to the $D_1$ surface, and also have low frequencies in the $n = 0 \rightarrow n = 1$ transitions (to the $D_2$ surface), as can be seen in Figure 3.3.

The infrared spectrum for the $P$ case, similar to the frequency distribution, is a single peak centered at 3453 cm$^{-1}$. When compared to the three cases that exhibit proton transfer, the $P$ spectrum is even narrower, with a fwhm of 14 cm$^{-1}$. In contrast, for the distribution of frequencies the fwhm is 53 cm$^{-1}$. This motional narrowing is discussed in greater detail in Section 3.5.3.

The frequency distribution and infrared spectrum for the $R$ case shown in Figure 3.9 are qualitatively the same as for the $P$ case. Specifically, the frequency distribution is a single peak associated almost completely with the $n = 0 \rightarrow n = 1$ transition with a small contribution from the $n = 0 \rightarrow n = 2$ contribution on the low frequency side. The low frequency tail of the distribution is quite small. The primary difference in the distributions for the $P$ and $R$ cases is the shift in frequency: for the $R$ case, the distribution is centered near 3369 cm$^{-1}$. The $R$ case infrared spectrum is also only quantitatively different than that for the $P$ case, consisting of a single peak. Like the frequency distribution, the spectrum is shifted to lower frequencies compared to the $P$ case and is centered at 3366 cm$^{-1}$. In addition, the spectrum is motionally narrowed with a fwhm of 22.5 cm$^{-1}$ compared to the fwhm of 53 cm$^{-1}$ for the frequency distribution (see Section 3.5.3).

### 3.4.4 Comparison of the Cases

It is useful to compare the distributions of transition frequencies and calculated spectra for the five cases considered; these are presented in Figure 3.10. To facilitate comparison, the frequency distributions have been normalized. In the frequency distributions, peaks corresponding to reactants and products are clearly resolved with the reactant (product) peak increasing (decreasing) in magnitude as $\Delta V_0$ is increased. For

the three cases exhibiting proton transfer, $PT$, $PT_P$, and $PT_R$, there is a nearly isosbestic point at $\sim$3388 cm$^{-1}$. The distributions for the $P$ and $R$ cases do not intersect the other curves at this point. This indicates that the anharmonicity of the reactant and product wells are affected by the overall exoergonicity of the reaction. That is, the more endoergonic the reaction is, the higher the reactant vibrational frequencies and the more exoergonic the reaction, the higher the product vibrational frequencies. This also corresponds to higher absolute values of the solvent coordinate that are sampled as exo-/endoergonicity increases, as discussed above in Sections 3.4.2 and 3.4.3 and in further detail in Section 3.5.1. The shift in the reactant and product frequencies leads to non-isosbestic behavior as the reaction equilibrium is shifted. However, it appears that if the changes in exoergonicity are sufficiently small, such as for the $PT$, $PT_P$, and $PT_R$ cases, the reactant and product frequency shifts are relatively minor, nearly preserving an isosbestic point. This issue is discussed further in Section 3.5.1.

The comparison of the infrared spectra for the five cases shown in Figure 3.10 illustrates a nearly isosbestic point at 3394 cm$^{-1}$ for the cases where proton transfer is observed ($PT$, $PT_P$, and $PT_R$), as also seen in the frequency distribution. It is only slightly shifted due to the motional narrowing of the spectra. While the $PT$, $PT_P$, and $PT_R$ have nearly identical fwhm values for the product (fwhm$\sim$18 cm$^{-1}$) and reactant (fwhm$\sim$28 cm$^{-1}$) peaks, the $P$ and $R$ cases exhibit slightly narrower peak widths of fwhm=14 and 22.5 cm$^{-1}$, respectively. The origins of the differences in the fwhm of the $P$ and $R$ cases are discussed in more detail in Section 3.5.3.

## 3.5 Discussion

This Section discusses the analysis carried out to understand the features of the frequency distributions and infrared spectra presented in Section 3.4. In particular, the role of a collective solvent coordinate, the Condon and other approximations to the spectra, motional narrowing, and connections to proton transfer rate constants are considered.

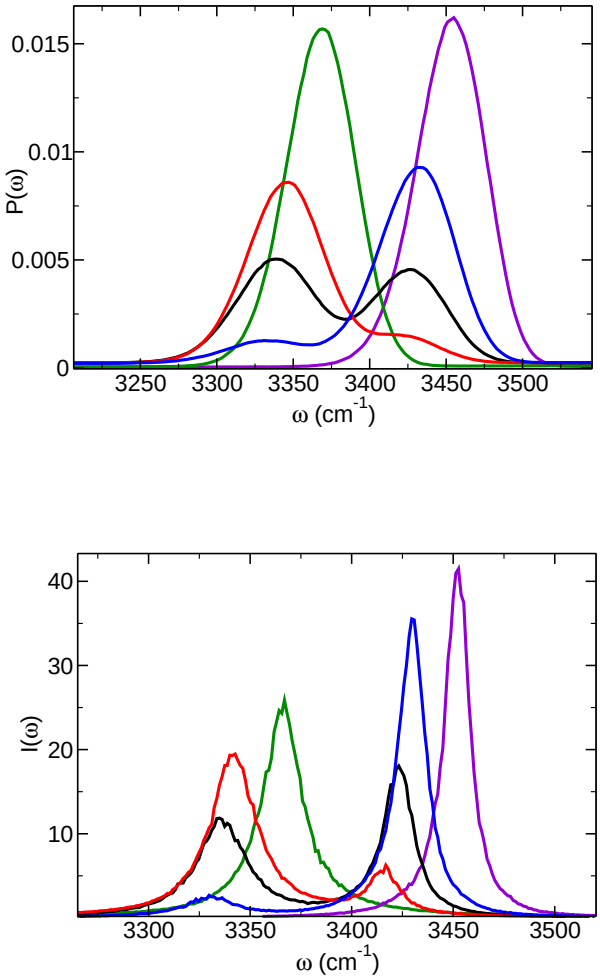


Figure 3.10 Results comparing the five cases, $P$ (violet line), $PT_P$ (blue line), $PT$ (black line), $PT_R$ (red line), and $R$ (green line) are shown. Top: Normalized total transition frequency distributions. Bottom: Infrared spectra.

### 3.5.1 Solvent Coordinate and Frequency Distributions

Since the frequency fluctuations arise through coupling to the solvent, it is instructive to examine the strong relationship between a collective solvent coordinate and the proton vibrational frequency. We define the solvent coordinate as

$$\Delta E(\mathbf{Q}, \mathbf{e}) = V_g(r_P, \mathbf{Q}, \mathbf{e}) - V_g(r_R, \mathbf{Q}, \mathbf{e}), \qquad [3.12]$$

where $r_P$ and $r_R$ are values of the O-H distance characteristic of the reactants ($r_{OH}$=0.95 Å) and products ($r_{OH}$=1.8 Å), respectively. A plot of the instantaneous transition frequencies, $\omega_{10}$ and $\omega_{20}$, versus $\Delta E$ is given in Figure 3.11 for the $PT$ case (data presented in the figure is collected from 6,000 evenly spaced points in one 15 ns trajectory). Note that $\Delta E < 0$ corresponds to reactant configurations while $\Delta E > 0$ implies products. It is clear from this data that there is a remarkably strong correlation between $\omega_{n0}$ and $\Delta E$, indicating that the solvent coordinate can be used to quite accurately predict the frequency distributions. Specifically, the solvent coordinate distributions, plotted in Figure 3.12 for the five cases considered, can be directly mapped using the relationship given in Figure 3.11 to determine the total frequency distributions, the relative contributions of the products and reactants, and the $n = 0 \rightarrow n = 1$ and $n = 0 \rightarrow n = 2$ transitions to the diabatic state $D_1$ (*cf.* Figure 3.3). The dividing surfaces for the diabatic states $D_1$ and $D_2$ are located in the solvent coordinate at ΔE=-9.5 kcal/mol for reactants and at ΔE=10.4 kcal/mol for products.

A strong relationship between frequency distribution and solvent coordinate was found for all of the cases considered. Moreover, the quantitative relationships between the transition frequencies ($\omega_{10}$, $\omega_{20}$) and $\Delta E$ evident in Figure 3.11 are the same for all five cases considered. The differences in the frequency distributions among the five cases arise from variations in the distribution of solvent coordinate values. Thus, by combining data from the solvent coordinate distributions with the multilinear relationships between the solvent coordinate, $\Delta E$, and the diabatic surface potentials $D_1$ and $D_2$ (likewise, the $n = 0 \rightarrow n = 1$ and $n = 0 \rightarrow n = 2$ transitions), the frequency

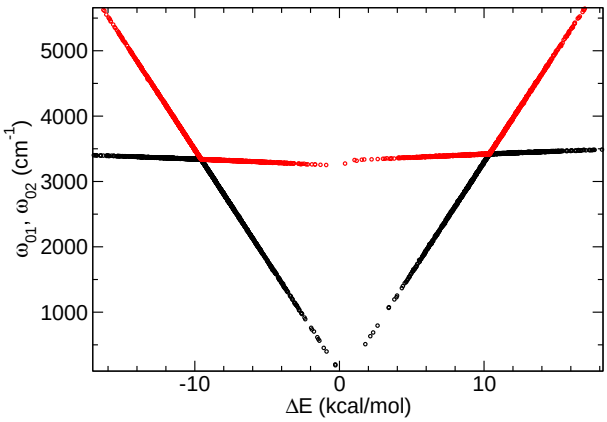


Figure 3.11 A scatter plot of the $n = 0 \rightarrow n = 1$ (black circles) and $n = 0 \rightarrow n = 2$ (red circles) instantaneous transition frequencies versus the collective solvent coordinate (Eq. 3.12) for the $PT$ case.

distributions can be determined. For example, the blueshifting of the reactant and product frequencies in the $R$ and $P$ cases relative to the chemical exchange cases can be understood based on the solvent coordinate distributions in Figure 3.12. Specifically, the distributions for the $R$ and $P$ cases are centered at larger absolute values of $\Delta E$, which correspond to higher vibrational frequencies as seen in Figure 3.11. The free energies for the $PT_P$, $PT$, and $PT_R$ cases are also shown as a function of the solvent coordinate in Figure 3.12. The errors in the free energies were calculated by block averaging, using the student *t*-distribution, and are reported at the 95% confidence level[118] The shifting reactant-product equilibrium with $\Delta V_0$ is clear from this plot. Note that the minima of the reactant and product wells (and hence also the peaks in the solvent coordinate distributions) shift with the reaction exoergonicity. This indicates that the peaks in the frequency distributions associated with reactants and products also shift between the $PT_P$, $PT$, and $PT_R$ cases, though this is somewhat more difficult to see from Figure 3.10.

The correlation between solvent coordinate and frequency distribution suggests that, once the relationship is determined, calculations may be simplified. Rather than calculating the vibrational energy levels at every time step, the solvent coordinate can be calculated instead, and from that, the instantaneous frequencies can be determined.

### 3.5.2 Condon and Other Approximations

Skinner and co-workers have recently demonstrated the failure of the Condon approximation to describe the infrared, Raman, and nonlinear spectra of HOD in $H_2O$ and $D_2O$.[184,185] The Condon approximation assumes that the transition dipole moment is a constant, independent of the environment of the mode of interest. Thus, $\phi(t)$ is approximated as

$$\phi(t) \simeq \phi_C(t) = \left\langle |\underline{\mu}_{d_{10}}|^2 \right\rangle \left\langle \underline{e}(0) \cdot \underline{e}(t)\, e^{i \int_0^t d\tau\, \delta\omega_{d_{10}}(\tau)} \right\rangle, \qquad [3.13]$$

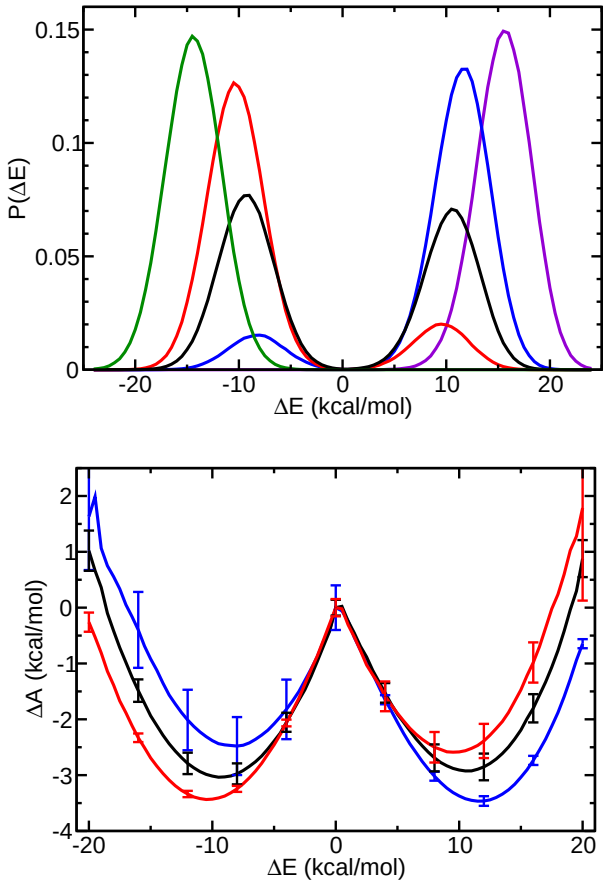


Figure 3.12 Top: The normalized solvent coordinate probability distribution for the $P$ (violet line), $PT_P$ (blue line), $PT$ (black line), $PT_R$ (red line), and $R$ (green line) cases. Bottom: The free energies in the solvent coordinate for the $PT_P$ (blue line), $PT$ (black line), and $PT_R$ (red line) cases.

where $\underline{e}(t)$ is the orientational unit vector at time $t$, as seen above in Eq. 3.4. Clearly, such an assumption is *a priori* suspect for a proton transfer reaction complex (since the infrared spectrum has contributions from two chemical species) and it is interesting to examine it for the system considered here.

Infrared spectra, obtained from the Fourier transform of the Condon approximation expression given in Eq. 3.13 were calculated for all 5 cases and compared with the full expression for the infrared spectra obtained using Eq. 3.9. The results for all five cases are presented in Figs. 3.13 and 3.14. For the $PT$, $PT_P$, $P$, and $R$ cases, the agreement is excellent, as the full and approximated spectra for each case appear essentially identical. It is not surprising that the cases with no chemical exchange ($P$ and $R$) would give the best agreement with the Condon approximation, as there is only one chemical species present. In the $PT_R$ case, the Condon approximation closely matches the infrared spectra obtained using the full expression, except that the intensity of the reactant species is slightly overestimated relative to that of the products. The average transition dipole moment, $\underline{\bar{\mu}}_{d_{10}}$, taken from the $P$ and $R$ cases is 0.207 Debye for products and 0.210 Debye for reactants. Thus, one would predict that the Condon approximation, using an average dipole value in the case of chemical exchange, would, if anything, lead to an overestimate of the product peak intensity and an underestimate of the reactant peak intensity. However, the opposite trend is observed for the $PT_R$ case. In general, though, the similarities in product and reactant transition dipole moments lend themselves toward good approximation with the Condon expression, since the value of $\underline{\bar{\mu}}_{d_{10}}$ is similar to both individual values $\underline{\mu}_{d_{10}}$.

Generally, the Condon approximation gives very good agreement with the full expression for the infrared spectra. It is worth noting that the model phenol-amine proton transfer complex considered here may favor the applicability of the Condon approximation to some degree. For example, the $O \cdots N$ distance is held fixed. This distance, when not held fixed, is affected by changes in the solvent coordinate, *i.e.*, it can be modulated by the electric field exerted on the complex by the solvent molecules,[186] and

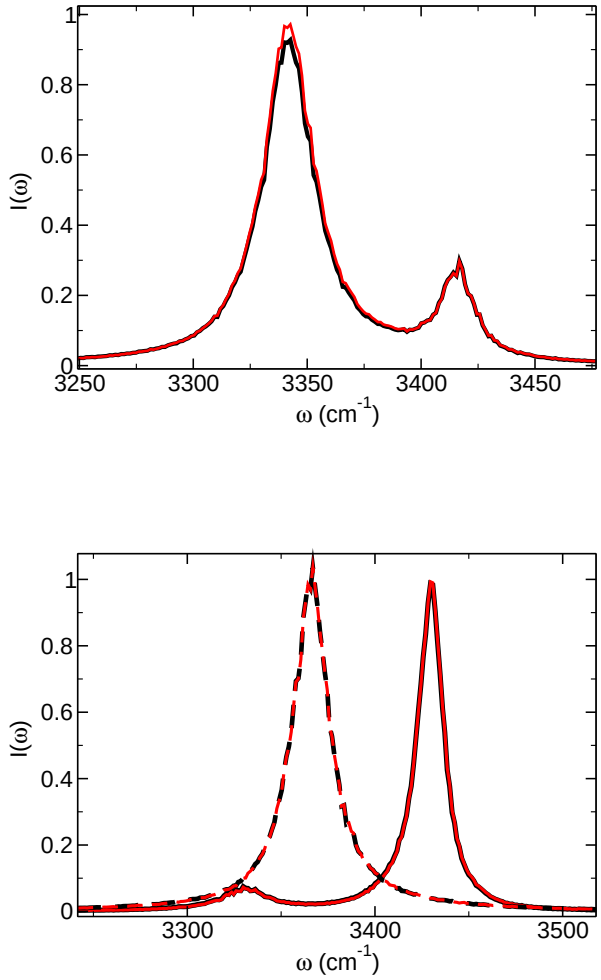


Figure 3.13 Results for the Condon approximation, $\phi_C(t)$, compared with the infrared spectra calculated from the full expression for $\phi(t)$. Top: The full spectrum (black line) and the Condon approximation (red line) for the $PT_R$ case. Bottom: The full spectra (black lines) and Condon approximations (red lines) for the $PT_P$ (solid lines) and $R$ cases (dashed lines).

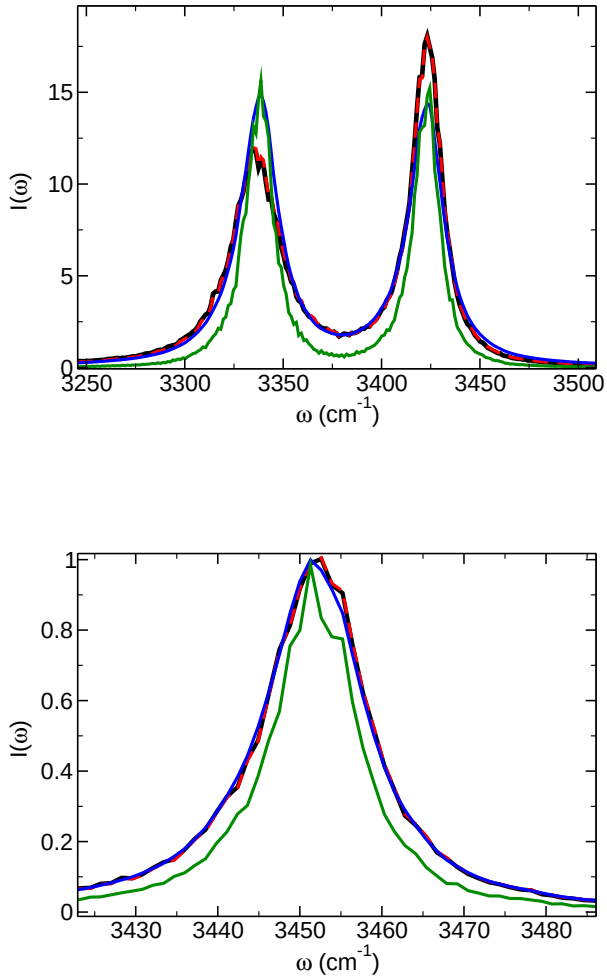


Figure 3.14 The full spectrum (black line), Condon approximation (dashed red line), $\phi_{\bar{\mu}}(t)$ approximation (blue line), and $\phi_{\delta\omega}(t)$ approximation (green line) for the $PT$ and $P$ cases. Top: Spectra for the $PT$ case. Bottom: Spectra for the $P$ case.

thus when unconstrained would be expected to lead to additional non-Condon effects. A similar argument may be made that constraining the $O \cdots H \cdots N$ angle to be linear, as is done here, may reduce the non-Condon effects. Therefore, the deviations from the Condon approximation are likely to be larger for more realistic proton transfer complex models.

In addition to the Condon approximation, several other approximations to the spectra were considered, as discussed in the work of Skinner and Lawrence.[181] If one assumes separability between the dipole-dipole correlation function and the fluctuating frequency, $\phi(t)$ can be approximated as

$$\phi(t) \approx \phi_{\bar{\mu}}(t) = \left\langle \underline{\mu}_{d_{10}}(0) \cdot \underline{\mu}_{d_{10}}(t) \right\rangle \left\langle e^{i \int_0^t d\tau \, \delta\omega_{d_{10}}(\tau)} \right\rangle . \qquad [3.14]$$

Moreover, if one assumes the decay of the dipole autocorrelation function to be sufficiently slow relative to the fluctuations in frequency, $\phi(t)$ can simply be approximated as

$$\phi(t) \approx \phi_{\delta\omega}(t) = \left\langle e^{i \int_0^t d\tau \, \delta\omega_{d_{10}}(\tau)} \right\rangle . \qquad [3.15]$$

The approximations given in Eqs. 3.14 and 3.15 were applied to all fives cases and compared with the infrared spectra calculated from the full expression for $\phi(t)$. For the cases with chemical exchange, $PT$, $PT_P$ and $PT_R$, the spectra from $\phi_{\bar{\mu}}(t)$ (Eq. 3.14) led to enhanced intensity of the reactant peaks relative to the products. Results for spectra obtained from the $\phi_{\bar{\mu}}(t)$ and $\phi_{\delta\omega}(t)$ approximations, compared with the full infrared spectra, are given for the $PT_R$, $PT_P$, and $R$ cases in Figure 3.15.

For the $P$ and $R$ cases with no chemical exchange, the linewidths and intensities of the $\phi_{\bar{\mu}}(t)$ approximation are in good agreement with the full spectra. However, for all of the cases considered, spectra obtained with thethe $\phi_{\delta\omega}(t)$ approximation deviate from the infrared spectra estimated using the full expression for $\phi(t)$. Specifically, the linewidths are narrower, while the maximum of the reactant peak is enhanced relative to the product peak. Although none of the five cases gave good agreement with the $\phi_{\delta\omega}(t)$ approximation, better agreement is found for the $PT_P$ and $P$ cases. This, along with

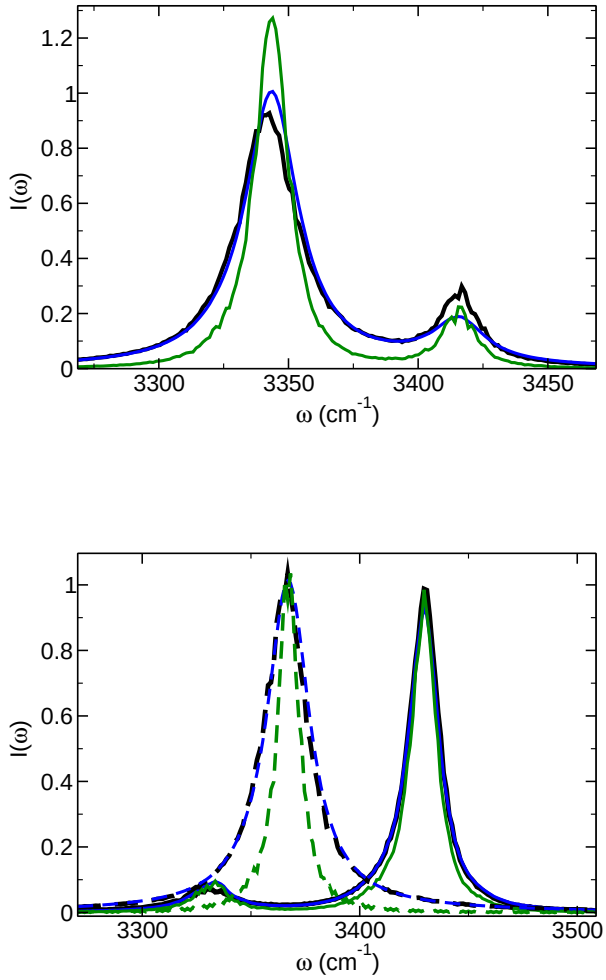


Figure 3.15 Results for the approximations $\phi_{\bar{\mu}}(t)$ and $\phi_{\delta\omega}(t)$, compared with the infrared spectra calculated from the full expression for $\phi(t)$. Top: The full spectrum (black line), $\phi_{\bar{\mu}}(t)$ approximation (blue line), and $\phi_{\delta\omega}(t)$ approximation (green line), for the $PT_R$ case. Bottom: The full spectra (black lines), $\phi_{\bar{\mu}}(t)$ approximations (blue lines), and $\phi_{\delta\omega}(t)$ approximations (green lines), for the $PT_P$ (solid lines) and $R$ (dashed lines) cases.

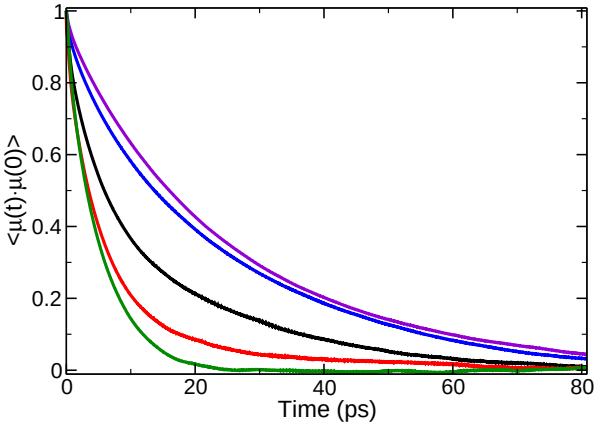


Figure 3.16 The transition dipole time correlation functions, $\left\langle \underline{\mu}(0) \cdot \underline{\mu}(t) \right\rangle$, for the $P$ (violet line), $PT_P$ (blue line), $PT$ (black line), $PT_R$ (red line), and $R$ (green line) cases.

the extent of agreement of the $\phi_{\bar{\mu}}(t)$ approximation, can be understood by examining the dipole-dipole time correlation functions.

The normalized dipole autocorrelation functions for the five cases considered are given in Figure 3.16. It should be mentioned the the dipole and rotational, $\langle e(t) \cdot e(0) \rangle$, autocorrelation functions are essentially identical to each other for all of the cases. This indicates that the dipole-dipole time correlation functions (TCFs) are dominated by reorientation, rather than fluctuations in the transition dipole moment values. As can be seen in Figure 3.16, the reactants only $R$ case has the fastest reorientation time, while the products only $P$ case has the slowest reorientation time. The reorientation times are affected by differences in the charge distributions, but the differences in reorientation times may be partially attributed to the different probability distributions of the products and reactants. As mentioned previously, earlier Monte Carlo studies of the system[62] showed that the more polar products are more likely located in the interior of the cavity, while the reactants are distributed near the walls of the nanocavity. Thus, the differences in product and reactant reorientation times may be augmented by confinement effects.

The dipole-dipole time correlation functions of the $P$ and $R$ cases can be fit with a single exponential function. The $PT_P$, $PT$, and $PT_R$ cases with chemical exchange have intermediate values for the decay of the dipole autocorrelation functions, and are, in fact, linear combinations of the $R$ and $P$ dipole-dipole time correlation functions. The dipole/rotational autocorrelation functions of the cases with chemical exchange can be predicted with good agreement from the known dipole-dipole TCFs of the $P$ and $R$ cases and the respective mole fractions of products and reactants in the $PT$, $PT_P$, and $PT_R$ cases. This is a reflection of the "slow" chemical exchange, which generally takes place on a timescale that is slower than the reorientation times.

The reorientation times of the five cases can be used to understand the extent of agreement of the $\phi_{\delta\omega}(t)$ approximation, which neglects contributions from the dipole-dipole TCF. One can see by comparing the full expression for the infrared spectrum (Eq. 3.9) with the expression for $\phi_{\delta\omega}(t)$ (Eq. 3.15) and the resulting spectra from the two expressions, that it is the rapid reorientational times of the reactants that leads to line broadening, and thus poorer agreement of the approximation for the $R$, $PT_R$, and $PT$ cases. As the reorientation times slow (for cases with a higher reaction composition of products), the contributions to the spectra from the dipole-dipole TCF are diminished and the approximation of $\phi_{\delta\omega}(t)$ is in better agreement with the full spectra of the $PT_P$ and $P$ cases. The broadening of linewidths from fast reorientation also leads to a reduced intensity for reactants in the full infrared spectra, as the $k_R$ values are larger than the $k_P$ values in the analytical fits according to Eq. 3.10; for Lorentzian (Cauchy) distributions, larger $k$ values lead to broader, shorter peaks (as shown in Eq. 3.11). The degree to which the approximation $\phi_{\bar{\mu}}(t)$ agrees with the infrared spectra can be explained in a similar fashion. Since $\phi_{\bar{\mu}}(t)$ averages the dipole-dipole TCF for both products and reactants, any contributions to the spectral features due to differences in reorientation times for the two species are lost. For products, the lifetime, $\tau$, describing exponential decay, $e^{-t/\tau}$, is $\sim$5 times longer than that for reactants. Because of the

Table 3.4 Motional Narrowing Parameters for the $P$ and $R$ Cases.

| Case | $\tau_c$ (ps) | $\Delta$ (ps$^{-1}$) | $\alpha$ |
|---|---|---|---|
| $P$ | 0.77 | 0.69 | 0.53 |
| $R$ | 0.52 | 0.67 | 0.35 |

significant difference in reorientation times of the product and reactant species, the approximation $\phi_{\bar{\mu}}(t)$ is poorest for the cases featuring chemical exchange.

### 3.5.3 Linewidths and Motional Narrowing

For all of the cases considered, the linewidths observed in the spectra, shown in Figs. 3.4-3.9, are narrower than their respective frequency distributions. This indicates that the spectra are in the motional narrowing regime.[179] Motional narrowing results when the parameter $\alpha$ is less than one, where $\alpha = \Delta \cdot \tau_c$ and the correlation time, $\tau_c$, is defined as[179]

$$\tau_c = \frac{1}{\langle \delta\omega^2 \rangle} \int_0^\infty \langle \delta\omega(0)\delta\omega(t) \rangle \, dt. \qquad [3.16]$$

The quantity $\Delta$ is the root mean square deviation of the frequency modulation, $\Delta = \sqrt{\langle \delta\omega^2 \rangle}$. The motional narrowing parameter $\alpha$ was examined for the $P$ and $R$ cases, and the values of the motional narrowing parameters $\tau_c$, $\Delta$, and $\alpha$ are given in Table 3.4. From the values calculated, it is clear that $\alpha < 1$ for both the $P$ and $R$ cases, indicating a motionally-narrowed spectrum. It can be seen that the two cases have similar values of $\Delta$, which is expected based on the similar fwhm observed for the frequency distributions shown in Figs. 3.8 and 3.9. Thus, it is the dynamical properties reflected in $\tau_c$ and the dipole autocorrelation functions that govern the differences in peakwidths of the $P$ and $R$ cases. The value of $\tau_c$ is smaller for the $R$ case than the $P$ case, giving the $R$ case a lower value of $\alpha$, indicating more significant motional narrowing due to frequency fluctuations. However, as evident from the underestimation of the spectral linewidths using the $\phi_{\delta\omega}(t)$ approximation (Eq. 3.15, *cf.* Section 3.5.2),

some broadening of the spectral peaks arises from rapid reorientation, most notably in the reactant peaks. Hence, the deciding factor that gives rise to a broader fwhm in the reactant peaks relative to the product peaks is not the motional narrowing parameters, but the line broadening from the more rapid reorientation time of the reactants (see Figure 3.16). Clearly, the reorientation times are not factored into the expression for motional narrowing as described by the $\alpha$ parameter.

In the $PT$, $PT_P$, and $PT_R$ cases, the distributions of frequencies for the product and reactant peaks are somewhat broader than for the cases with no chemical exchange, indicating larger values of $\Delta$. This is a reflection of the differences in the solvent coordinate free energy curves for these cases, as discussed in Section 3.5.1. Even so, the spectra of the $PT$, $PT_P$, and $PT_R$ cases are clearly motionally narrowed - the spectral peaks are significantly narrower than the frequency distributions. The higher fwhm values of the absorption peaks for the chemical exchange cases, relative to the $P$ and $R$ cases, can be attributed to these larger values of $\Delta$.

### 3.5.4 Proton Transfer Rate Constants

It is interesting to consider what information the infrared spectra provide about the proton transfer reaction rate constants. Such information is not easily extracted from the linear IR absorption spectra presented here, *e.g.*, through analysis of the lineshapes. However, nonlinear IR spectroscopies can probe more dynamical quantities, such as the frequency autocorrelation function, more directly. Therefore, the relationship between the frequency-frequency time correlation function and proton transfer rate constants is discussed here.

The frequency autocorrelation functions of the $PT$, $PT_R$ and $PT_P$ cases, shown in Figure 3.17, have a long time decay tail, while those of the $P$ and $R$ cases do not, with nearly complete decay by 5 ps. This suggests that chemical exchange gives rise to the long-time tail. To examine reaction rate constants in the context of equilibrium dynamics, the autocorrelation functions of the fluctuation of the reaction composition,

$\delta n(t) = n_r(t) - \langle n_r \rangle$, were calculated.[187] Here, $n_r$ is a variable describing whether the reaction complex is in the reactant form and is defined as

$$n_r(t) = \begin{cases} 1, & \Delta E(t) < 0 \\ 0, & \Delta E(t) > 0. \end{cases} \quad [3.17]$$

Then, $\langle n_r \rangle$ is the fraction of reactants present at equilibrium. Note that the analogous variable related to products, $n_p(t)$, could also be used; since $n_r(t) = 1 - n_p(t)$, the same result is obtained. The reaction composition autocorrelation functions for all of the cases involving chemical exchange are given in Figure 3.17.

As expected,[187] the functions fit the form $e^{-t/\tau}$, where $\tau$ is the lifetime and a function of the forward and backward rate constants, $k_f$ and $k_b$, such that $\tau = (k_f + k_b)^{-1}$. As can be seen, the lifetime is longest for the $PT$ case, $\tau_{PT} = 388$ ps, which has forward and backward rate constants that are approximately equal, since $K_{eq} \approx 1$. The lifetimes of the $PT_R$ and $PT_P$ cases, $\tau_{PT_R} = 220$ ps and $\tau_{PT_P} = 204$ ps, are dominated by the relatively fast values of $k_b$ and $k_f$, respectively, which correspond to chemical exchange out of the energetically disfavored species (products for $PT_R$, reactants for $PT_P$). The error bars for the $\tau$ values are within 10-15%.

The long-time tail of the frequency autocorrelation functions, $C_{\delta\omega}(t)$, of the $PT$, $PT_P$, and $PT_R$ cases, like the reaction composition autocorrelation functions, fit the form $e^{-t/\tau}$. The following values were obtained for $\tau$ from $C_{\delta\omega}(t)$: $\tau_{PT} = 357$ ps, $\tau_{PT_R} = 217$ ps, and $\tau_{PT_P} = 207$ ps. The lifetimes obtained for $C_{\delta\omega}(t)$ follow the same trend as those for $C_n(t)$, and are the same within statistical error. This suggests that the long-time decay of $C_{\delta\omega}(t)$ is related to the rate of proton transfer.

The relationship between the frequency autocorrelation function and reaction rates can be seen directly for the simpler case where the product and reactant forms of the reaction complex each have a single distinct frequency, $\omega_p$ and $\omega_r$ respectively. In this case, the instantaneous frequency is given by

$$\omega(t) = \omega_r \, n_r(t) \; + \; \omega_p \, n_p(t) = (\omega_r - \omega_p) \, n_r(t) + \omega_p, \quad [3.18]$$

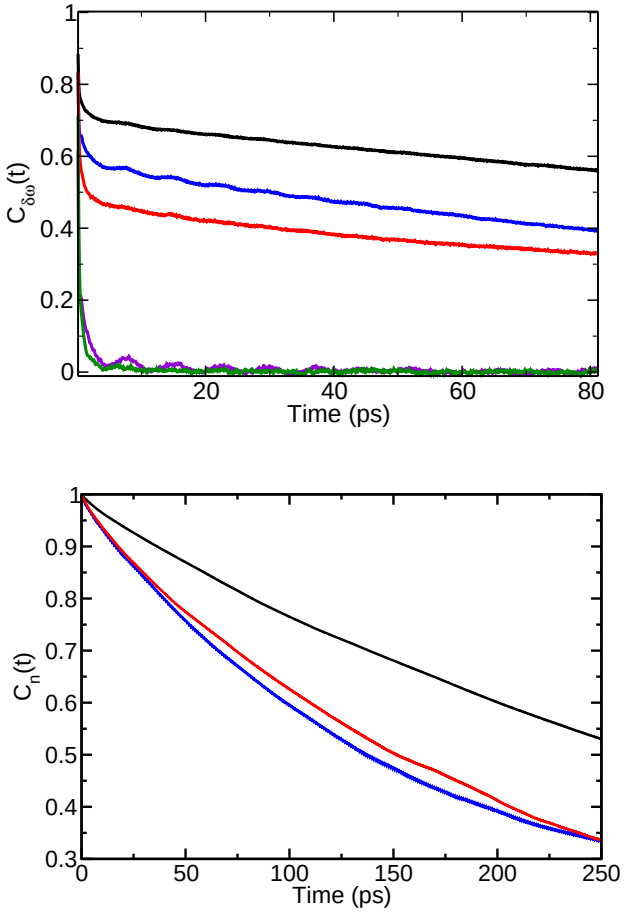


Figure 3.17 Top: The frequency-frequency time correlation function, $C_{\delta\omega}(t)$= $\langle\delta\omega(0)\delta\omega(t)\rangle$, for the $PT$ (black line), $PT_P$ (blue line), $PT_R$ (red line), $P$ (violet line), and $R$ (green line) cases. Bottom: Time correlation functions of the reaction composition $\delta n$, $C_n(t)$= $\langle\delta n(0)\delta n(t)\rangle$, for the $PT$ (black line), $PT_P$ (blue line), and $PT_R$ (red line) cases.

since $n_p(t) = 1 - n_r(t)$. The average frequency at equilibrium is given by an analogous expression, $\langle\omega\rangle = (\omega_r - \omega_p)\langle n_r\rangle + \omega_p$, so that the instantaneous frequency fluctuation is

$$\delta\omega(t) = \omega(t) - \langle\omega\rangle = \delta n(t)\,(\omega_r - \omega_p). \qquad [3.19]$$

Here, $\delta n(t) = n_r(t) - \langle n_r\rangle$ as above. Then, it is clear that the frequency and reaction composition correlation functions are directly related as

$$\begin{aligned} C_{\delta\omega}(t) &= \frac{\langle\delta\omega(0)\delta\omega(t)\rangle}{\langle\delta\omega(0)^2\rangle} \\ &= \frac{\langle\delta n(0)\delta n(t)\rangle\,(\omega_r - \omega_p)^2}{\langle\delta n(0)^2\rangle(\omega_r - \omega_p)^2}, \\ &= C_n(t). \end{aligned} \qquad [3.20]$$

Thus, in this simplified model, the frequency autocorrelation function provides direct information about the reaction rate constants, since

$$C_{\delta\omega}(t) = C_n(t) \propto e^{-t/\tau}, \qquad [3.21]$$

with $\tau = (k_f + k_b)^{-1}$. Clearly, this result for $C_{\delta\omega}(t)$ provides insight into the connection with reaction rate constant information, but strictly applies only when the simplifying assumptions are valid. The system in this work consists of a distribution of frequencies for products and reactants, a small portion of which consists of overlapping frequencies. However, the relationship between $C_{\delta\omega}(t)$ and $C_n(t)$ in Eq. 3.20 and the agreement between the two correlation functions calculated in this work and presented in Figure 3.17 suggest that the two are related for more complex systems. Because frequency autocorrelation functions can be extracted from the results of IR photon echo experiments,[188–194] this indicates the potential for obtaining rate constants for *ground-state* proton transfer reactions from such spectroscopic measurements.

## 3.6 Conclusion

The infrared spectra for a model proton transfer complex dissolved in $CH_3Cl$ solvent in a 12 Å spherical hydrophobic cavity have been calculated with mixed quantum-classical molecular dynamics simulations. The gas phase energy offset was adjusted so that cases with varying degrees of proton transfer (chemical exchange) were explored. The primary conclusions of this work are: 1.) In addition to the $n = 0 \rightarrow n = 1$ vibrational transitions, the $n = 0 \rightarrow n = 2$ vibrational transitions contribute to the infrared absorption spectra, as the two sets of vibrational transitions combine to form diabatic surfaces, labeled $D_1$ and $D_2$. The diabatic surface $D_1$ carries the oscillator strength; thus, transitions from the ground state to $D_1$ give rise to the infrared absorption spectra. 2.) There is a strong relationship between a collective solvent coordinate and the instantaneous vibrational transition frequency, such that the frequency distribution is determined by the sampling of different values of the solvent coordinate. 3.) The spectral linewidths are narrower than the instantaneous frequency distributions, indicating that the absorption spectra are motionally narrowed by the rapid frequency fluctuations of large magnitude. Narrowing of the absorption peaks also has contributions from the decay of the transition dipole autocorrelation functions. 4.) The infrared spectra can be obtained from equilibrium simulations, with the frequency distribution determined from the solvent coordinate. The dipole-dipole time correlation function can be predicted as a linear combination of the product and reactant TCFs based on the relative ratios of products and reactants. 5.) The Condon approximation, which assumes that the transition dipole moment is constant, generally gives very good agreement with the infrared spectra. Other approximations to the function $\phi(t)$ have varying degrees of agreement with the calculated spectra, with the discrepancies in intensity and linewidth generally attributable to different reorientation times for products and reactants. 6.) The frequency autocorrelation function displays a long-time decay tail that appears to contain information about the ground-state proton transfer reaction rate constants.

A simplified proton transfer model of a phenol-amine complex was used in this work, in which the $O - N$ distance is held fixed, and the $O \cdots H \cdots N$ angle is constrained to be linear. While the results indicate that vibrational spectroscopies should provide useful probes of ground-state proton transfer reaction systems in nanoconfined solvents, additional work is required to understand the effect of a realistic treatment of the hydrogen bond distance and angle as well as the impact of more realistic confining framework interactions.

# Chapter 4

# *Ab Initio* Studies of a Carbon Acid for Potential Use as a Friedel-Crafts Acylation Solid Acid Catalyst

In the previous chapters, effects of confinement on chemical behavior were studied directly. The results provide information about how a confining framework affects chemical dynamics and reactivity, in order to elucidate design principles for functional materials. In the work described in this chapter, a novel catalytic system is modeled in order to understand the catalytic mechanism and selectivity. Although these studies are predominantly on homogeneous catalysis, the catalyst has the potential of being incorporated into a variety of porous materials for use as a solid acid. With the results described herein, one may be able to interpret future experimental observations derived from heterogeneous systems. Thus, the approach in this chapter provides a different means for understanding and designing functional materials.

## 4.1 Introduction

In this work, *ab initio* studies of a carbon acid catalyst and its role in the Friedel-Crafts acylation of 2-methoxynaphthalene (2-MN) were carried out in collaboration with the research group of Professor Mikhail V. Barybin. Most of the experimental work focused on the acid as a homogeneous catalyst. The acid is notable in that the acidic proton is bound to a carbon atom. The acidity of the carbon atom is derived from the presence of strongly electron-withdrawing groups: two triflate groups and a fluorinated phenyl ring. The structure of the acid, pentafluorophenylbis(triflyl)methane (hereafter referred to as **Acid1**), is given in Figure 4.1.

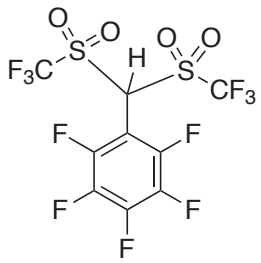

Figure 4.1 Chemical structure of **Acid1**

.

The phenyl ring substituent can be modified in order to incorporate the acid into a material for heterogeneous catalysis. For instance, the synthesis of polystyrene-bound tetrafluorophenylbis(triflyl)methane has been reported,[24] in which **Acid1** was modified by addition of a styryl group at the *para* position. The resulting acid (**styryl-Acid1**) was incorporated into an organic-solvent-swellable polystyrene bead for use as a solid acid. Other chemical modifications attempted have included the addition of alkylsilanol groups for inclusion of the acid into a sol-gel (silica) matrix. Figure 4.2 illustrates these two chemical modifications to **Acid1** that can adapt it for applications in heterogeneous catalysis. Heterogeneous solid acid catalysts are a focus of green chemistry efforts.

## 4.2 Solid Acids in Green Chemistry

The work described in this chapter was done in conjunction with the Center for Environmentally Beneficial Catalysis, a National Science Foundation Engineering Research Center at the University of Kansas. The strong Brønsted acid (**Acid1**) was investigated for its use both as a homogeneous catalyst and as a solid acid catalyst. Solid acids are heterogeneous catalytic materials that are sought after for green chemistry applications. Green chemistry has a number of guiding principles.[195] Some of these include: the prevention of chemical waste, rather than a focus on cleanup of chemical waste after it is generated; promoting atom economy/efficiency, in part by reducing/eliminating solvents, separating agents, and protecting groups; reducing the

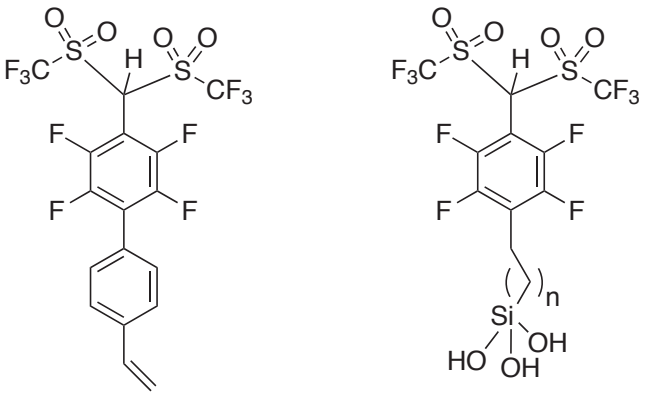


Figure 4.2 Chemical modifications of **Acid1** for incorporation into solid materials for heterogeneous catalysis. Left: **styryl-Acid1**.

toxicity of products and byproducts; the use of renewable feedstocks; seeking reactions that take place at ambient temperature and pressure in order to reduce energy use; and choosing substances that minimize the potential for chemical accidents. Many of these green chemistry principles are addressed in the development and use of solid acids. Solid acids can be used to replace corrosive and toxic Lewis and Brønsted acids, such as $AlCl_3$ and HF, currently used in large-scale chemical syntheses, thereby increasing the safety of manufacture and generating less waste. In addition to replacing undesirable conventional acid reagents, solid acids have the benefits of being reusable, non-corrosive, highly selective, easily separable from reaction mixtures, and generating fewer hazardous byproducts.[196,197] For instance, in conventional acidic (and alkali) systems, large amounts of waste are generated by use of a water quench for neutralization, whereas for solid acid systems, the acid can be readily removed by filtration/separation of phases.

There are a number of different materials currently being researched and used as solid acids.

*Zeolites*

Zeolites are microcrystalline, microporous (pores $<$2 nm in diameter) solids of the form $x\mathrm{M}_2/n\mathrm{O}{\cdot}x\mathrm{Al}_2\mathrm{O}_3{\cdot}y\mathrm{SiO}_2{\cdot}w\mathrm{H}_2\mathrm{O}$, where $x$, $y$, and $w$ are stoichiometric coefficients, and M is a group IA or IIA metal cation.[198] Zeolites, prized for the high internal surface area of their pores, are used as size and shape-selective catalysts, and can be either naturally-occurring minerals or synthetic aluminosilicate materials.[197,199] Due to their microporosity, the utility of zeolites suffers from deactivation due to clogging of pores and size limitations for catalytic transformations of larger organic molecules. However, zeolites are generally highly thermally stable and can be regenerated through heating. They are broadly used in petroleum refining. An example of shape-selective catalysis in zeolites is the isomerization of xylene: only *para*-xylene can diffuse rapidly through the pores of zeolite HZSM5, such that mixtures of xylenes reacted in the zeolite afford complete conversion to *p*-xylene.[197] The ratio of $SiO_2$:$Al_2O_3$ and the Brønsted acidity,

in addition to the pore structure, affects catalytic activity, but zeolites have been found to promote Friedel-Crafts acylation reactions by the ability to form a complex between the zeolite and an acylium-ion-like cation.[196]

*Zeotypes/molecular sieves/mesoporous solids*

Zeotypes describe materials that are not aluminosilicates, but have porous structures similar to zeolites. Often, such materials are mesoporous (having pores 2-50 nm in diameter) and have larger pores than zeolites, increasing their utility in the synthesis of larger pharmaceutical and specialty chemicals. Examples of mesoporous solids include MCMs (developed at Mobil: Mobil composition of matter) and hexagonal mesoporous silicas (HMS), also called micelle-templated silicas (MTS). Both MCM and HMS materials are synthesized based on a micelle template, so that the pore size can be varied.[197,200,201] MCMs are mesoporous aluminosilicates that act as mild acids. Porous silica and MCM materials have been used as scaffolds for the addition of Brønsted acid groups, typically sulfonic acids. This allows for easy recovery and handling of the acids, with less risk to human tissue. For example, sulfonic acid-treated mesoporous silica gel showed good activity and selectivity for esterification of glycerol.[202] Lewis acids can also be incorporated into mesoporous materials; silica-supported $AlCl_3$ was shown to be successful in catalyzing alkene polymerization and benzene alkylation.[200] In fact, silica-supported $AlCl_3$ showed the same activity with enhanced selectivity over homogeneous $AlCl_3$ toward the monoalkylation of benzene.[203] A promising prospect in the development of novel mesoporous HMS-supported solid acid catalysts is that more than one group can be incorporated, such that both catalytically active sites and groups to modify the polarity or affinity of the pores can be added.

*Resin/polymer-supported acids*

Sulfonic acid groups can be added to a variety of substrates, including carbon, cross-linked styrene polymers, and commercial resins, such as Dowex 50 and Amberlite resins to afford solid Brønsted acids.[204] These materials can also be treated with $AlCl_3$ to incorporated Lewis acids. A drawback of polymer-supported acids, however,

is that they easily suffer thermal and chemical damage.[200] On such material, DuPont's Nafion, is inert and chemically robust; Nafion is a copolymer of perfluorinated epoxide and vinylsulfonic acid, and is an effective heterogeneous catalyst for acylation with aroyl chlorides and anhydrides.[204] In an effort to create a solid acid with higher surface area, nanoparticles of Nafion have been entrapped in silica. One example of this, the DuPont product SAC 13, was used to acylate anisole and other aromatic compounds; the silica-supported Nafion catalyst produced higher yields and selectivity than either the reactions with unsupported Nafion or with $AlCl_3$.[205]

*Clays*

Clays consist of negatively-charged crystalline aluminosilicate layers. They contain "defects" in the aluminosilicate structure, with $Al^{3+}$ and $Mg^{2+}$ substitutions for $Si^{4+}$ and $Al^{3+}$, respectively, and $Na^+$, $K^+$, and $Ca^{2+}$ cations situated in a hydrated environment between the layers. Clays can be treated for cation exchange or modified with Lewis or Brønsted acids. They have been shown to be effective catalysts for direct acylation reactions, including reactions with carboxylic acids serving as mild acylating reagents.[196] Clays have also been used for the microwave oxidation of isopropanol to acetone, in lieu of less environmentally-benign reagents such as $CrO_3$ and $KMnO_4$.[195]

*Metal oxides and sulfated metal oxides*

Sulfated zirconia is a highly acidic, mesoporous material that is thermally stable. It has been used as a solid acid to prepare linear alkyl benzenes for use in detergents.[200] Greener syntheses of these surfactants, including the use of sulfated zirconia and HMS-supported $AlCl_3$, offer substantial environmental benefits over mass-production with hydrofluoric acid or aluminum chloride.[197] Other metal oxides that have been explored for their use as solid acids include sulfated titania-alumina, zirconia-alumina, and iron oxide-alumina.[196] In addition to sulfation treatment to increase Brønsted acidity, metal oxides have been treated with Lewis acids, such as $SbF_5$ and $AlCl_3$ to afford solid Lewis acid catalysts. For example, complexes of $SbF_5$-treated titania and mixed titania-oxides serve as solid superacid catalysts for the skeletal isomerization of alkanes.[204]

*Heteropoly acids*

Heteropoly acids (HPAs) are highly acidic metal complexes with two different types of oxoanions,[198,206] and can be used for both homogeneous and heterogeneous catalysis, depending on the solvent polarity and temperature at which reactions are run. In the latter case, supported HPAs (on mesoporous silica or metal oxides) have increased surface area and efficacy as heterogeneous catalysts.[206] Heteropoly acids and acid-treated metal oxides are effective catalysts for Friedel-Crafts acylations, as they stabilitze cationic intermediates such as benzoyl cations.[196]

In summary, solid acids are capable of catalyzing a broad range of chemical transformations, including esterification, isomerizations, alkylation and dealkylation of aromatics and olefins, dehydration of alcohols, and halogenation reactions. In order to design new solid acids, an understanding of the effects of the confining frameworks on catalytic selectivity should be developed. A number of the solid acids mentioned in this section have been effective as catalysts for Friedel-Crafts acylation. In the following section, Section 4.3, solid acids that have been used in the acylation of 2-methoxynaphthalene are detailed, as this reaction is the focus of this chapter. As explained below, solid acids have shown some promise in the regioselective acylation of 2-methoxynaphthalene. However, the reactions generally are run with an excess of 2-MN, so that the yields are reported with respect to the acylating agent. With this in mind, none of the solid acid catalysts used in the acylation of 2-MN are ideal green chemistry replacements for the currently-used manufacturing process for 2-methoxy-6-acetylnaphthalene synthesis in the production of *(S)*-naproxen. The design of new solid acids for selective chemical transformations is an area of active research. The carbon acid **Acid1** has shown promise as a regioselective homogeneous catalyst; the incorporation of **Acid1** into a solid support is an area of current and future research.

## 4.3 Acylation of 2-methoxynaphthalene

The carbon acid, **Acid1**, was tested for its ability to regioselectively catalyze the Friedel-Crafts acylation of 2-methoxynaphthalene (2-MN). This reaction is of interest because the regioisomer 2-methoxy-6-acetylnapththalene (2,6-AMN) is a precursor in the synthesis of the anti-inflammatory analgesic *(S)*-naproxen. Figure 4.3 gives chemical structures for 2-MN, *(S)*-naproxen, and the three major acylated regioisomers of 2-MN: 1-acetyl-2-methoxynaphthalene (1,2-AMN), 2-methoxy-6-acetylnaphthalene (2,6-AMN), and 1-acetyl-7-methoxynaphthalene (1,7-AMN).

The current method for Friedel-Crafts acylation of 2-MN for the manufacture of pharmaceuticals and fine chemicals involves the use of Lewis acid reagents, namely $AlCl_3$ in nitrobenzene or $BF_3$ in HF with acid chlorides as the acylating reagents.[207] The Lewis acids are often referred to as "catalysts". However, they are required in greater than stoichiometric amounts, and, strictly speaking, should not be termed catalysts. Drawbacks to such Friedel-Crafts syntheses include poor regioselectivity and corrosive reaction mixtures. Moreover, there is considerable waste generated, as the Lewis acids must be present in excess of two molar equivalents. The use of $AlCl_3$, for instance, generates greater than four chloride ions per molecule of acylated 2-MN.[208] This is because the aryl ketone product forms a 1:1 adduct with $AlCl_3$, requiring a hydrolysis step in the workup. In addition, the methoxy group, which acts as an activator toward electrophilic aromatic substitution and a directing group (for *ortho/para* substitution in benzene rings), is a good donor site for the Lewis acid, thus reducing the activity of both reagent and "catalyst".[196] Because of these drawbacks, and in light of the large amount of waste generated in the manufacture, the regioselective synthesis of 2,6-AMN has been the focus of green chemistry methodological efforts, with a considerable thrust toward the development of solid acid catalysts with "greener" acylating reagents such as acids and acid anhydrides for regioselective Friedel-Crafts acylation.

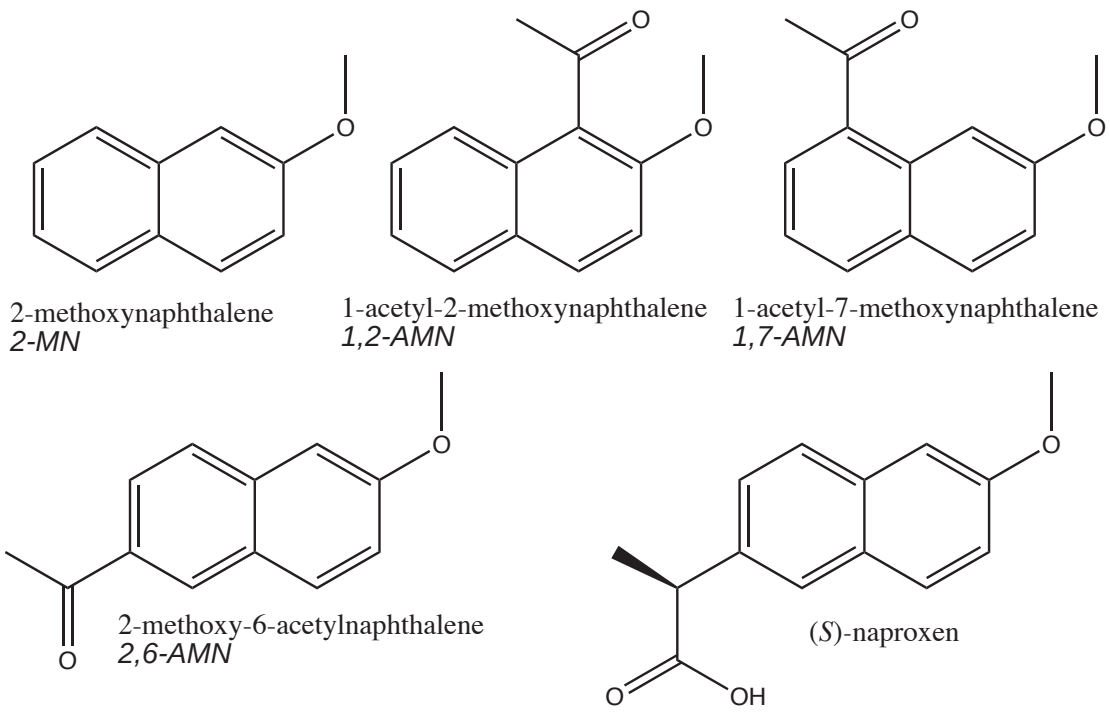


Figure 4.3 Chemical structures of 2-methoxynaphthalene, the three major acylated products of 2-MN, and *(S)*-naproxen.

As mentioned above in Section 4.2, solid acids are prized in green chemistry for their ease of separation and the potential to be regenerated and reused.

Nearly all of the previous and current work on solid acid catalysts for Friedel-Crafts acylation has focused on the use of zeolites as Lewis and Brønsted acid catalysts. A number of different zeolites have been investigated. For reactions with HBEA zeolite, it was found that 1-acetyl-2-methoxynaphthalene (1,2-AMN) forms initially and then disappears, with a final product composition of primarily 2,6-AMN (87%) with a small amount of 1-acetyl-7-methoxylnaphthalene (1,7-AMN) (13%).[196,208] The reaction conditions for which the HBEA15 catalyst gave the best yield are nitrobenzene solvent, heating at 170 °C for 4 h, 5 equivalents 2-MN and 1 equivalent acetic anhydride ($Ac_2O$), with a total yield (with respect to concentration of the acylating reagent) of 76.3%. At lower temperatures (120 °C, 50 h), the reaction gave a higher overall yield, 90%, with a different distribution of products: 68% 2,6-AMN, 8% 1,7-AMN, and 23% 1,2-AMN. It should be noted when considering the yields that these conditions require a large excess of starting material. Studies by the same authors on modifications of various commercially-available zeolites found that dealumination of HBEA zeolites reduced the number of Lewis acidic sites while increasing the Brønsted acidity. This led to increased yields of 2,6-AMN relative to the non-treated zeolites.[209] Experiments with the zeolite HBEA773 (400 K, 24 h, 2:1 2-MN:$Ac_2O$ in nitrobenzene) gave 40% conversion with 71% selectivity toward 2,6-AMN, 25% toward 1,2-AMN, and 4.5% toward 1,7-AMN. It was also found that thermal pretreatment of the zeolite HBEA773 could increase the selectivity of the catalyst toward 2,6-AMN.[210]

In addition to zeolites, mesoporous materials were investigated for catalytic activity in the Friedel-Crafts acylation of 2-MN. The mesoporous molecular sieve MCM-41 is an aluminosilicate material with uniformly sized pores. Both Brønsted acidic (H-MCM-41) and Lewis acidic (Zn-MCM-41) modifications of the molecular sieves have been studied.[211] The reactions were run with a 2:1 excess of 2-MN to acylating reagent; thus, the yields are reported with respect to concentration of acylating reagent. It was

found that H-MCM-41 exhibited high regioselectivity in the acylation of 2-MN with acetic anhydride to form 1,2-AMN (97% regioselectivity, 40% conversion) at 100 °C. In contrast, the Lewis-acidic Zn-MCM-41 gave regioselective acylation of 2-MN with acetyl chloride to form 2,6-AMN with 81% selectivity and 28.9% conversion . In both cases, the catalyst could be successfully regenerated with treatment at 450 °C for 2 days. However, regenerated Zn-MCM-41 catalyst led to increasing yields of 1,2-AMN.[211]

The selectivity of HBEA zeolites toward acylation of 2-MN has been investigated in a number of studies. Heinichen and Hölderich concluded, through modifications of HBEA pores and subsequent studies of the catalytic activity of the modified zeolites, that the bulkier regioisomer 1,2-AMN is formed by reactions occurring on the surface of the zeolite catalyst, while acylation to form the more linear regioisomer 2,6-AMN arises from reactions that take place within the interior of the zeolites. Thus, it is the size/shape preference of the porous material that gives rise to the catalytic regioselectivity.[212] Further study of the acylation mechanism by Fromentin, Coustard, and Guisnet found that HBEA zeolite catalyzes the isomerization of 1,2-AMN to 2,6- and 1,7-AMN by a number of mechanisms: through deacylation of 1,2-AMN and transacylation of 1,2- to 2,6-AMN in the presence of excess 2-MN. While a small amount of intramolecular isomerization takes place, it rarely occurs for the 1,2- to 2,6-AMN isomerization, although it is intramolecular rearrangement of 1,2-AMN that gives rise to the 1,7-AMN regioisomer.[213] The zeolite is hypothesized to participate in the transacylation, isomerization, and deacylation reactions by transferring a proton and forming an adduct with the resulting cationic *sigma*-complex. See Section 4.7 below for further explanation of the proposed mechanism of Friedel-Crafts acylation reactions. A computational study of the catalytic selectivity of large-pore zeolites supported the role of size selectivity of zeolitic pores on the regioselectivity of the acylation of 2-MN. Molecular modeling of the diffusion of 2-MN, 1,2-AMN, and 2,6-AMN in four different zeolite pores showed that 2-MN and 2,6-AMN diffuse most rapidly through the pores, while 1,2-AMN diffusion was hindered due to its bulky shape. It was also found that Brønsted acidity

modeled by hybrid quantum mechanics/molecular mechanics methods (QM/MM) affected overall catalytic activity, but not regioselectivity. Hence, the authors suggest that pores giving rise to the largest difference in diffusion rates between 1,2-AMN and 2,6-AMN would lead to the highest regioselectivity.[214]

Research in the Barybin group on the Friedel-Crafts acylation of 2-MN with **Acid1** has initially focused primarily on homogeneous catalysis. However, as mentioned previously in Section 4.2, **Acid1** can be modified for inclusion in a number of solid supports for heterogeneous catalysis. As detailed in the following section, **Acid1** shows excellent regioselectivity that is solvent-dependent, so that reaction conditions can be chosen to selectively afford either 2,6-AMN or 1,2-AMN.

## 4.4 Regioselective Friedel-Crafts Acylation with Acid1: Experimental Results

Experiments carried out in the Barybin group with **Acid1** showed solvent-dependent regioselective acylation of 2-MN. For reactions in $CH_3NO_2$ at 100 °C, a mixture of 2-MN with 9% **Acid1** catalyst resulted in a 60% total yield of acylated methoxynaphthalene. The total products consisted of a mixture of 90% 2,6-AMN and 10% 1,7-AMN. For similar reaction conditions in $CH_3NO_2$ with only 1% acid, the only product obtained is 1,2-AMN. This suggests that extra amounts of catalyst are required to deacylate the kinetic product 1,2-AMN in order to form the more thermodynamically-stable 1,7- and 2,6-AMN products. This is discussed in detail in Section 4.7 below. Acylation of 2-MN was also carried out in hexanes solvent. With 1% catalyst loading at 100 °C, 100% yield of 1,2-AMN was obtained. No formation of other AMN regiomers was documented upon increasing the catalyst loading to ca. 10 mol %. The possible origins of this solvent-dependent regioselectivity are discussed further in Section 4.7.

Computational methods were used to explore possible catalytic mechanisms, and to rationalize the regioselectivity of **Acid1**. The methods for the calculations are detailed below in Section 4.5. Thermodynamic factors in the homogeneous catalytic process

are discussed in Section 4.6, while kinetic factors are addressed in Section 4.7. Chemical modifications to **Acid1** for incorporation into a solid support for heterogeneous catalysis are considered in Section 4.8. Finally, conclusions are offered in Section 4.9.

## 4.5 *Ab Initio* and Density Functional Theory Calculations: Methods

Geometries for all regioisomers of acylated 2-methoxynaphthalene were obtained with Density Functional Theory (DFT) calculations at the B3LYP/6-31+G* level using the Gaussian 98 and Gaussian 03 computational programs.[215,216] A number of starting geometries were used for the optimizations in order to increase the likelihood of finding the global minimum, rather than optimizing a structure that is at a local energy minimum. Frequency calculations were carried out on the optimized structures of lowest energy; in all cases, positive frequencies indicated that a minimized structure was found. For the experimentally-observed regioisomers (1,2-, 2,6-, and 1,7-AMN), higher level second-order perturbation theory (MP2) energies with the 6-31+G* basis set were calculated using the DFT optimized structures as starting input. Solvation energies were calculated using the Polarized Continuum Model.[217] Enthalpy and entropy values for the free energy differences of the three observed regioisomers were calculated from the vibrational frequencies. Atomic charges were calculated using the Natural Bond Orbital (NBO) program.[218] Optimized geometries and vibrational frequencies for the **Acid1** and the corresponding conjugate base were obtained with B3LYP/6-31+G* calculations. For the styryl modification of **Acid1**, **styryl-Acid1**, reported in Ref. 24, the reported crystal structure[219] was used as a starting input for the geometry optimization.

## 4.6 Thermodynamic Control

In order to explore the origins of the regioselectivity of Friedel-Crafts acylation of 2-MN with **Acid1**, the relative energies of all possible monoacylated products were calculated. Optimized geometries and vibrational frequencies for the regioisomers were

obtained at the B3LYP/6-31+G* level, as detailed in Section 4.5. The relative energies with PCM calculations in $CH_3NO_2$ solvent are reported in Table 4.1.[220] The numbering scheme for the carbon atoms of 2-methoxynaphthalene, used below in Tables 4.1 and 4.3, is given in Figure 4.4.

Table 4.1 Relative Electronic Energies (B3LYP/6-31+G*) for Optimized Geometries of the Regioisomers of Acylated 2-methoxynaphthalene.

| Acylated Carbon | Relative Energy (kcal/mol) |
|---|---|
| **1** | 9.16 |
| **3** | 4.83 |
| **4** | 5.68 |
| **5** | 4.89 |
| **6** | 0.00 |
| **7** | 0.73 |
| **8** | 4.13 |

As seen in Table 4.1, the lowest-energy regioisomer is 2,6-AMN (from acylation at the **6** carbon), which is the desired acylated product of 2-MN for the manufacture of naproxen. One regioisomer, 2-methoxy-7-acetylnaphthalene (from acylation at the **7** carbon), lies close in energy ($<$ 1 kcal/mol) to the thermodynamic product, 2,6-AMN. However, as discussed below in Section 4.7, this regioisomer is not kinetically accessible, because of the position of the methoxy directing group. Many of the regioisomers have calculated relative energies 4-6 kcal/mol higher than that of 2,6-AMN. The highest energy form, 1,2-AMN (from acylation at the **1** carbon), is calculated to be considerably higher in energy than 2,6-AMN, at 9.2 kcal/mol.

In order to compare with experimental yields, free energies were calculated for the three observed regioisomers: 1,2-AMN, 1,7-AMN, and 2,6-AMN. The free energies were calculated from MP2 (Second-order Møller-Plesset Perturbation Theory) energies

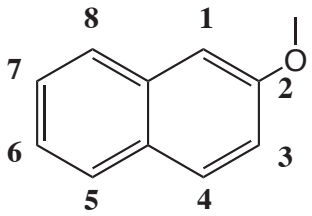


Figure 4.4 2-methoxynaphthalene: carbon numbers

with the 6-31+G* basis set, using the PCM solvent model with nitromethane solvent. These more expensive calculations were used because they generally give better relative energy differences. An enthalpic correction to the electronic energies was calculated from the vibrational partition function, $q_{vib}$, where

$$q_{vib} = \prod_{j=1}^{3n-5} \frac{e^{-\frac{h\nu_j}{2k_bT}}}{1 - e^{-\frac{h\nu_j}{k_bT}}}. \qquad [4.1]$$

Using the harmonic oscillator approximation, the vibrational enthalpy is defined as:[221]

$$H_{vib} = Nk_bT^2 \frac{\partial \ln q_{vib}}{\partial T} = Nk_b \sum_{j=1}^{3n-5} \left( \frac{h\nu_j}{2k_b} + \frac{h\nu_j e^{-\frac{h\nu_j}{k_bT}}}{1 - e^{-\frac{h\nu_j}{k_bT}}} \right). \qquad [4.2]$$

In Eqs. 4.1-4.3, $k_b$ is the Boltzmann constant, $N$ is the total number of particles, and $n$ is the number of atoms in the molecule. Likewise, the vibrational frequencies were used to calculate the entropy term for each of the regioisomers, using Equation 4.3:

$$S_{vib} = \frac{H_{vib}}{T} + Nk_b \ln q_{vib}. \qquad [4.3]$$

Note that rotational contributions to the enthalpy and entropy were neglected, as rotations are hindered in solution. Moreover, differences in the translational contributions were assumed to be negligible as well.

The free energies in $CH_3NO_2$ at 373 K of the three experimentally-observed regioisomers, 1,2-AMN, 1,7-AMN, and 2,6-AMN, are reported in Table 4.2, along with the predicted composition at equilibrium and the experimentally-observed yields (also in nitromethane at 373 K). As can be seen when comparing the free energies given in

Table 4.2 Relative Free Energies at 373 K of Experimentally-observed Regioisomers of Acylated 2-MN (MP2/6-31+G*) in $CH_3NO_2$.

| | Calculated $\Delta$G (kcal/mol) | Predicted Yield | Experimental Yield |
|---|---|---|---|
| 2,6-AMN | 0.0 | 97.6% | 90% |
| 1,7-AMN | 2.8 | 2.3% | 10% |
| 1,2-AMN | 4.9 | 0.1% | 0% |

Table 4.2 with the electronic energy values reported in Table 4.1, the relative energy differences are smaller for the calculated free energies. The regioisomer 2,6-AMN is the thermodynamic product, more stable than 1,7-AMN by 2.8 kcal/mol, and more stable than the isomer 1,2-AMN by 4.9 kcal/mol. From the free energy differences, yields were calculated assuming the reaction goes to equilibrium. The predicted yields (97.6% 2,6-AMN, 2.3% 1,7-AMN, 0.1% 1,2-AMN) are in good agreement with the experimental yields of 90% 2,6-AMN and 10% 1,7-AMN (with no amount of 1,2-AMN detected). The good agreement between the predicted and experimental yields indicates that the calculated free energy differences reasonably describe the experimental situation, and that the experimental reaction conditions (100 °C in $CH_3NO_2$) allow the reaction to reach equilibrium or near-equilibrium. The fact that equilibrium is reached (or approached) indicates that the catalyst enables reversibility of the reaction, since the kinetic product is 1,2-AMN, as discussed in detail below in the next section (Section 4.7).

## 4.7 Kinetic Factors

Friedel-Crafts acylation,[222] which involves formation of a carbon-carbon bond by addition of an acyl group to an aromatic ring to form an aryl ketone or aldehyde, is proposed to go through the following general mechanism:[223] 1. Generation of a reactive acyl group by addition of a Lewis or strong protic acid to an acylating agent (typically,

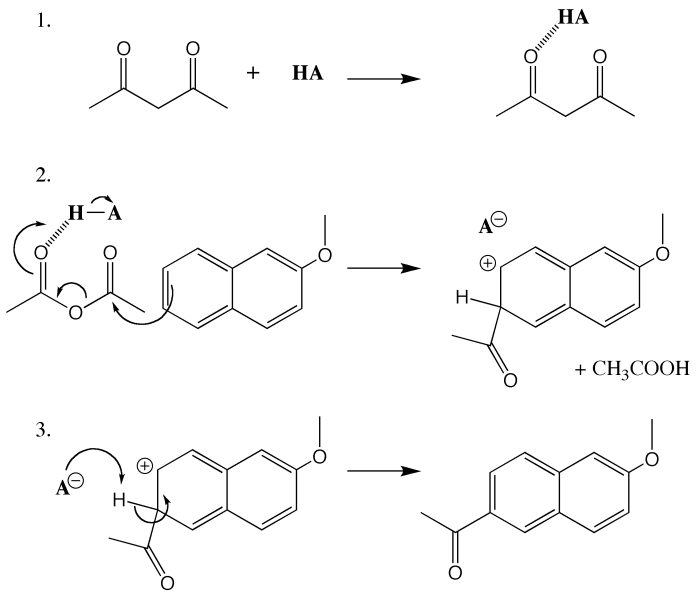


Figure 4.5 Proposed mechanism for Friedel-Crafts acylation 2-methoxynaphthalene with acetic anhydride and a generic Brønsted acid. Step 1: generation of a reactive acyl group; Step 2: formation of the *sigma* intermediate; Step 3: deprotonation

an acyl halide, acid anhydride, ester, or carboxylic acid). The reactive acyl group may be a cationic acylium ion (R-C=$O^+$), or a complex formed between the carbonyl group and the Lewis/Brønsted acid. 2. Addition of the acyl group to the aromatic ring to form a cationic *sigma* intermediate. 3. Deprotonation of the *sigma* intermediate to form the final acylated product. This mechanism is illustrated in Figure 4.5 for the acylation of 2-methoxynaphthalene with acetic anhydride with a generic acid, **HA**.

The methoxy group of 2-MN is an *ortho/para* directing group for the electrophilic aromatic substitution (EAS) of phenyl rings; it acts in a similar fashion as a directing group in EAS reactions of naphthalene. This is a factor of kinetic control in determining the regioselectivity of the acylation reaction. For example, it can be seen in Table 4.1 that some of the products at deactivated carbons are more stable than some of the isomers of acylated 2-MN that are acylated at activated carbons. Population analysis through the NBO charges shows that the **4**, **5**, **7** and **8** carbons are less activated for electrophilic aromatic substitution . Charges of the carbon atoms and the associated

hydrogens in 2-methoxynaphthalene are summarized in Table 4.3. The carbon atoms at

Table 4.3 Calculated NBO Charges for 2-methoxynaphthalene (B3LYP/6-31+G* optimized geometry).

| Carbon Number | Charge on Carbon | Charge on Hydrogen | C-H Total Charge |
|---|---|---|---|
| **1** | -0.31 | 0.24 | -0.07 |
| **2** | 0.32 | N/A | |
| **3** | -0.26 | 0.25 | -0.01 |
| **4** | -0.20 | 0.24 | 0.04 |
| **5** | -0.20 | 0.23 | 0.03 |
| **6** | -0.25 | 0.24 | -0.01 |
| **7** | -0.23 | 0.24 | 0.01 |
| **8** | -0.22 | 0.23 | 0.01 |

the **1**, **3**, and **6** positions are more highly charged, thus providing a kinetic aspect to the regioselectivity. Note that acylation at the **3** carbon is not observed, while acylation at carbon **8** is, so that the NBO charges are not entirely predictive of which regioisomers are observed.

If all regioisomers were kinetically accessible, one would predict a detectable amount of substitution at the inactivated carbons at equilibrium, since several of these isomers are close in energy (see Table 4.1) to 1,7-AMN: 1-acetyl-3-methoxynaphthalene and 1-acetyl-6-methoxynaphthalene from acylation of carbons **4** and **5**, respectively. Even more notable is that the isomer 2-methoxy-7-acetylnaphthalene, from acylation at the **7** carbon, lies very close in energy (0.73 kcal/mol higher) to the thermodynamic and observed major product in $CH_3NO_2$ solvent, 2,6-AMN. Thus, the NBO charges verify the resonance structures of 2-MN, both of which explain the kinetic selectivity provided by the methoxy directing group.

Another factor to explore in the kinetic selectivity of the acylation of 2-MN is the relative stabilities of the *sigma* intermediates. Optimized geometries of the *sigma* intermediates were obtained at the B3LYP/6-31+G* levels, and frequency calculations were used to verify that the structures constitute local minima. Solvation effects were calculated from single point energies using the PCM model. For comparison with the experimental results, nitromethane and heptane solvents were used; experiments in the Barybin group were carried out in nitromethane and hexanes, as described above in Section 4.4. Since there is no model in the Gaussian computational package for PCM calculations in hexanes, heptane ($\epsilon$=1.9) was selected instead, as the molecular sizes and dielectric constants of the two solvents are similar. The relative energies of the *sigma* intermediates are given in Table 4.4 for the three observed regioisomers of acetylmethoxynaphthalene: 1,2-AMN, 1,7-AMN, and 2,6-AMN.

Table 4.4 Relative Energies of *Sigma* Complex Intermediates (B3LYP/6-31+G* single point PCM calculations).

| *Sigma* Intermediate | Relative Energy in Heptane (kcal/mol) | Relative Energy in Nitromethane (kcal/mol) |
|---|---|---|
| 1,2-AMN | 0.0 | 0.0 |
| 1,7-AMN | 6.21 | 5.09 |
| 2,6-AMN | 7.34 | 6.06 |

The *sigma* intermediate of the 1,2-AMN isomer has the lowest energy in both solvents, while that of the thermodynamic product 2,6-AMN has the highest energy. Experiments in hexanes at 100 °C yielded the 1,2-AMN isomer exclusively, while acylation of 2-MN in more polar nitromethane solvent yielded primarily 2,6-AMN (90% selectivity), with small amounts of 1,7-AMN (10% selectivity). The relative stabilities of the *sigma* complexes, as given in Table 4.4 may help rationalize this observation. In heptane, the energy differences between the intermediates for 1,2-AMN and 2,6-AMN (1,7-AMN) are larger than those in nitromethane. Specifically, in nitromethane

the energy difference between the $\sigma$ intermediates for 1,2-AMN and 2,6-AMN (1,7-AMN) is 6.06 kcal/mol (5.09 kcal/mol), while in heptane the energy difference is 7.34 kcal/mol (6.06 kcal/mol). The differences in relative stabilities of the intermediates in the two solvents is equal to $\sim 2k_bT$ at 100 °C, enough that the *sigma* intermediates of the more stable products may not be kinetically accessible in hexanes. Alternatively, the observed solvent-dependent regioselectivity may be attributed to the *reversibility* of the reactions, *i.e.*, deacylation via the 1,2-AMN *sigma* intermediate may be kinetically accessible in $CH_3NO_2$, whereas it may not be in hexanes. In fact, it is likely that the ability of the catalyst to deacylate 1,2-AMN, the kinetic product in both polar and non-polar solvent, is key to the regioselective formation of 2,6-AMN, the thermodynamic product, in $CH_3NO_2$ with **Acid1**.

## 4.8 Chemical Modifications of Acid1: Effects on Acidity

The gas phase acidities of **Acid1** and **styryl-Acid1** were calculated using the difference between the B3LYP/6-31+G* calculated energies (as described in Section 4.5) of the acids and the corresponding conjugate bases. The gas phase acidity for **Acid1** is 295 kcal/mol, while that of **styryl-Acid1** is 307 kcal/mol. In order to benchmark the quantum chemistry calculations, the gas phase acidities of a number of acids, including a set of carbon acids, were calculated and compared to the experimentally-determined values. In general, the calculated gas phase acidities were in reasonable agreement with the experimental values. Although the calculations are not always in quantitative agreement with experiment, the calculated values generally agreed with the experimental gas phase acidities within 5 kcal/mol. The results are given in Table 4.5. As can be seen, the gas phase acidity of **Acid1** is higher than those of a number of strong acids. The solution-phase acidity is more challenging to calculate by *ab initio* methods, as solvent effects on proton transfer are hard to calculate without explicit treatment of the solvent. The PCM calculations that were used with the 2-MN derivatives were carried

out on the acids and conjugate bases, but calculations of absolute $pK_a$ values for intermolecular proton transfer reactions with continuum solvation models are generally unreliable.[225] The gas phase acidity of **styryl-Acid1** is still quite strong, though not as favorable as that of **Acid1**, which acts as a homogeneous catalyst. Furthermore, one would expect solvation effects to favor proton transfer from the smaller, homogeneous catalyst **Acid1**, thus making **Acid1** a stronger acid than its solid analogue based on **styryl-Acid1**. However, while incorporation into a solid support may reduce the acidity, it may actually increase the catalytic activity for some reactions. In work with sulfonic superacids, Harmer and co-workers found that highly polar liquid superacids were essentially inactive in the isomerization and oligomerization of 1-dodecene. After incorporation into sol-gel and silica supports, miscibility issues were overcome, and the solid acids showed high catalytic activity for the reaction.[226]

## 4.9 Conclusions

Quantum chemistry calculations were used to find the optimized geometries and relative energies of **Acid1**, its styryl modification, regioisomers of acylated 2-methoxynaphthalene, and their related *sigma* intermediates. The primary conclusions are: 1. The desired acylated product for the synthesis of (*S*)-naproxen, 2,6-AMN is the thermodynamic product in the acylation of 2-methoxynaphthalene. 2. The regioisomer 1,2-AMN is the kinetic product; it has the lowest energy $\sigma$ intermediates. 3. The gas phase acidity of **Acid1** is stronger than that of many strong acids. 4. The efficacy of **Acid1** in the regioselective acylation of 2-MN can likely be attributed to its ability to catalyze both the forward and reverse (deacylation) reactions, thereby affording the thermodynamic product.

The carbon acid, **Acid1**, shows promise as a greener acid in Friedel-Crafts acylation, both as a homogeneous catalyst and as a solid acid. Future directions involve studies to determine the best porous materials in which to incorporate **Acid1** for solid acid catalysis.

Table 4.5 Experimental and Calculated Gas Phase Acidities.

| Acid | Experimental[224] $\Delta H^0_{acid}$ (kcal/mol) | Calculated (B3LYP/6-31+G*) $\Delta E^0_{acid}$ (kcal/mol) |
|---|---|---|
| $CH_3OH$ | 378.02 $\pm$ 2.5, 381.4 $\pm$ 1.7 | 385 |
| HF | 371.3 $\pm$ 2.9 | 366 |
| pyrrole | 359.2, 360.7 $\pm$ 2 | 365 |
| acetic acid | 348.5 $\pm$ 2 | 349 |
| $C_6H_5SH$ | 338.9 $\pm$ 3.4 | 340 |
| HCl | 333.3 $\pm$ 0.3 | 328 |
| $HNO_3$ | 324.6 $\pm$ 1 | 323 |
| HBr | 323.6 $\pm$ 0.3 | 321 |
| Carbon Acids | | |
| $HCF_3$ | 377.6 $\pm$ 2.5 | 381 |
| $CH_3CN$ | 371.3 $\pm$ 2.9 | 380 |
| $C_6H_5SO_2CH_3$ | 363.1 $\pm$ 2 | 373 |
| $CH_3COF$ | 359 $\pm$ 6 | 365 |
| *p*-$NO_2C_6H_4CH_3$ | 353.1 $\pm$ 2 | 356 |
| HCN | 349.3 $\pm$ 2.4 | 353 |
| **styryl-Acid1** | | 307 |
| **Acid1** | | 295 |

# Chapter 5

# Conclusions

## 5.1 Overview and Future Directions

In this dissertation, charge transfer reactions that take place in porous media were studied. In Chapter 2, the driving forces behind solute diffusion upon photoexcitation were studied in 10 and 15 Å spherical nanocavities. In prior research carried out by the Thompson group, it was found that a long-time tail in the time-dependent fluorescence signal correlated to solvent diffusion away from the nanocavity wall toward the interior of the pore. The free and internal energies and entropies were calculated for the model dye molecule in a variety of solvents: methyl iodide, acetonitrile, and methanol. It was found that the entropy is at a maximum at radial distances where the solvent density is highest. The entropy maxima also correspond to minima in the free energy; thus, it is entropy that drives the solute to be located within a solvent layer. In contrast, the internal energy is maximized at locations where the solute center-of-mass is located between the solvent layers (with one atom each in a solvent layer). The rotational free energies/probability distributions as a function of solute radial distance suggest that the rotational entropy is minimized at these positions between solvent layers, but maximized when located near the cavity wall, and within a solvent layer. In the latter cases, more solute orientations are possible, and rotation through the azimuthal angle is maximized when the solute is oriented perpendicular to the wall. Although entropy directs the solute to positions within the solvent layers, it is the internal energy (electrostatic interactions) that ultimately decides the position of the ground/excited state dye molecule: the less polar ground-state solute has lower internal energy in locations near

the cavity wall, within the first solvent layer, while the more polar excited-state solute has lower internal energy within the second solvent layer or closer to the cavity interior where the solvent is effectively more polar.

In the spherical, hydrophobic nanocavities, less polar solutes are located near the cavity wall, while more polar solutes are located near the interior. This has implications in the design of nanoporous catalysts. If a less polar substrate is reacting at the surface to form a more polar reactant, a material with these properties is ideal. However, for the opposite case (polar substrate, less polar reactants), a different environment would be required to maximize reactivity and diffusion of products away from catalytic active sites. In Chapter 3, a reaction that is critical in many catalytic processes, proton transfer, was studied in $CH_3Cl$ solvent in a 12 Å radius spherical, hydrophobic cavity. The model proton transfer complex is based on a phenol-amine intermolecular reaction. The infrared spectra of this proton transfer complex were calculated for a number of different cases in which the proton transfer equilibria were varied. It was found that the infrared absorption spectra contain information about chemical equilibria; furthermore, the frequency-frequency time correlation functions, which can be obtained with non-linear vibrational spectroscopy, contain information about the rate of proton transfer. Specifically, by fitting the function $\phi$, which is Fourier transformed to the absorption spectrum, with an analytical expression that describes two Lorentzian peaks, the ratio of the products to reactants can be found. The proton transfer model used here does lend itself to such a fitting, since the transition dipole moments for products and reactants are nearly identical. Another consequence of having similar values of $\underline{\mu}_{d_{10}}(t)$ is that the dipole-dipole time correlation functions are identical to the rotational autocorrelation function. The widths of the product and reactant peaks in the absorption spectra are related to the solute dipole autocorrelation/reorientation times (wider peaks indicate faster reorientation). The spectral peaks also display motional narrowing due to rapid frequency fluctuations. Because of the slow chemical exchange, it was found that the orientational TCF of the products with chemical exchange could be predicted as a linear

function of the *products only* and *reactants only* reorientation times, with the ratios coming from the respective mole fraction of each species.

Future directions for this work involve using a proton transfer model in which the nitrogen-oxygen distance can vary. This could be achieved by adding a Morse or harmonic potential to the heavy atoms. One would expect that the varying N-O distance would result in different transition dipole moments for products and reactants; it would then be interesting to revisit the analytical expressions for the infrared spectra and the dipole-dipole autocorrelation functions to see what information about chemical equilibria and relative reorientation times can be found in the infrared spectrum for a more realistic (or, at least, more general) system. It would also be instructive to revisit the Condon and other linear response approximations with the revised proton transfer model.

Another interesting result of the work in Chapter 3 is the implications it has for finding proton transfer rate constants from IR photon echo experiments. This work suggests that the long-time decay rate, $\tau$, of the frequency-frequency time correlation function is equal to $(k_f + k_b)^{-1}$. If $K_{eq}$ is known, the proton transfer rate contstants can be found, since $K_{eq} = \frac{k_f}{k_b}$. Thus, ground-state proton transfer rate constants may be found with nonlinear vibrational spectroscopy. Previously, vibrational spectroscopy has been used to find *excited-state* proton transfer rates. Excited-state proton transfer dynamics provide useful data regarding the effects of confinement on chemical reactivity, but do not provide information on the dynamics of *ground-state* proton transfer, which is more relevant for understanding and designing nanoporous catalysts.

In Chapter 4, a carbon acid catalyst (**Acid1**) and its role in the Friedel-Crafts acylation of 2-methoxynaphthalene (2-MN) were studied. This reaction is of interest because 2,6-acetylmethoxynaphthalene (2,6-AMN), one of the acylation products of 2-MN, is a precursor in the manufacture of the analgesic *(S)*-naproxen. The conventional acylation reaction protocol is carried out using Lewis acids such as $AlCl_3$, and the desired regioisomer is a minor product at best. Thus, an improvement in the regioselectivity

of this process would be environmentally beneficial, with less need for separation and purification, and less generation of hazardous waste. When $AlCl_3$ is used as a Lewis acid, it is not done catalytically, but in excess of stoichiometric amounts. Moreover, if the carbon acid is immobilized in a porous host, it can be used as a solid acid, which can, in principle, be removed from the reaction mixture, regenerated, and reused.

By calculating the relative energies of the acylated products of 2-MN, it was found that the desired product, 2,6-AMN, is the thermodynamic product. The major product in most catalyzed acylations of 2-MN, 1,2-AMN, was shown to be the kinetic product, as the *sigma* intermediate of this product is lower in energy than the *sigma* complexes of the other acylation products. Thus, the carbon acid achieves regioselectivity by forming the thermodynamic product, most likely by catalyzing the deacylation of 1,2-AMN to 2-MN so that 2,6-AMN may eventually be formed as the predominant product. The gas phase acidity of **Acid1** and modifications to the acid that allow for incorporation thereof into porous materials were calculated. It was found that the gas phase acidity is higher than those of many strong acids, and that *para*-modification reduces the acidity only slightly. Of course, the gas phase acidity does not take into account solvation effects, which play a significant role in acid-base chemistry. Future work in this area may involve calculating the acidities in solution or developing a model of the acid and simulating it in a confined system.

Most of the research described herein involves a very simple confining framework: a spherical, smooth-walled nanocavity. Future directions involve using a more realistic confining framework, such as one with atomic detail/roughness. Work has been done in the Thompson group with a library of sol-gel pores,[227] and carrying out studies in these pores is a natural direction in extending this work. However, the simplifications offered by the spherical nanocavities do offer some advantages. Without atomic roughness, it is easy to define properties as a function of radial distance from the wall. Also, the volume is easily defined, so that concentration can be calculated in a straightforward manner.

This work contributes to the body of knowledge regarding confinement effects in materials. Clearly, there are innumerable discoveries still to be made in the area. With the vast variety of materials that can be synthesized, the interplay between theoretical and experimental chemistry in the rational design of functional materials looks to be a promising area of research for many years to come.

## LIST OF REFERENCES


[1] Brinker, C. J.; Scherer, G. W. *Sol-Gel Science: The Physics and Chemistry of Sol-Gel Processing*. Academic Press, New York, 1990.

[2] Pileni, M. P. *Structure and Reactivity in Reverse Micelles*. Elsevier, New York, 1989.

[3] Steed, J. W.; Atwood, J. L. *Supramolecular Chemistry*. Wiley, New York, 2000.

[4] MacGillivray, L. R.; Atwood, J. L. *Adv. Supramolec. Chem.*, **2000**, *6*, 157–183.

[5] J. Rebek, J. *Acc. Chem. Res.*, **1999**, *32*, 278–286.

[6] Palmer, L. C.; J. Rebek, J. *Org. Biomol. Chem.*, **2004**, *2*, 3051–3059.

[7] Vos, D. E. D.; Dams, M.; Sels, B. F.; Jacobs, P. A. *Chem. Rev.*, **2002**, *102*, 3615–3640.

[8] Welbes, L. L.; Borovik, A. S. *Acc. Chem. Res.*, **2005**, *38*, 765–774.

[9] Fierro-Gonzalez, J. C.; Kuba, S.; Hao, Y.; Gates, B. C. *J. Phys. Chem. B*, **2006**, *110*, 13326–13351.

[10] Pastore, H. O.; Coluccia, S.; Marchese, L. *Annu. Rev. Mater. Res.*, **2005**, *35*, 351–395.

[11] Davis, M. E. *Nature*, **2002**, *417*, 813–821.

[12] Bradshaw, D.; Claridge, J. B.; Cussen, E. J.; Prior, T. J.; Rosseinsky, M. *Acc. Chem. Res.*, **2005**, *38*, 273–282.

[13] Hench, L. L. *Sol-Gel Silica: Properties, Processing, and Technology Transfer*. Noyes Publications, Westwood, NJ, 1998.

[14] Hench, L. L.; West, J. K. *Chem. Rev.*, **1990**, *90*, 33–72.

[15] Corma, A. *Chem. Rev.*, **1997**, *97*, 2373–2419.

[16] Williams, A. K.; Hupp, J. T. *J. Am. Chem. Soc.*, **1998**, *120*, 4366–4371.

[17] Scott, B. J.; Wirnsberger, G.; Stucky, G. D. *Chem. Mater.*, **2001**, *13*, 3140–3150.

[18] T. F. Degnan, J. *Top. Catal.*, **2000**, *13*, 349–356.

[19] Eddaoudi, M.; Kim, J.; Rosi, N.; Vodak, D.; Wachter, J.; O'Keeffe, M.; Yaghi, O. M. *Science*, **2002**, *295*, 469–472.

[20] Rowsell, J.; Yaghi, O. M. *Angew. Chem. Int. Ed.*, **2005**, *44*, 4670–4681.

[21] Chen, B.; Contreras, D. S.; Ockwig, N.; Yaghi, O. M. *Angew. Chem. Int. Ed.*, **2005**, *44*, 4745–4748.

[22] Millward, A.; Yaghi, O. M. *J. Am. Chem. Soc.*, **2006**, *127*(17998–17999).

[23] Kuznicki, S. M.; Bell, V. A.; Nair, S.; Hillhouse, H. W.; Jacubinas, R. M.; Braunbarth, C. M.; Toby, B. H.; Tsapatsis, M. *Nature*, **2001**, *412*, 720–724.

[24] Ishihara, K.; Hasegawa, A.; Yamamoto, H. *Angew. Chem. Int. Ed.*, **2001**, *40*, 4077–4079.

[25] Fendler, J. H. *Acc. Chem. Res.*, **1976**, *9*, 153–161.

[26] Bunton, C. A.; Nome, F.; Quina, F. H.; Romsted, L. S. *Acc. Chem. Res.*, **1991**, *24*, 357–364.

[27] Garcia-Rio, L.; Herves, P.; Mejuto, J. C.; Perez-Juste, J.; Rodriguez-Dafonte, P. *Ind. Eng. Chem. Res.*, **2003**, *42*, 5450–5456.

[28] Correa, N. M.; Zorzan, D. H.; Chiarini, M.; Cerichelli, G. *J. Org. Chem.*, **2004**, *69*, 8224–8230.

[29] Correa, N. M.; Zorzan, D. H.; D'Anteo, L.; Lasta, E.; Chiarini, M.; Cerichelli, G. *J. Org. Chem.*, **2004**, *69*(8231–8238).

[30] Correa, N. M.; Durantini, E. D.; Silber, J. J. *J. Org. Chem.*, **2000**, *65*, 6427–6433.

[31] Lee, Y. J.; Zhang, T.; Barbara, P. F. *J. Phys. Chem. B*, **2004**, *108*, 5175–5178.

[32] Bakale, G.; Beck, G.; Thomas, J. K. *J. Phys. Chem.*, **1992**, *96*, 2328–2334.

[33] Bakale, G.; Beck, G.; Thomas, J. K. *J. Phys. Chem.*, **1981**, *85*, 1062–1064.

[34] Kwon, O.-H.; Jang, D.-J. *J. Phys. Chem. B*, **2005**, *109*, 20479–20484.

[35] Kwon, O.-H.; Jang, D.-J. *J. Phys. Chem. B*, **2005**, *109*, 8049–8052.

[36] Spry, D. B.; Goun, A.; Glusac, K.; Moilanen, D. E.; Fayer, M. D. *J. Am. Chem. Soc.*, **2007**, *129*, 8122–8130.

[37] Cohen, B.; Huppert, D.; Solntsev, K. M.; Tsfadia, Y.; Nachliel, E.; Gutman, M. *J. Am. Chem. Soc.*, **2002**, *124*, 7539–7547.

[38] Bardez, E.; Goguillon, B.-T.; Keh, E.; Valeur, B. *J. Phys. Chem.*, **1984**, *88*, 1909–1913.

[39] Bardez, E.; Monnier, E.; Valeur, B. *J. Phys. Chem.*, **1985**, *89*, 5031–5036.

[40] Das, S.; Datta, A.; Bhattacharyya, K. *J. Phys. Chem. A*, **1997**, *101*, 3299–3304.

[41] Mandal, D.; Pal, S. K.; Bhattacharyya, K. *J. Phys. Chem. A*, **1998**, *102*, 9710–9714.

[42] Pal, S. K.; Mandal, D.; Bhattacharyya, K. *J. Phys. Chem. B*, **1998**, *102*, 11017–11023.

[43] Politi, M. J.; Chaimovich, H. *J. Phys. Chem.*, **1986**, *90*, 282–287.

[44] Kwon, O.-H.; Jang, D.-J. *J. Phys. Chem. B*, **2005**, *109*, 8049–8052.

[45] Tamura, K.; Schelly, Z. A. *J. Am. Chem. Soc.*, **1979**, *101*, 7643–7644.

[46] Harada, S.; Schelly, Z. A. *J. Phys. Chem.*, **1982**, *86*, 2098–2102.

[47] Marcus, R. A. *Annu. Rev. Phys. Chem.*, **1964**, *15*, 155–196.

[48] Marcus, R. A. *Proc. Electrochem. Soc.*, **1980**, *80*, 1–14.

[49] Newton, M. D.; Sutin, N. *Annu. Rev. Phys. Chem.*, **1984**, *35*, 437–480.

[50] Warshel, A. *Computer Modelling of Chemical Reactions in Proteins and Solution*. Wiley, New York, 1991.

[51] Åqvist, J.; Warshel, A. *Chem. Rev.*, **1993**, *93*, 2523–2544.

[52] Juanós i Timoneda, J.; Hynes, J. T. *J. Phys. Chem.*, **1991**, *95*, 10431–10442.

[53] Geissler, P. L.; Dellago, C.; Changler, D.; Hutter, J.; Parrinello, M. *Science*, **2001**, *291*, 2121–2124.

[54] Linse, P. *J. Chem. Phys.*, **1989**, *90*, 4992–5004.

[55] Linse, P.; Halle, B. *Mol. Phys.*, **1989**, *67*, 537–573.

[56] Faeder, J.; Ladanyi, B. M. *J. Phys. Chem. B*, **2000**, *104*, 1033–1046.

[57] Thompson, W. H. *J. Chem. Phys.*, **2002**, *117*, 6618–6628.

[58] Thompson, W. H. *J. Chem. Phys.*, **2004**, *120*, 8125–8133.

[59] Gomez, J. A.; Thompson, W. H. *J. Phys. Chem. B*, **2004**, *108*, 20144–20154.

[60] Gomez, J. A.; Tucker, A. K.; Shepherd, T. D.; Thompson, W. H. *J. Phys. Chem. B*, **2005**, *109*, 17479–17487.

[61] Li, S. M.; Shepherd, T. D.; Thompson, W. H. *J. Phys. Chem. A*, **2004**, *108*, 7347–7355.

[62] Li, S.; Thompson, W. H. *J. Phys. Chem. B*, **2005**, *109*, 4941–4946.

[63] Thompson, W. H. *J. Phys. Chem. B*, **2005**, *109*, 18201–18208.

[64] Feng, X. B.; Thompson, W. H. *J. Phys. Chem. C*, **2007**, *111*, 18060–18072.

[65] Mitchell-Koch, K. R.; Thompson, W. H. *J. Phys. Chem. C*, **2007**, *111*, 11991–12001.

[66] Mitchell-Koch, K. R.; Thompson, W. H. *J. Phys. Chem. B*, **2008**.

[67] Dunn, B.; Zink, J. I. *Chem. Mat.*, **1997**, *9*, 2280–2291.

[68] Ghosh, S.; Mondal, S. K.; Sahu, K.; Bhattacharyya, K. *J. Phys. Chem. A*, **2006**, *110*, 13139–13144.

[69] Eyal, M.; Reisfeld, R.; Chernyak, V.; Kaczmarek, L.; Grabowska, A. *Chem. Phys. Lett.*, **1991**, *176*, 531–535.

[70] McKiernan, J.; Simoni, E.; Dunn, B.; Zink, J. I. *J. Phys. Chem.*, **1994**, *98*, 1006–1009.

[71] Prosposito, P.; Marks, D.; Zhang, H.; Glasbeek, M. *J. Phys. Chem. A*, **1998**, *102*, 8894–8902.

[72] Prosposito, P.; Marks, D.; Zhang, H.; Glasbeek, M. *Radiat. Eff. Defects Solids*, **1999**, *150*, 385–389.

[73] Carturan, S.; Quaranta, A.; Maggioni, G.; Vomiero, A.; Ceccato, R.; Mea, G. D. *J. Sol-Gel Sci. Technol.*, **2003**, *26*, 931–935.

[74] Quaranta, A.; Carturan, S.; Maggioni, G.; Ceccato, R.; Mea, G. D. *J. Non-Cryst. Solids*, **2003**, *322*, 1–6.

[75] Umeto, H.; Abe, K.; Kawasaki, C.; Igarashi, T.; Sakurai, T. *J. Photochem. Photobiol. A: Chem.*, **2003**, *156*, 127–137.

[76] Bhattacharyya, K. *Acc. Chem. Res.*, **2003**, *36*, 95–101.

[77] Laria, D.; Kapral, R. *J. Chem. Phys.*, **2002**, *117*, 7712–7718.

[78] Nogami, M.; Nagao, R.; Cong, W.; Abe, Y. *J. Sol-Gel Sci. Technol.*, **1998**, *13*, 933–936.

[79] Nogami, M. *J. Sol-Gel Sci. Technol.*, **2004**, *31*, 359–364.

[80] Daiko, Y.; Kasuga, T.; Nogami, M. *Micropor. Mesopor. Mater.*, **2004**, *69*, 149–155.

[81] Streck, C.; Mel'nichenko, Y. B.; Richert, R. *Phys. Rev. B*, **1996**, *53*, 5341–5347.

[82] Richert, R. *Phys. Rev. B*, **1996**, *54*, 15762–15766.

[83] Riter, R. E.; Willard, D. M.; Levinger, N. E. *J. Phys. Chem. B*, **1998**, *102*, 2705–2714.

[84] Riter, R. E.; Undiks, E. P.; Kimmel, J. R.; Levinger, N. E. *J. Phys. Chem. B*, **1998**, *102*, 7931–7938.

[85] Willard, D. M.; Riter, R. E.; Levinger, N. E. *J. Am. Chem. Soc.*, **1998**, *120*, 4151–4160.

[86] Riter, R. E.; Undiks, E. P.; Levinger, N. E. *J. Am. Chem. Soc.*, **1998**, *120*, 6062–6067.

[87] Pant, D.; Riter, R. E.; Levinger, N. E. *J. Chem. Phys.*, **1998**, *109*, 9995–10003.

[88] Willard, D. M.; Levinger, N. E. *J. Phys. Chem. B*, **2000**, *104*, 11075–11080.

[89] Pant, D.; Levinger, N. E. *Langmuir*, **2000**, *16*, 10123–10130.

[90] Corbeil, E. M.; Riter, R. E.; Levinger, N. E. *J. Phys. Chem. B*, **2004**, *108*, 10777–10784.

[91] Correa, N. M.; Levinger, N. E. *J. Phys. Chem. B*, **2006**, *110*, 13050–13061.

[92] Pal, S. K.; Sukul, D.; Mandal, D.; Sen, S.; Bhattacharyya, K. *J. Phys. Chem. B*, **2000**, *104*, 2613–2616.

[93] Sarkar, N.; Das, K.; Datta, A.; Das, S.; Bhattacharyya, K. *J. Phys. Chem.*, **1996**, *100*, 10523–10527.

[94] Bhattacharyya, K. *J. Fluoresc.*, **2001**, *11*, 167–176.

[95] Sen, S.; Sukul, D.; Dutta, P.; Bhattacharyya, K. *J. Phys. Chem. A*, **2001**, *105*, 10635–10639.

[96] Sahu, K.; Roy, D.; Mondal, S. K.; Halder, A.; Bhattacharyya, K. *J. Phys. Chem. B*, **2004**, *108*, 11971–11975.

[97] Sen, P.; Mukherjee, S.; Halder, A.; Bhattacharyya, K. *Chem. Phys. Lett.*, **2004**, *385*, 357–361.

[98] Satoh, T.; Okuno, H.; Tominaga, K.; Bhattacharyya, K. *Chem. Lett.*, **2004**, *33*, 1090–1091.

[99] Bhattacharyya, K.; Bagchi, B. *J. Phys. Chem. A*, **2000**, *104*, 10603–10613.

[100] Nandi, N.; Bagchi, B. *J. Phys. Chem.*, **1996**, *100*, 13914–13919.

[101] Baumann, R.; Ferrante, C.; Deeg, F. W.; Bräuchle, C. *J. Chem. Phys.*, **2001**, *114*, 5781–5791.

[102] Baumann, R.; Ferrante, C.; Kneuper, E.; Deeg, F. W.; Bräuchle, C. *J. Phys. Chem. A*, **2003**, *107*, 2422–2430.

[103] Zhang, J.; Bright, F. V. *J. Phys. Chem.*, **1991**, *95*, 7900–7907.

[104] Hazra, P.; Sarkar, N. *Chem. Phys. Lett.*, **2001**, *342*, 303–311.

[105] Senapati, S.; Chandra, A. *J. Chem. Phys.*, **1999**, *111*, 1223–1230.

[106] Faeder, J.; Ladanyi, B. M. *J. Phys. Chem. B*, **2001**, *105*, 11148–11158.

[107] Faeder, J.; Ladanyi, B. M. *J. Phys. Chem. B*, **2005**, *109*, 6732–6740.

[108] Š. Vajda; Jimenez, R.; Rosenthal, S. J.; Fidler, V.; Fleming, G. R.; E. W. Castner, J. *J. Chem. Soc. Faraday Trans.*, **1995**, *91*, 867–873.

[109] Carter, E. A.; Hynes, J. T. *J. Phys. Chem.*, **1989**, *93*, 2184–2187.

[110] Carter, E. A.; Hynes, J. T. *J. Chem. Phys.*, **1991**, *94*, 5961–5979.

[111] Freitas, F. F. M.; Fernandes, F. M. S. S.; Cabral, B. J. C. *J. Phys. Chem.*, **1995**, *99*, 5180–5186.

[112] Jorgensen, W. L.; Briggs, J. M. *Mol. Phys.*, **1988**, *63*, 547–558.

[113] Haughney, M.; Ferrario, M.; McDonald, I. R. *J. Phys. Chem.*, **1987**, *91*, 4934–4940.

[114] Jorgensen, W. L. *J. Phys. Chem.*, **1986**, *90*, 1276–1284.

[115] Lide, D. R., Ed. *CRC Handbook of Chemistry and Physics, 87th edition*. Taylor and Francis, Boca Raton, FL, 2007.

[116] Allen, M. P.; Tildesley, D. J. *Computer Simulation of Liquids*. Oxford University Press, New York, 1987.

[117] Frenkel, D.; Smit, B. *Understanding Molecular Simulation*. Academic Press, San Diego, CA, 2002.

[118] Shoemaker, D. P.; Garland, C. W.; Nibler, J. W. *Experiments in Physical Chemistry*. McGraw-Hill, New York, 5th edition, 1989.

[119] Metropolis, N.; Rosenbluth, A. W.; Rosenbluth, M. N.; Teller, A. H.; Teller, E. *J. Chem. Phys.*, **1953**, *21*, 1087–1092.

[120] Mittal, J.; Errington, J. R.; Truskett, T. M. *Phys. Rev. Lett.*, **2006**, *96*, 177804.

[121] Mammen, M.; Shakhnovich, E. I.; Deutsch, J. M.; Whitesides, G. M. *J. Org. Chem.*, **1998**, *63*, 3821–3830.

[122] Histograms with zero counts (zero probability) were assigned free energy values of 2.5 kcal/mol in order to plot the data.

[123] Ashbaugh, H. S.; Paulaitis, M. E. *J. Phys. Chem.*, **1996**, *100*, 1900–1913.

[124] Rodriguez, J.; Marti, J.; Guardia, E.; Laria, D. *J. Phys. Chem. B*, **2007**, *111*, 4432–4439.

[125] Laage, D.; Hynes, J. T. *Chem. Phys. Lett.*, **2006**, *433*, 80–85.

[126] Rey, R.; Møller, K. B.; Hynes, J. T. *Chem. Rev.*, **2004**, *104*, 1915–1928.

[127] Roscioli, J. R.; Diken, E. G.; Johnson, M. A.; Horvath, S.; McCoy, A. B. *J. Phys. Chem. A*, **2006**, *110*, 4943–4952.

[128] Gaigeot, M.-P.; Sprik, M. *J. Phys. Chem. B*, **2003**, *107*, 10344–10358.

[129] Singh, N. J.; Park, M.; Min, S. K.; Suh, S. B.; Kim, K. S. *Angew. Chem. Int. Ed.*, **2006**, *45*, 3795–3800.

[130] Nakabayashi, T.; Nishi, N. *J. Phys. Chem. A*, **2002**, *106*, 3491–3500.

[131] Bour, P. *Chem. Phys. Lett.*, **2002**, *365*, 82–88.

[132] Mathias, G.; Marx, D. *Proc. Natl. Acad. Sci. USA*, **2007**, *104*, 6980–6985.

[133] Ha, J.; Kim, Y. S.; Hochstrasser, R. M. *J. Chem. Phys.*, **2006**, *124*, 064508.

[134] Møller, K. B.; Rey, R.; Hynes, J. T. *J. Phys. Chem. A*, **2004**, *108*, 1275–1289.

[135] Nigro, B.; Re, S.; Laage, D.; Rey, R.; Hynes, J. T. *J. Phys. Chem. A*, **2006**, *110*, 11237–11243.

[136] Tan, H.-S.; Piletic, I. R.; Fayer, M. D. *J. Chem. Phys.*, **2005**, *122*, 174501.

[137] Stenger, J.; Madsen, D.; Hamm, P.; Nibbering, E. T. J.; Elsaesser, T. *Phys. Rev. Lett.*, **2001**, *87*, 027401.

[138] Schmitz, M.; Tavan, P. *J. Chem. Phys.*, **2004**, *121*, 12247.

[139] Woutersen, S.; Bakker, H. J. *Phys. Rev. Lett.*, **2006**, *96*, 138305.

[140] Amir, W.; Gallot, G.; Hache, F.; Bratos, S.; Leicknam, J.; Vuilleumier, R. *J. Chem. Phys.*, **2007**, *126*, 034511.

[141] Kaledin, M.; Kaledin, A.; Bowman, J. M. *J. Phys. Chem. A*, **2006**, *110*, 2933–2939.

[142] Zhu, Z.; Tuckerman, M. E. *J. Phys. Chem. B*, **2002**, *106*, 8009–8018.

[143] Piletic, I. R.; Moilanen, D. E.; Levinger, N. E.; Fayer, M. D. *J. Am. Chem. Soc.*, **2006**, *128*, 10366–10367.

[144] Florián, J.; Kubelková, L. *J. Phys. Chem.*, **1994**, *98*, 8734–8741.

[145] Coudert, F.-X.; Vuillemier, R.; Boutin, A. *ChemPhysChem*, **2006**, *7*, 2464–2467.

[146] Dokter, A. M.; Woutersen, S.; Bakker, H. J. *Phys. Rev. Lett.*, **2005**, *94*, 178301.

[147] Piletic, I. R.; Moilanen, D. E.; Spry, D. B.; Levinger, N. E.; Fayer, M. D. *J. Phys. Chem. A*, **2006**, *110*, 4985–4999.

[148] Zhong, Q.; Steinhurst, D. A.; Carpenter, E. E.; Owrutsky, J. C. *Langmuir*, **2002**, *18*, 7401–7408.

[149] Sando, G. M.; Dahl, K.; Owrutsky, J. C. *Chem. Phys. Lett.*, **2006**, *418*, 402–407.

[150] Sando, G. M.; Fox, D. M.; Sutto, T. E.; Owrutsky, J. C. *J. Chem. Phys.*, **2005**, *123*, 084504.

[151] Sando, G. M.; Dahl, K.; Zhong, Q.; Owrutsky, J. C. *J. Phys. Chem. A*, **2005**, *109*, 5788–5792.

[152] Sando, G. M.; Dahl, K.; Owrutsky, J. C. *J. Phys. Chem. B*, **2005**, *109*, 4084–4095.

[153] Sando, G. M.; Dahl, K.; Owrutsky, J. C. *J. Phys. Chem. A*, **2004**, *108*, 11209–11217.

[154] Sando, G. M.; Zhong, Q.; Owrutsky, J. C. *J. Chem. Phys.*, **2004**, *121*, 2158–2168.

[155] Zhong, Q.; Baronavski, A. P.; Owrutsky, J. C. *J. Chem. Phys.*, **2003**, *119*, 9171–9177.

[156] Zhong, Q.; Baronavski, A. P.; Owrutsky, J. C. *J. Chem. Phys.*, **2003**, *118*, 7074–7080.

[157] Zundel, G. *Adv. Chem. Phys.*, **2000**, *111*, 1–217.

[158] Iftimie, R.; Tuckerman, M. E. *Angew. Chem. Int. Ed.*, **2006**, *45*, 1144–1147.

[159] Iftimie, R.; Tuckerman, M. E. *J. Chem. Phys.*, **2005**, *122*, 214508.

[160] Brancato, G.; Tuckerman, M. E. *J. Chem. Phys.*, **2005**, *122*, 224507.

[161] Kim, J.; Schmitt, U. W.; Gruetzmacher, J. A.; Voth, G. A.; Scherer, N. E. *J. Chem. Phys.*, **2002**, *116*, 737–746.

[162] Iyengar, S. S.; Petersen, M. K.; Day, T. J. F.; Burnham, C. J.; Telge, V. E.; Voth, G. A. *J. Chem. Phys.*, **2005**, *123*, 084309.

[163] Diken, E. G.; Headrick, J. M.; Roscioli, J. R.; Bopp, J. C.; Johnson, M. A.; McCoy, A. B. *J. Phys. Chem. A*, **2005**, *109*, 1487–1490.

[164] Marx, D. *ChemPhysChem*, **2006**, *7*, 1848–1870.

[165] Jezierska, A.; Panek, J.; Borstnik, U.; Mavri, J.; Janezic, D. *J. Phys. Chem. B*, **2007**, *111*, 5243–5248.

[166] Borgis, D.; Tarjus, G.; Azzouz, H. *J. Phys. Chem.*, **1992**, *96*, 3188–3191.

[167] Borgis, D.; Tarjus, G.; Azzouz, H. *J. Chem. Phys.*, **1992**, *97*, 390–400.

[168] Lanczos, C. *J. Res. Natl. Bur. Stand. (U.S.)*, **1950**, *45*, 255–282.

[169] Saad, Y. *Numerical Methods for Large Eigenvalue Problems*. Halstead Press, New York, 1992.

[170] Colbert, D. T.; Miller, W. H. *J. Chem. Phys.*, **1992**, *96*, 1982–1991.

[171] Bond, S. D.; Leimkuhler, B. J.; Laird, B. B. *J. Comput. Phys.*, **1999**, *151*, 6129–6141.

[172] Zhang, J. Z.; Heller, E. J.; Huber, D.; Imre, D. G. *J. Phys. Chem.*, **1991**, *95*, 6129–6141.

[173] Coalson, R. D.; Kinsey, J. L. *J. Chem. Phys.*, **1986**, *85*, 4322–4340.

[174] Bergsma, J. P.; Berens, P. H.; Wilson, K. R.; Fredkin, D. R.; Heller, E. J. *J. Phys. Chem.*, **1984**, *88*, 612–619.

[175] Landau, L. D. *Zs. Sovjet.*, **1932**, *1*, 88.

[176] Landau, L. D.; Lifshitz, E. M. *Quantum Mechanics, 3rd ed.* Pergamon Press, Oxford, 1977.

[177] Zener, C. *Proc. R. Soc. London, Ser. A*, **1932**, *137*, 696–702.

[178] Zener, C. *Phys. Rev.*, **1931**, pp 556–569.

[179] Kubo, R.; Toda, M.; Hashitsume, N. *Statistical Physics II: Nonequilibrium Statistical Mechanics*. Springer-Verlag, New York, 1991.

[180] Saven, J. G.; Skinner, J. L. *J. Chem. Phys.*, **1993**, *99*, 4391–4402.

[181] Lawrence, C. P.; Skinner, J. L. *J. Chem. Phys.*, **2002**, *117*, 8847–8854.

[182] Hayashi, T.; Jansen, T. I. C.; Zhuang, W.; Mukamel, S. *J. Phys. Chem. A*, **2005**, *109*, 64–82.

[183] Librovich, N. B.; Sakun, V. P.; Sokolov, N. D. *Chem. Phys.*, **1979**, *39*, 351–366.

[184] Schmidt, J. R.; Corcelli, S. A.; Skinner, J. L. *J. Chem. Phys.*, **2005**, *123*, 044513.

[185] Corcelli, S. A.; Skinner, J. L. *J. Phys. Chem. A*, **2005**, *109*, 6154–6165.

[186] Thompson, W. H.; Hynes, J. T. *J. Phys. Chem. A*, **2001**, *105*, 2582–2590.

[187] Chandler, D. *Introduction to Modern Statistical Mechanics*. Oxford University Press, New York, 1987.

[188] Steinel, T.; Asbury, J. B.; Corcelli, S. A.; Lawrence, C. P.; Skinner, J. L.; Fayer, M. D. *Chem. Phys. Lett.*, **2004**, *386*, 295–300.

[189] Asbury, J. B.; Steinel, T.; Stromberg, C.; Corcelli, S. A.; Lawrence, C. P.; Skinner, J. L.; Fayer, M. D. *J. Phys. Chem. A*, **2004**, *108*, 1107–1119.

[190] Asbury, J. B.; Steinel, T.; Kwak, K.; Corcelli, S. A.; Lawrence, C. P.; Skinner, J. L.; Fayer, M. D. *J. Chem. Phys.*, **2004**, *121*, 12431.

[191] Fecko, C. J.; Eaves, J. D.; Loparo, J. J.; Tokmakoff, A.; Geissler, P. L. *Science*, **2003**, *301*, 1698–1702.

[192] Loparo, J. J.; Fecko, C. J.; Eaves, J. D.; Roberts, S. T.; Tokmakoff, A. *Phys. Rev. B*, **2004**, *70*, 180201.

[193] Fecko, C. J.; Loparo, J. J.; Roberts, S. T.; Tokmakoff, A. *J. Chem. Phys.*, **2005**, *122*, 054506.

[194] Hamm, P. *J. Chem. Phys.*, **2006**, *124*, 124506.

[195] Anastas, P. T.; Bartless, L. B.; Kirchhoff, M. M.; Williamson, T. C. *Catal. Today*, **2000**, *55*, 11–22.

[196] Sartori, G.; Maggi, R. *Chem. Rev.*, **2006**, *106*, 1077–1104.

[197] Macquarrie, D. J. *Phil. Trans. R. Soc. Lond. A*, **2000**, *358*, 419–430.

[198] Corma, A. *Chem. Rev.*, **1995**, *95*, 559–614.

[199] Sen, S. E.; Smith, S. M.; Sullivan, K. A. *Tetrahedron*, **1999**, *55*, 12657–12698.

[200] Clark, J. H. *Acc. Chem. Res.*, **2002**, *35*, 791–797.

[201] Tanev, P. T.; Pinnavaia, T. J. *Science*, **1995**, *267*, 865–867.

[202] Bossaert, W. D.; Vos, D. E. D.; Rhijn, W. M. V.; Bullen, J.; Grobet, P. J.; Jacobs, P. A. *J. Catal.*, **1999**, *182*, 156–164.

[203] Clark, J. H.; Price, P. M.; Martin, K.; Macquarrie, D. J.; Bastock, T. W. *J. Chem. Res.*, **1997**, pp 430–431.

[204] Olah, G. A.; Prakash, G. K. S.; Sommer, J. *Superacids*. John Wiley and Sons, Inc., New York, 1985.

[205] Heidekum, A.; Harmer, M. A.; Hoelderich, W. F. *J. Catal.*, **1999**, *188*, 230–232.

[206] Kozhevnikov, I. V. *Chem. Rev.*, **1998**, *98*, 171–198.

[207] Zoeller, J. R.; C. E. Sumner, J. *J. Org. Chem.*, **1990**, *55*, 319–324.

[208] Fromentin, E.; Coustard, J.-M.; Guisnet, M. *J. Mol. Catal. A: Chem.*, **2000**, *159*, 377–388.

[209] Berreghis, A.; Ayrault, P.; Fromentin, E.; Guisnet, M. *Catal. Lett.*, **2000**, *68*, 121–127.

[210] Casagrande, M.; Storaro, L.; Lenarda, M.; Ganzerla, R. *Appl. Catal., A*, **2000**, *201*, 263–270.

[211] Gunnewegh, E. A.; Gopie, S. S.; van Bekkum, H. *J. Mol. Catal. A: Chem.*, **1996**, *106*, 151–158.

[212] Heinichen, H. K.; Hölderich, W. F. *J. Catal.*, **1999**, *185*, 408–414.

[213] Fromentin, E.; Coustard, J.-M.; Guisnet, M. *J. Catal.*, **2000**, *190*, 433–438.

[214] Patil, S. P.; Yadav, G. D. *Comp. Biol. Chem.*, **2003**, *27*, 393–404.

[215] Frisch, M.; Trucks, G.; Schlegel, H.; Scuseria, G.; Robb, M.; Cheeseman, J.; Zakrzewski, V.; J.A. Montgomery, J.; Stratmann, R.; Burant, J.; Dapprich, S.; Millam, J.; Daniels, A.; Kudin, K. N.; Strain, M.; Farkas, O.; Tomasi, J.; Barone, V.; Cossi, M.; Cammi, R.; Mennucci, B.; Pomelli, C.; Adamo, C.; Clifford, S.; Ochterski, J.; Petersson, G.; Ayala, P.; Cui, Q.; Morokuma, K.; Salvador, P.; Dannenberg, J.; Malick, D.; Rabuck, A.; Raghavachari, K.; Foresman, J.; Cioslowski, J.; Ortiz, J.; Baboul, A.; Stefanov, B.; Liu, G.; Liashenko, A.; Piskorz, P.; Komaromi, I.; Gomperts, R.; Martin, R.; Fox, D.; Keith, T.; Al-Laham, M.; Peng, C.; Nanayakkara, A.; Challacombe, M.; Gill, P.; Johnson, B.; Chen, W.; Wong, M.; Andres, J.; Gonzalez, C.; Head-Gordon, M.; Replogle, E.; Pople, J. *Gaussian 98 (Revision A.11)*. Gaussian, Inc., Pittsburgh, PA, 2001.

[216] Frischand, M.; Trucksand, G.; Schlegel, H.; Scuseria, G.; Robb, M.; Cheeseman, J.; J.A. Montgomery, J.; Vreven, T.; Kudin, K.; Burant, J.; Millam, J.; Iyengar, S.; Tomasi, J.; Barone, V.; Mennucci, B.; Cossi, M.; Scalmani, G.; Rega, N.; Petersson, G.; Nakatsuji, H.; Hada, M.; Ehara, M.; Toyota, K.; Fukuda, R.; Hasegawa, J.; Ishida, M.; Nakajima, T.; Honda, Y.; Kitao, O.; Nakai, H.; Klene, M.; Li, X.; Knox, J.; Hratchian, H.; Cross, J.; Bakken, V.; Adamo, C.; Jaramillo, J.; Gomperts, R.; Stratmann, R.; Yazyev, O.; Austin, A.; Cammi, R.; Pomelli, C.; Ochterski, J.; Ayala, P.; Morokuma, K.; Voth, G. A.; Salvador, P.; Dannenberg, J.; Zakrzewski, V.; Dapprich, S.; Daniels, A. D.; Strain, M.; Farkas, O.; Malick, D.; Rabuck, A.; Raghavachari, K.; Foresman, J.; Ortiz, J.; Cui, Q.; Baboul, A.; Clifford, S.; Cioslowski, J.; Stefanov, B. B.; Liu, G.; Liashenko, A.; Piskorz, P.; Komaromi, I.; Martin, R.; Fox, D.; Keith, T.; Al-Laham, M.; Peng, C.; Nanayakkara, A.; Challacombe, M.; Gill, P.; Johnson, B.; Chen, W.; Wong, M. W.; Gonzalez, C.; Pople, J. A. *Gaussian 03, Revision D.01*. Gaussian, Inc., Wallingford, CT, 2004.

[217] Miertus, S.; Scrocco, E.; Tomasi, J. *Chem. Phys.*, **1981**, *55*, 117–129.

[218] Glendening, E. D.; Reed, A. E.; Carpenter, J. E.; Weinhold, F. NBO Version 3.1.

[219] The Cambridge Structural Database code for the crystal structures is ACORAL.

[220] Thermal corrections to the enthalpy (at 298 K) from the vibrational frequency calculations were also considered. However, the thermal corrections are very similar for all of the regioisomers, changing the relative energies by no more than 0.1 kcal/mol, except in the case of 1,7-AMN (acylation at carbon **8**), which lies 0.3 kcal/mol higher in relative energy when the thermal enthalpy correction is considered. Even so, the thermal corrections are negligible in this data set.

[221] McQuarrie, D. A. *Statistical Thermodynamics*. Harper and Row Publishers, New York, New York, 1973.

[222] Olah, G. A. *Friedel-Crafts Chemistry*. John Wiley and Sons, Inc., New York, 1973.

[223] Carey, F. A.; Sundberg, R. J. *Advanced Organic Chemistry, Part A: Structure and Mechanisms*. Kluwer Academic/Plenum Publishers, New York, fourth edition, 2000.

[224] Bowers, M. T., Ed. *Gas Phase Ion Chemistry*, volume 2. Academic Press, New York, New York, 1979.

[225] "Continuum Solvation Models", C. J. Cramer and D. G. Truhlar, Chapter 1 in Solvent Effects and Chemical Reactivity, O. Tapia and J. Bertrán, ed. Kluwer Academic Publishers, Dordrecht, The Netherlands, 1996.

[226] Harmer, M. A.; Junk, C.; Rostovtsev, V.; Carcani, L. G.; Vickery, J.; Schnepp, Z. *Green Chem.*, **2007**, *9*, 30–37.

[227] Gulmen, T. S.; Thompson, W. H. *Langmuir*, **2006**, *22*, 10919–10923.